TECHNISCHE UNIVERSITÄT MÜNCHEN

Lehrstuhl für Anorganische Chemie mit Schwerpunkt Neue Materialien

Synthesis, Characterization and Physical Properties of Semiconducting Clathrate Compounds

Andreas Kaltzoglou

Vollständiger Abdruck der von der Fakultät für Chemie der Technischen Universität München zur Erlangung des akademischen Grades eines

Doktors der Naturwissenschaften

genehmigten Dissertation.

Vorsitzender:	Univ.-Prof. Dr. Kai-Olaf Hinrichsen
Prüfer der Dissertation:	1. Univ.-Prof. Dr. Thomas F. Fässler
	2. Univ.-Prof. Dr. Wolfgang Scherer, Universität Augsburg

Die Dissertation wurde am 07.04.2009 bei der Technischen Universität München eingereicht und durch die Fakultät für Chemie am 20.05.2009 angenommen.

To my mother

Acknowledgements

- To Prof. Thomas Fässler for accepting me as Ph.D. student in his group and supporting me throughout this course.
- To Ms. Manuela Donaubauer for her kind assistance in various organization issues.
- To Dr. Stephan Hoffmann for supervising most of my experimental work.
- To Dr. Sung-Jin Kim and Dr. Annette Spiekermann for their continuous encouragement and support.
- To Dr. Florian Kraus for introducing me to the technique of alkali-metal distillation.
- To Dr. Martin Schreyer for introducing me to X-ray diffraction techniques.
- To Dr. Simeon Ponou for the cooperation in the field of clathrate research.
- To Ms. Ingrid Werner for her assistance in scanning electron microscopy.
- To Prof. Rainer Niewa for the helpful discussions and advices on solid-state chemistry and thermal analysis.
- To Prof. Bo Iversen and Dr. Simon Johnsen at the Aarhus University in Denmark for the thermoelectric measurements.
- To Dr. Eiji Nishibori and Dr. Mogens Christensen at the SPring-8 facilities in Japan for the synchrotron measurements and refinements.
- To Prof. Wolfgang Scherer, Dr. Ernst-Wilhelm Scheidt and M. Sc. Christian Gold at the Augsburg University in Germany for the electrical resistivity and heat capacity measurements.
- To Prof. Hiroyasu Shimizu and Ass. Prof. Tetsuji Kume at the Gifu University in Japan for the Raman spectroscopy.
- To Prof. Andrei Shevelkov, Igor Presniakov and Alexey Sobolev at the Moscow State University in Russia for the Mössbauer spectroscopy.
- To Dr. Tobias Unruh at the neutron source Heinz Maier-Leibnitz (FRM II) for the inelastic neutron-scattering experiments.
- To the European European Union's RTN program of Nanocage Materials (EU-project Nr. HPRN-CT 2002-00193) for the financial support.

- Finally, to my parents, my cousins Rania and Sakis, my friend Elina as well as my colleagues at the TUM for supporting me patiently all these years. For without them this work would just not be possible.

Abbreviations

A	=	Alkali metal
ADP	=	Atomic Displacement Parameter
bcc	=	body-centered cubic
CCD	=	Charge-Coupled Device
dmf	=	dimethylformamide
DOS	=	electron Density Of States
DTA	=	Differential Thermal Analysis
EDX	=	Energy Dispersive X-ray analysis
FOM	=	Figure Of Merit
hkad	=	hexakaidecahedron
IPDS	=	Image Plate Detector System
pdod	=	pentagonal dodecahedron
PDOS	=	Phonon Density Of States
PGEC	=	Phonon-Glass and Electron-Crystal
pkad	=	pentakaidecahedron
SEM	=	Scanning Electron Microscope
SOF	=	Site Occupation Factor
SPS	=	Spark Plasma Sintering
SQUID	=	Superconducting QUantum Interference Device
tkad	=	tetrakaidecahedron
Tr	=	Triel, element of the group 13
Tt	=	Tetrel, element of the group 14
VEC	=	Valence Electron Concentration
XRD	=	X-Ray Diffraction
XRPD	=	X-Ray Powder Diffraction

Contents

1. Introduction

1.1 Thermoelectric materials

The global need for efficient energy management has become in the last decades a major scientific topic. Among various research fields, the interest in thermoelectric materials has revived. In general, thermoelectricity is the direct conversion of temperature differential into voltage and vice versa.[1,2] The effect has been discovered by T. Seebeck in 1821 by applying a temperature gradient (ΔT) on a metal rod that produced electromotive force (ΔV) on the junctions. Inversely, passing electric current through the rod causes temperature gradient on the junctions (Figure 1.1). The two phenomena are known as Seebeck and Peltier effect, respectively and are best described by the band theory for solids.[3]

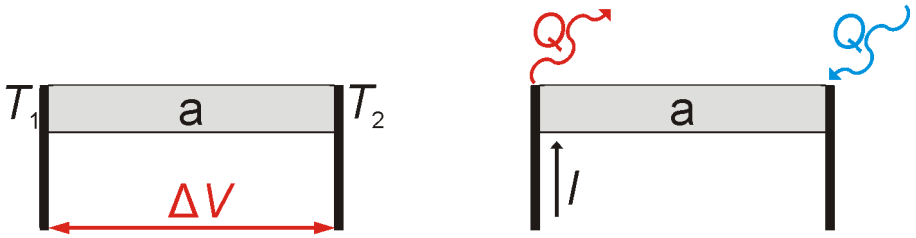

Figure 1.1 Schematic representation of the thermoelectric effects on a metal rod (a).

The development of powerful thermoelectric materials is an interdisciplinary field involving physics, chemistry and mechanical engineering. Up to now, thermoelectric materials have gained widespread use as thermocouples as well as some commercial interest in refrigeration devices and small-size coolers for computer processors (Peltier effect). However, there have been only limited applications in energy recovery from waste heat (Seebeck effect). This has intensified the search for new materials and technologies that would provide except for a large Seebeck coefficient, $S = \Delta V\,(\Delta T)^{-1}$, maximization of the electrical conductivity (σ) and minimization of the thermal conductivity (κ).[4,5] The overall thermoelectric efficiency is defined by the dimensionless figure of merit (ZT):

$$ZT = \frac{\sigma S^2 T}{\kappa}$$

However, these three transport properties are strongly correlated and cannot be optimized separately. Materials such as pure metals with high electrical conductivity also exhibit high electron contribution to the thermal conductivity whereas insulators with large Seebeck coefficient (in absolute value) and low thermal conductivity are also very

poor electric conductors and therefore would not reach large *ZT* values. The main characteristics of thermoelectric materials can be summarized as follows: a) low thermal conductivity, which approaches that of amorphous materials, b) indirect electronic band gap, which facilitates large effective mass of the charge carriers and moderate electrical conductivity and c) small electronegativity difference between the constituent elements to maximize the charge-carrier mobility.

Several classes of compounds have been extensively studied with respect to their thermoelectric properties (Figure 1.2).[6,7] The use of thermoelectric materials for waste-heat recovery requires $ZT \geq 1$. Some high-efficiency bulk materials for room-temperature applications are: a) tellurides, like Bi_2Te_3 with $ZT \sim 1$ and its alloys with Sb and Se, b) skutterudites, like $Yb_{0.19}Co_4Sb_{12}$ with $ZT = 0.7$, c) n- or p-type doped PbTe d) half-Heusler alloys, like YNiSb with $ZT = 0.4$. At higher temperatures, other compounds like Zn_4Sb_3 exhibit *ZT* up to 1.5 (700 K).[8]

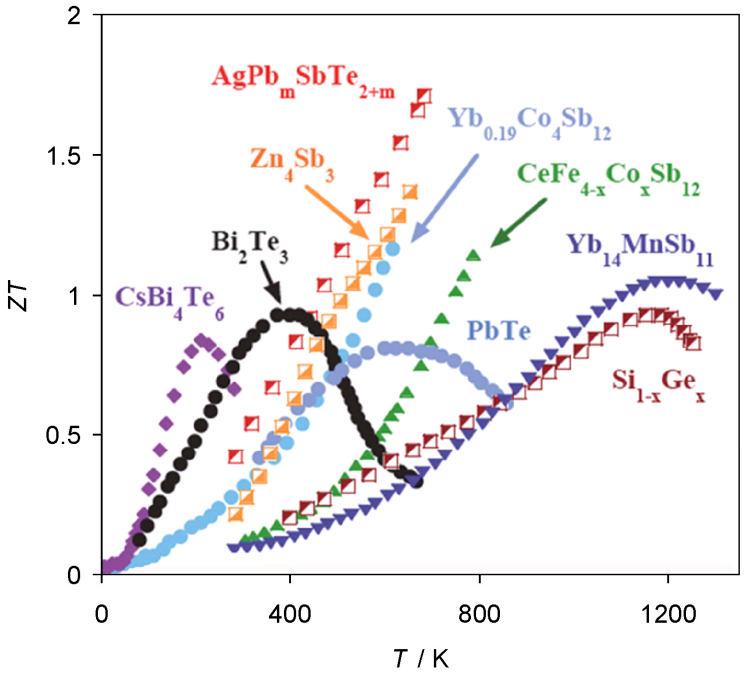

Figure 1.2 High-efficiency thermoelectric materials taken from reference [9].

Nowadays, the design of thermoelectric materials focuses mostly on mechanisms for reducing the thermal conductivity, like nanostructuring. The strategy is to scatter phonons at interfaces, leading to the use of multiphase composites mixed on the nanometer scale.[5] These nanostructured materials can be formed as thin-film superlattices or as intimately mixed composite structures. Indeed, Bi_2Te_3/Sb_2Te_3 superlattices may reach *ZT* up to 2.5 even at room temperature.[10]

1.2 Intermetallic compounds

Intermetallic compounds are chemical species formed by two or more metallic elements with a definite composition.[11,12] In some cases, the term is also used for compounds that contain semimetals like Si and Ge. As the periodic table consists mostly of metals, there is great potential for the formation of numerous binary, ternary and multinary intermetallic compounds. However, intermetallics should be distinguished from conventional alloys. The latter are described as disordered solid solutions or mixtures of more than one solid phases that contain metallic elements of similar sizes and characteristics with no distinct chemical formula.

Most of metals and semimetals have high melting points and therefore the synthesis of intermetallic compounds utilizes arc-melting, high frequency induction heating and flux methods so that sufficient atom diffusion is achieved.[13] The prediction of the composition and structure of the products is sometimes a rather difficult task. Because of the low enthalpies of formation and the presence of diffuse metallic bonds in the solid, even slight variations of the stoichiometry or the reaction conditions (temperature, pressure, grain size of the starting materials) may alter significantly the reaction product.[14] Nevertheless, the exploration in new fields of intermetallic chemistry is nowadays facilitated by the rich experimental knowledge obtained from the phase diagrams.

Among the classes of chemical compounds, intermetallics remain the least understood with respect to their bonding properties. This is mainly due to the fact that some of the features that primarily determine the chemical bonding, such as the degree of valence-electron transfer and localization, vary widely and almost continuously with the composition and the nature of the elements involved. In other words, intermetallic compounds usually do not adhere to the “normal” rules of valence and bonding. The relationship between structure and electronic properties is therefore elucidated with band-structure calculations.[15,16]

Regarding now the practical interest,[17] intermetallic phases fall into the interdisciplinary field of solid-state science (including also pure metals and alloys) with numerous applications that have inextricably connected them to everyday life. Their most useful properties are the following: a) electrical conductivity, ranging from semiconductors to normal conductors and superconductors, b) mechanical strength and chemical inertness for manufacturing most engine parts, tools, light alloys, coating materials, nanocomposites etc., c) ferromagnetism of permanent magnets and electromagnets as well as applications in magnetic-recording media and cooling devices

based on the magnetocaloric effect,[18] d) thermoelectricity, applied mostly on thermocouples and e) optical properties of metal-metal or metal-metalloid semiconductors used for photodetectors or photovoltaic cells.

1.3 Zintl-Klemm concept

Several useful concepts for classifying intermetallic systems have been developed over the years that usually refer to the structure type and the bonding character of the atoms involved.[11] Typical cases of *p*-*d* and *d*-*d* bonding are the Hume-Rothery phases, e.g. CuZn, NiAl, Co_5Zn_{21} and Ag_5Al_3 with variable valence electron concentration (VEC). Another large group of intermetallic compounds with *s*-*d*, *d*-*d*, *s*-*p*, *d*-*d* or *d*-*f* bonding are the Laves phases, e.g. $MgCu_2$, $ZrZn_2$, $CaAl_2$, HfV_2 and UMn_2. Their composition is MM'_2 and they occur in hexagonal and cubic structures, forming Frank-Kasper polyhedra. In the above cases, it is not possible to assess nominal oxidation states to the metal atoms. However, some intermetallic systems composed of alkali- or alkaline earth-metals and *p*-metals possess not only metallic and covalent bonding but also significant ionic character due to electronegativity difference of the atoms. A large class of these polar intermetallic compounds is described by the Zintl-Klemm concept.

The ‘classical’ Zintl phases contain clusters of post-transition elements and isolated alkali- or alkaline earth-metals that occupy interstitials sites. The octet rule applies by assuming full charge transfer from the cations to the polyanionic substructure. In this case, the electrons are localized either in two-center-two-electron (2c-2e) bonds between post-transition atoms or in the form of lone pairs on these atoms. Thus, the Zintl-Klemm concept predicts the composition and structure of numerous polar intermetallics that contain an electropositive element and a moderately electronegative one. This class of compounds has been extensively studied for many decades by E. Zintl, W. Klemm,[19] H. Schäfer, B. Eisenmann,[20] H.-G. von Schnering,[21] J. D. Corbett,[22] R. Nesper[23] and others.[24]

Zintl phases are electronically positioned between intermetallic and insulating valence compounds. Overall, the following features discriminate them from metals, salts and molecular solids: a) covalent anionic substructure, whereas the cations simply provide electrons, b) well defined relationship between their chemical and electronic structures, c) very narrow homogeneity range, d) semiconducting properties with band gap, $\Delta E <$ 2.0 eV and e) mostly diamagnetic behavior but not Pauli paramagnetic. Two typical

examples of Zintl phases are shown in Figure 1.3. NaTl exhibits covalent bonding among the Tl atoms,[25] whereas the Na atoms provide their valence electrons to Tl atoms, resulting in the formal charges $(Na^+)_4(4b\text{-}Tl^-)_4$ and VEC(Na) = VEC(Tl) = 8. The anionic substructure resembles that of diamond. In the case of Cs_4Sn_4, the three-bonded Sn atoms form regular tetrahedra and the isolated Cs cations counterbalance the charge according to the formal electron-counting $(Cs^+)_4(3b\text{-}Sn^-)_4$.[26] The $(Sn_4)^{4-}$ species are electronically isovalent and isostructural to the allotrope of white P.

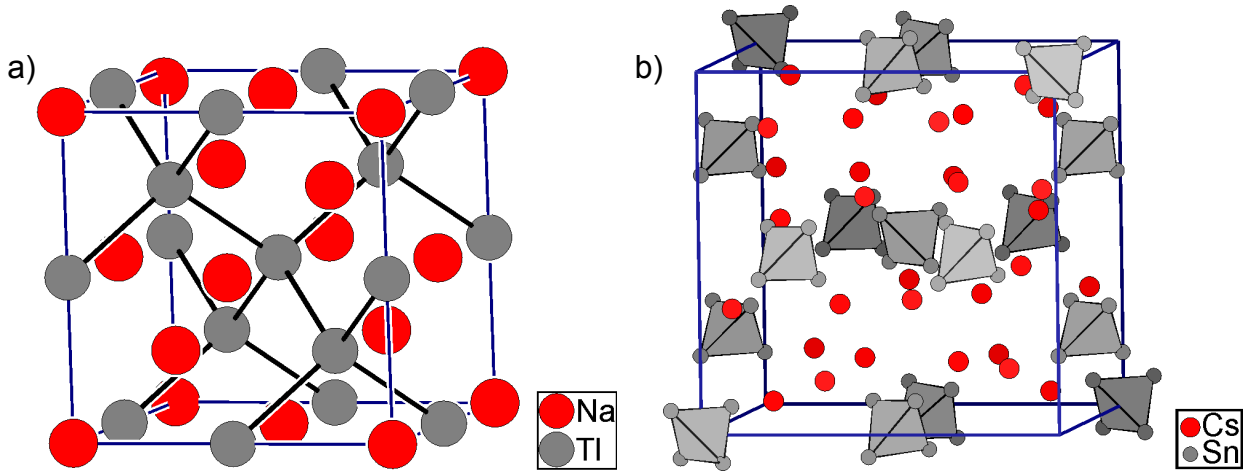

Figure 1.3 Crystal structures of NaTl and Cs_4Sn_4.

Apart from binary intermetallic phases like the ones mentioned above, many new classes of ternary and quaternary compounds that may also contain semimetals are regarded as Zintl phases. These include heteroatomic Zintl anions or phases with polycationic substructure and isolated anions that counterbalance the charge.[22] Some cases of double salts that contain Zintl ions have also been reported, e.g. $[Si_4]^{4-}$ in $Cs_{10}[Si_4][Si_3O_9]$.[27] Most Zintl phases are strong reducing agents and their synthesis requires inert conditions either in solid state or in solution of liquid NH_3 or dimethylformamide. The main criticism on the concept regards the assumption of full charge transfer like in normal salts and the discrepancy that is sometimes observed between the anticipated semiconducting behavior and the measured metallic behavior, for example in NaTl.[28]

1.4 Structure of clathrate compounds

Clathrates (from Latin *clatratus* = encaged) are defined as inclusion compounds with a three-dimensional framework of host species (E) that encapsulate irreversibly in their cavities guest atoms or molecules (G).[29] The first report on clathrate compounds dates back to 1811, when H. Davy passed chlorine gas through water cooled to 275 - 276 K.[30] The exact composition and crystal structure of this chlorine hydrate was determined in 1950's as $(Cl_2)_{6.34}(H_2O)_{46}$.[31,32] Each water molecule is connected to four others via H-bridges and the eight polyhedral cavities per unit cell are partially occupied by Cl_2 molecules. Despite the only weak interaction between H_2O and Cl_2 species, the framework structure may only exist in the presence of the guests. The same behavior has meanwhile been observed for many other hydrate clathrates with G = noble gases, Br_2, CO_2, CH_4, H_2S etc., as well as for the organic clathrates.[33] The latter consist of organic molecules such as urea, phenol and 1,4-hydroquinone that encapsulate other atoms or small molecules.[34] From the environmental aspect, the gas hydrates have attracted considerable attention. There are giant natural deposits of methane hydrate $(CH_4)_8(H_2O)_{46}$ (Figure 1.4) on the deep ocean floor and in permafrost regions.[35,36] Gas hydrates may also be used as a cheaper alternative of gas storage and transport as compared to liquefied gas,[37] whereas the idea of CO_2 captivation from the atmosphere seems very intriguing for the removal of greenhouse gases.[38]

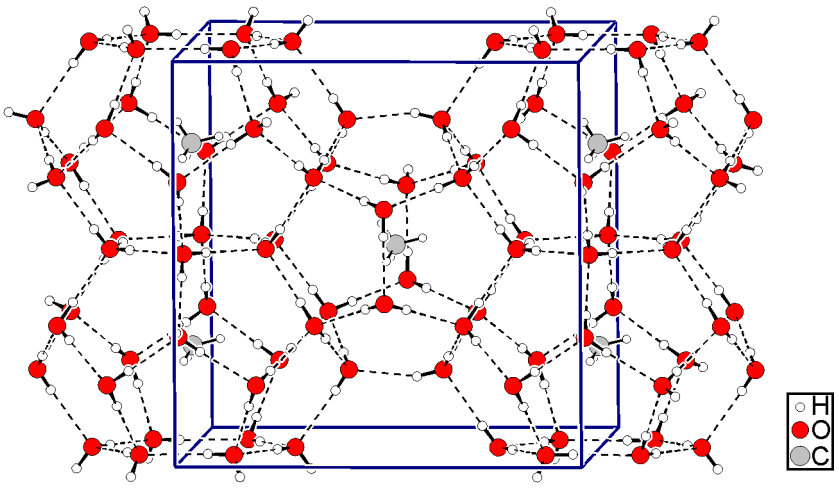

Figure 1.4 Structure of the methane hydrate $(CH_4)_8(H_2O)_{46}$ based on crystallographic and spectroscopic data.[36] The dashed lines denote H-bridges.

In 1965, Na_8Si_{46} and Na_xSi_{136} (x < 11) were synthesized and structurally characterized.[39] Their structure resembles that of the hydrates $(Cl_2)_8(H_2O)_{46}$ and $(Cl_2)_x(H_2O)_{136}$ by replacing H_2O molecules with Si atoms and the Cl_2 units with Na atoms. This breakthrough prompted the research in a new class of compounds named

"semiconducting" or "intermetallic" clathrates (although none of these terms is strictly correct), with the term "semiconducting" being today widely used in the literature. Despite the structural similarity, the semiconducting clathrates differ significantly from their hydrate and organic analogues: a) their framework atoms form covalent bonds instead of weak H-bridges, b) the interaction among framework and encaged atoms is primarily ionic, c) they possess much higher thermal stability, d) they behave as semiconductors or poor metallic conductors and e) they do not occur naturally.

To date, over 150 semiconducting clathrates are known including about 1/3 of the chemical elements (Figure 1.5). As expected, the elements Si, Ge and Sn due to their tetravalency and moderate electronegativity constitute the building blocks of the framework. C atoms do not show the same tendency but rather form fullerenes with strong double bonding and trigonal coordination,[40] whereas Pb atoms with pronounced metallic character and very weak Pb-Pb bonds cannot adopt any big-size cage-like structure.[41] However, many late transition metals, group-13, group-15 elements and Te or I can partially substitute the tetrel atoms towards a variety of new clathrate compounds. The polyhedral cavities are usually occupied by alkali metals, heavier alkaline-earth metals as well as Ce and Eu atoms. Owing to the electronegativity difference between E and G, the framework is negatively charged and therefore these compounds are often called polyanionic clathrates. On the other hand, clathrates that encage electronegative atoms such as Cl, Br and I have also been studied extensively and they are known as polycationic clathrates.[42,43,44]

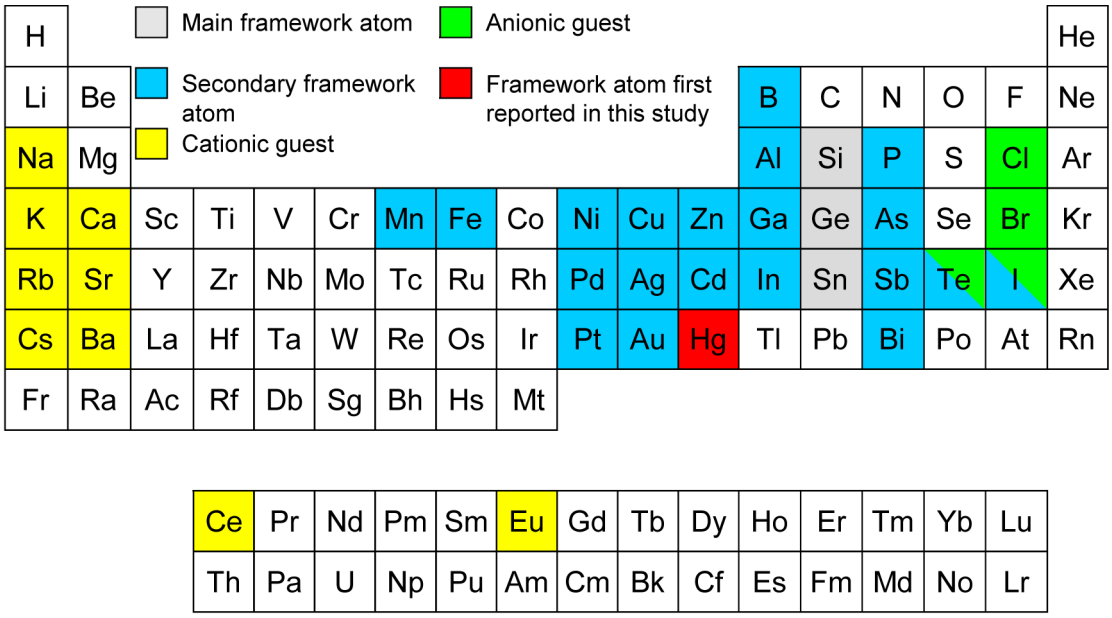

Figure 1.5 Elements found in semiconducting clathrates.

The covalently-bonded framework atoms form polyhedra with regular or distorted pentagonal and hexagonal faces. The following types of polyhedra are found in clathrate compounds (Figure 1.6): a) pentagonal dodecahedron (pdod, $[5^{12}]$) with 20 vertices, b) tetrakaidecahedron (tkad, $[5^{12}6^2]$) with 24 vertices, c) pentakaidecahedron (pkad, $[5^{12}6^3]$) with 26 vertices and d) hexakaidecahedron (pdod, $[5^{12}6^4]$) with 28 vertices. The symbols in brackets denote the number of pentagons and hexagons of the polyhedron. For instance, $[5^{12}6^3]$ refers to a polyhedron with 12 pentagonal and three hexagonal faces.

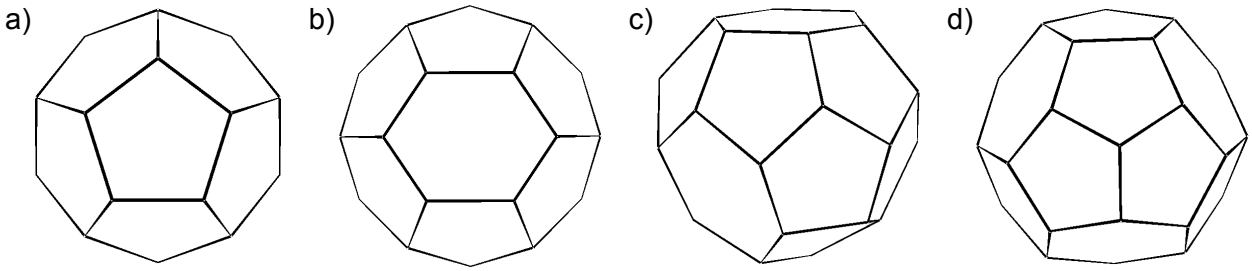

Figure 1.6 Polyhedra in clathrates: a) pentagonal dodecahedron, b) tetrakaidecahedron, c) pentakaidecahedron and d) hexakaidecahedron.

Depending now on the types of polyhedra and their crystal packing, clathrates are classified in nine structure types denoted with Latin numbers I, II,..., IX. Only five types have been reported up to date for the semiconducting clathrates and they are described below. The type-I clathrates with the ideal composition G_8E_{46} consist of pdod and tkad (Figure 1.7). It is the most usual structure type and it crystallizes almost without exception with cubic symmetry. Due to the similar size of framework cavities, this structure is thermodynamically favored over other clathrates for single-type guests, like in Na_8Si_{46}[45] and $[Ge_{38}P_8]Cl_8$[46] (atoms in square brackets compose the host structure).

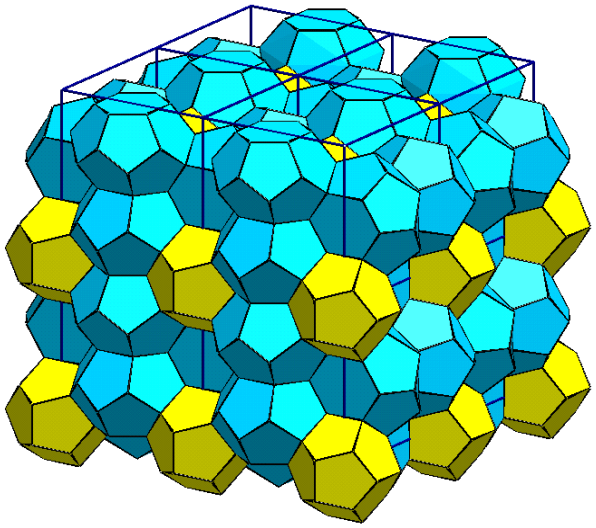

Figure 1.7 The clathrate-I structure (2 × 2 × 2 cell). Strands of tkad (light blue) run orthogonally to one another and the resulting voids are filled with pdod (yellow).

The type-II clathrates with the ideal composition $G_{24}E_{136}$ contain two polyhedra types of very different size, namely pdod and hkad (Figure 1.8). They always crystallize in the cubic, centrosymmetric space group $Fd\bar{3}m$. No single-size cation can fit efficiently enough in both cavities.[47] For this reason and despite the similar composition with the clathrate-I, type-II clathrates may only occur in the presence of two guest-atom types of very different size, i.e. $Na_{16}Cs_8Ge_{136}$[48] or when one type of framework cavities remains free of guest atoms, i.e. $Ba_{16}\square_8[Ga_{32}Sn_{104}]$[49] (□ denotes a vacant position).

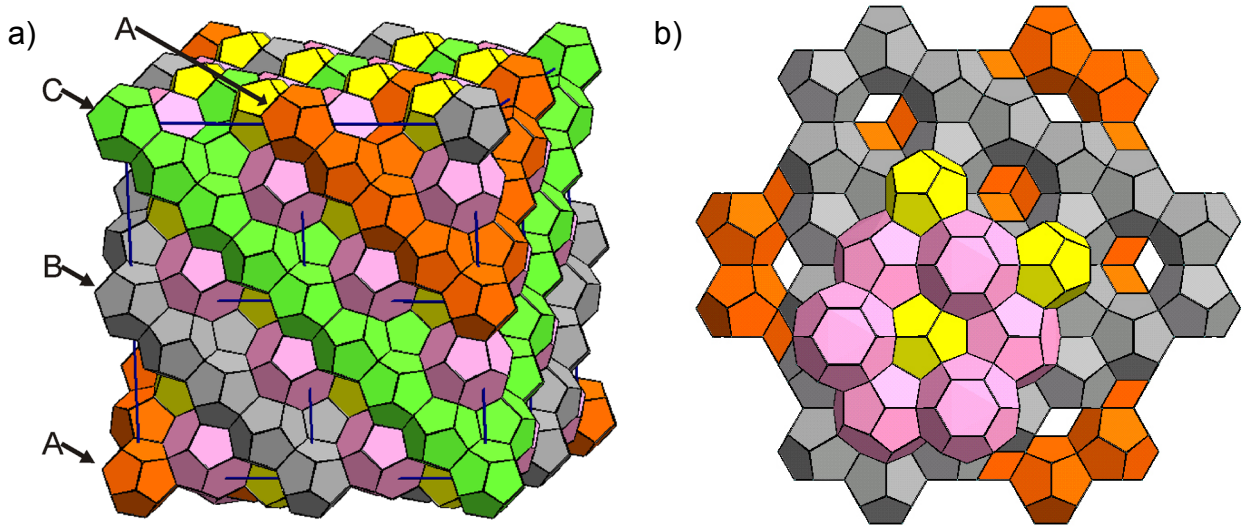

Figure 1.8 a) The clathrate-II structure (2 × 2 × 2 cell). Layers A (orange), B (gray) and C (green) of pdod are stacked along a body diagonal and are interconnected by additional pdod (yellow) and hkad (purple). b) Kagome nets of pdod (layers A and B of (a) from a different view point) interconnected by pdod (yellow). The hkad form a diamond-like network.

The type-III clathrates have the ideal composition $G_{30}E_{172}$ with three kinds of polyhedra, namely pdod, tkad and pkad in the ratio 10 : 16 : 4 (Figure 1.9). Similar to type-II clathrates, the presence of polyhedra with very different size favors the simultaneous encapsulation of more than one atom types. Only three examples have been reported so far and they all crystallize in the tetragonal space group $P4_2/mnm$.[50,51] In the most recent example, namely $[Si_{130}P_{42}]Te_{21.2(2)}\square_{8.8}$, the rather large Te atoms are encaged in the Si/P polyhedra.[51] The pdod are free of guest atoms whereas the tkad are partially occupied and the pkad are fully occupied.

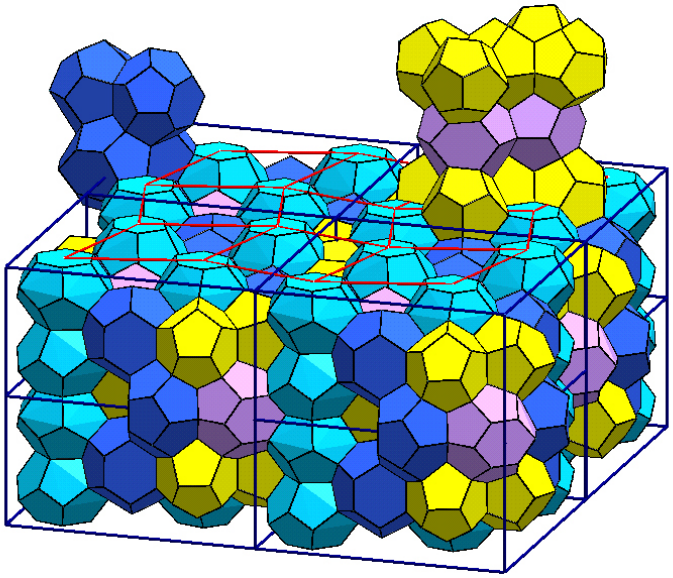

Figure 1.9 The clathrate-III structure (2 × 2 × 2 cell). Strands of tkad (light blue) form a rod packing of distorted squares and rhombi. The distorted square channels are filled with face-sharing tetrahedra of tkad (dark blue). The rhombic channels are filled with a linear chain of alternating groups of five pdod (yellow) and two pkad (purple).

The type-VIII clathrates have the same composition as the type-I, namely G_8E_{46}. However, as shown in Figure 1.10, they contain only one type of filled cavities. These cavities can be described as distorted pentagonal dodecahedra or E_{20+3} polyhedra. Since it is impossible to fill the complete space with this type of polyhedra, the structure also contains smaller 8-vertex cavities, which remain free of guests. The only two examples, $Ba_8[Ga_{16}Sn_{30}]$[52,53] and $Eu_8[Ga_{16}Ge_{30}]$,[54,55] crystallize in the cubic non-centrosymmetric space group *I*43*m*. Both compounds can transform to a high-temperature *β*-modification with the type-I clathrate structure.

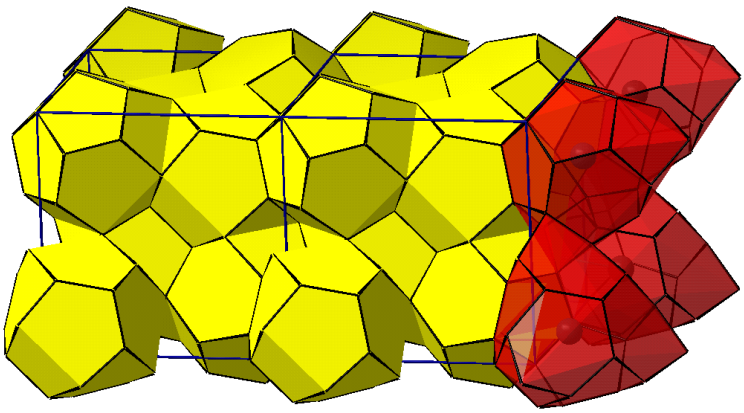

Figure 1.10 The clathrate-VIII structure (2 × 1 × 1 cell). The framework cavities are described either as distorted pdod (yellow) or as (20+3)hedra (semitransparent red).

The type-IX clathrates or “chiral” clathrates crystallize with cubic symmetry having the nominal composition G_8E_{25}. About 15 compounds of this type are currently known,[29,56]

for example $Na_5Rb_3Sn_{25}$[57] and $K_6\square_2Sn_{25}$.[58] The pdod share faces to form a helix about each 4_1 axis, which accounts for the name “chiral” clathrate (Figure 1.11). The helical chains interpenetrate each other and form a three-dimensional network that fills partially the space. Two additional guest atom types occupy the channels between these chains. The type-IX clathrate structure differs essentially from all other clathrates in two ways: a) only 17 out of 25 framework atoms are four-coordinated, whereas the remaining eight atoms are three-coordinated and b) only one out of three crystallographically independent guest sites is encaged by framework atoms.[59]

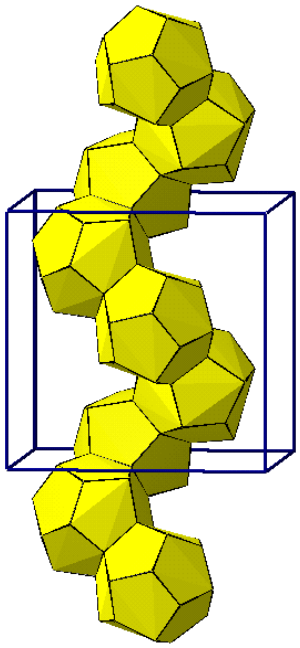

Figure 1.11 The clathrate-IX structure. The pdod (yellow) compose a chiral chain and encapsulate the guest atoms.

It is said that “*nature abhors vacuum*”.[60] Likewise, open framework structures as the semiconducting clathrates show a thermodynamic tendency towards dense states. In other words, the guest atom or ion has to “fit” in the rather rigid covalent cage but on the other hand should not be too small and “escape” from it. The only two cases of guest-free clathrates, namely type-II Na_xSi_{136} ($x = 0.058$)[61] and $\square_{24}Ge_{136}$[62] may only exist as thermodynamically metastable phases. The latter compound accounts also for a new Ge allotrope.[63] However, one should point out that the encapsulation of the guest atoms is an irreversible procedure and no change of composition may take place unless the framework collapses. This distinguishes clathrates from many classes of intercalation compounds such as metal-organic frameworks,[64] zeolites[65,66] and graphite intercalates.[3]

1.5 Physical properties of clathrates compounds

Another crucial point regarding the thermodynamic stability of clathrate compounds is the electronegativity difference and the charge transfer from G to E. In the simplified example of a type-I clathrate with the composition A_8Tt_{46}, the n*s* and n*p* orbitals are completely occupied with the electrons of the three-bonded framework atoms, whereas the high-energy valence electrons of A atoms are partially or fully transferred to the hosts and therefore are delocalised in the antibonding nσ^* states.[24] Thus, the conduction band is occupied and the compound should exhibit metallic properties.

However, metallic character holds actually only for a few clathrates, e.g. Ba_8Si_{46}[67] and $Na_{16}Cs_8Ge_{136}$.[48] The majority shows typical semiconducting properties with band gaps of 0.5 - 2 eV. This is attributed to: a) the introduction of defects in guest or host sites and/or b) the substitution of the framework with electron-poorer atoms. In the first case, the removal of one Tt atom from A_8Tt_{46} would reduce the valence band by four electrons and the four remaining 3b-Tt atoms that surround the vacancy would attract electrons from the A atoms, to fill their valence shell (formal charge –1). Now, upon removal of two Tt atoms, eight electrons are missing and the polyanionic framework can fully compensate the eight electrons of the A atoms. This leads to the electron-counting $(A^+)_8[(4b\text{-}Tt^0)_{36}(3b\text{-}Tt^-)_8]$ and therefore complies with the Zintl-Klemm concept.

Theoretical investigations for the type-I K_8Sn_{46-x}[68] (Figure 1.12) and Cs_8Sn_{46-x}[69] have shown that the presence of two defects in the Sn framework is energetically favored, confirming the experimentally found composition and semimetallic behavior for A_8Sn_{44} (A = K, Rb, Cs)[70] and K_8Ge_{44}[71] clathrates. Generally, when the energy of the electrons in the conduction band overcomes the energy cost of breaking E-E bonds, then the vacancy formation is favored. Taking into account the decreasing bond strength of the tetrel atoms,[41] it is reasonable that the Si clathrates are usually metallic with no defects in their structure, whereas binary Ge and Sn clathrates often show framework defects and semiconducting properties.[29]

The second and most common class of semiconducting clathrates is based on the substitution of the framework with elements other than Si, Ge and Sn. The extra electrons of the G atoms counterbalance the lack of valence electrons of the dopant atoms. The choice of the dopant(s) and the extent of substitution have led to a variety of ternary and quaternary compounds with tunable electronic structure. This has been in the last two decades the main focus in the clathrate research along with their potential use as thermoelectric materials.

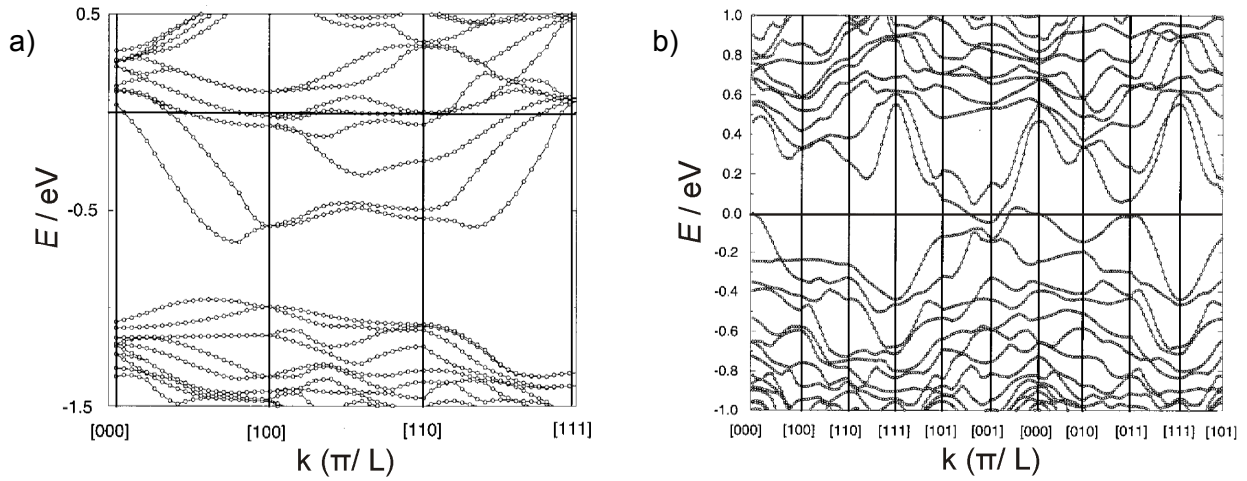

Figure 1.12 Band structures for K_8Sn_{46} (a) and K_8Sn_{44} (b) taken from reference [68]. The horizontal lines indicate the Fermi level.

The thermoelectric efficiency of the clathrates has been proposed by G. Slack in terms of the Phonon Glass - Electron Crystal concept (PGEC).[1] The basic hypothesis is that a semiconducting host framework has high Seebeck coefficient and electrical conductivity (like in crystals), while the extreme thermal motion - "rattling" of the loosely-bound guest atoms scatters efficiently the heat-carrying phonons and reduces the thermal conductivity (like in glasses).[72,73] Some clathrate compounds, such as the type-I $Sr_8Ga_{16}Ge_{30}$, exhibit indeed considerable thermoelectric efficiency at room temperature (ZT = 0.3).[74]

1.6 Scope of this work

The present study deals with the synthesis, characterization and physical properties of Sn and Ge clathrates. The main aim is to investigate the ordering of the Sn vacancies in the defect type-I clathrates A_8Sn_{44}. Primarily, this is achieved with the aid of the modern X-ray diffraction techniques that render the crystal-structure determination a rather fast and routine work. The thermodynamics of the system are studied by differential thermal analysis and heat-capacity measurements whereas the chemical environment of the Sn atoms is analysed with multi-temperature Mössbauer and Raman spectroscopy. The mixing of Rb and Cs atoms in $Rb_xCs_{8-x}Sn_{44}$ and its effect on the stability of the clathrates are also discussed. In an attempt to elucidate the structure-properties relationship, magnetic and thermoelectric measurements as well as inelastic neutron-scattering experiments are performed on A_8Sn_{44} (A = Rb, Cs).

The second part of the thesis refers to the substitution of the Sn or Ge framework with

Hg atoms. Noteworthy, no Hg-substituted clathrate compounds have been up to now reported in the literature. Different preparation routes, like the fusion of the elements or the use of A_4Ge_9 (A = K, Rb) as precursors, are applied. Apart from the structural determination of the new compounds, attention is also paid to the purification and crystallization of the products as the physical measurements necessitate pure-phase samples with minimum ratio of surface-to-bulk atoms. Finally, the application of the Zintl-Klemm concept on these compounds is discussed, in the light of the experimental results.

1.7 References

[1] G. Slack *CRC Handbook of Thermoelectrics*, CRC Press, **1995**.

[2] F. DiSalvo *Science* **1999**, *285*, 703.

[3] A. R. West *Solid State Chemistry and its Applications*, Wiley, **1984**.

[4] A. Shevelkov *Russ. Chem. Rev.* **2008**, *77*, 1.

[5] G. J. Snyder, E. Toberer *Nature Mater.* **2008**, 105.

[6] G. S. Nolas, J. Poon, M. G. Kanatzidis *MRS Bulletin* **2006**, *31*,199.

[7] S. Kauzlarich, S. Brown, G. Snyder *Dalton Trans.* **2007**, 2099.

[8] G. J. Snyder, M. Christensen, E. Nishibori, T. Caillat, B. B. Iversen *Nature Mater.* **2004**, 458.

[9] www.ipm.fraunhofer.de/fhg/ipm_en/extra/bigimg/technologien/thermoelektrik/wissenwertes/zt-wert.jsp

[10] H. Böttner, G. Chen, R. Venkatasubramanian *MRS Bulletin* **2006**, *31*, 211.

[11] E. Holleman, N. Wiberg *Lehrbuch der Anorganischen Chemie* 101. Auflage, Walter de Gruyter **1995**.

[12] O. Gourdon, D. Gout, G. J. Miller *Encyclopedia of Condensed Matter Physics* **2005**, 409.

[13] M. G. Kanatzidis, R. Pöttgen, W. Jeitschko *Angew. Chem. Int. Ed.* **2005**, *44*, 6996.

[14] M. G. Kanatzidis *Acc. Chem. Res.* **2005**, *38*, 361.

[15] G. J. Miller *Eur. J. Inorg. Chem.* **1998**, 523.

[16] R. Hoffmann *Angew. Chem.* **1987**, *99*, 871.

[17] J. H. Westbrook, R. L. Fleischer *Intermetallic Compounds Volume 2 – Practice*, Wiley, **1995**.

[18] G. J. Miller *Chem. Soc. Rev.* **2006**, *35*, 799.

[19] W. Klemm *Prog. Chem. Soc.* **1959**, 329.

[20] H. Schäfer, B. Eisenmann, W. Müller *Angew. Chem.* **1973***, 85*, 742.

[21] H.-G. von Schnering *Angew. Chem.* **1981**, *93*, 44.

[22] J. D. Corbett *Chem. Rev.* **1985**, *85*, 383.

[23] R. Nesper *Prog. Solid State Chem* **1990**, *20*, 1.

[24] S. Kauzlarich *Chemistry, Structure and Bonding of Zintl Phases and Ions*, VCH Publishers, Inc. **1996**.

[25] E. Zintl, W. Dullenkopf *Z. Phys. Chem.* **1932**, *B16*, 195.

[26] C. Hoch, C. Röhr *Z. Anorg. Allg. Chem.* **2002**, *628*, 1541.

[27] S. Hoffmann, T. F. Fässler, C. Hoch, C. Röhr *Angew. Chem.* **2001**, *113*, 4527.

[28] P. C. Schmidt *Struct. Bonding* **1987**, *65*, 91.

[29] K. Konvir, A. Shevelkov *Russ. Chem. Rev.* **2004**, *73*, 923.

[30] H. Davy *Philos. Trans. R. Soc. London* **1811**, *101*, 155.

[31] W. Claussen *J. Chem. Phys.* **1951**, *19*, 259.

[32] M. Stackelberg, H. Müller *J. Chem. Phys.* **1951**, *19*, 1319.

[33] H. Powell *J. Am. Chem. Soc.* **1948**, 61.

[34] L. Mandelcorn *Chem. Rev.* **1959**, *59*, 827.

[35] R. G. Rothwell, J. Thomson, G. Kähler *Nature* **1998**, *392*, 377.

[36] J. Schicks *Chem. Unserer Zeit* **2008**, *42*, 310.

[37] P. D. Profio, S. Arca, R. Germani, G. Savelli *J. Fuel Cell Sci. Technol.* **2007**, *4*, 49.

[38] T. Ohsumi *J. Oceanogr.* **2004**, *60*, 693.

[39] J. Kasper, P. Hagenmuller, M. Pouchard, C. Cros *Science* **1965**, *150*, 1713.

[40] J. Yang, J. S. Tse, Y. Yao, T. Iitaka *Angew. Chem. Int. Ed.* **2007**, *46*, 6275.

[41] F. Cotton, G. Wilkinson, C. Murillos, M. Bochmann *Advanced Inorganic Chemistry*, Wiley, **1999**.

[42] H.-G. von Schnering, H. Menke *Angew. Chem. Int. Ed. Engl.* **1972**, *11*, 43.

[43] H.-G. von Schnering, H. Menke *Z. Anorg. Allg. Chem.* **1973**, *395*, 223.

[44] M. Shatruk, K. Kovnir, M Lindsjö, I. Presniakov, L. Kloo, A. Shevelkov *J. Solid State Chem.* **2001**, *161*, 233.

[45] E. Reny, P. Gravereau, C. Cros, M. Pouchard *J. Mater. Chem.* **1998**, *8*, 2839.

[46] H Menke, H.-G. von Schnering *Naturwissenschaften* **1972**, 59, 420.

[47] M. Beekman, G. Nolas *J. Mater. Chem.* **2008**, *18*, 842.

[48] S. Bobev, S. C. Sevov *J. Am. Chem. Soc.* **1999**, *121*, 3795.

[49] R. Kröner, K. Peters, H.-G. von Schnering, R. Nesper *Z. Kristallogr. NCS* **1998**, *213*, 664.

[50] S. Bobev, S. Sevov *J. Am. Chem. Soc.* **2001,** *123*, 3389.

[51] J. Zaikina, K. Kovnir, F. Haarmann, W. Schnelle, U. Burkhardt, H. Borrmann, U. Schwarz, Yu. Grin, A. Shevelkov *Chem. Eur. J.* **2008**, *14*, 5414.

[52] B. Eisenmann, H. Schäfer, R. Zagler *J. Less-Common. Met.* **1986**, *118*, 43.

[53] Y. Li, J. Gao, N. Chen, Y. Liu, Z. P. Luo, R. H. Zhang, X. Q. Ma, G. H. Cao *Physica B* **2008**, *403*, 1140.

[54] S. Paschen, W. Carrillo-Cabrera, A. Bentien, V. H. Tran, M. Baenitz, Yu. Grin, F. Steglich *Phys. Rev. B* **2001**, *64*, 214404.

[55] S. Srinath, J. Gass, D. J. Rebar, G. T. Woods, H. Srikanth, G. S. Nolas *J. Appl. Phys.* **2006**, *99*, 08K902.

[56] H.-G. von Schnering, A. Zürn, J.-H. Chang, M. Baitinger, Yu. Grin *Z. Anorg. Allg. Chem.* **2007**, *633*, 1147.

[57] S. Bobev, S. C. Sevov *Inorg. Chem.* **2000**, *39*, 5930.

[58] T. F. Fässler, C. Kronseder *Z. Anorg. Allg. Chem.* **1998**, *624*, 561.

[59] T. F. Fässler *Z. Anorg. Allg. Chem.* **1998**, *624*, 569.

[60] G. Ozin, A. Arsenault *Nanochemistry, A Chemical Approach to Nanomaterials*, RSC Publishing **2005**.

[61] A. Ammar, C. Cros, M. Pouchard, N. Jaussaud, J.-M. Bassat, G. Villeneuve, M. Duttine, M. Ménétrier, E. Reny *Solid State Sciences* **2004**, *6*, 393.

[62] A. Guloy, R. Ramlau, Z. Tang, W. Schnelle, M. Baitinger, Yu. Grin, *Nature* **2006**, *443*, 320

[63] T. F. Fässler *Angew. Chem. Int. Ed.* **2007**, *46*, 2.

[64] A. K. Cheetham, C. N. Rao, R. K. Feller *Chem. Commun.* **2006**, 4780.

[65] J. Pérez-Ramírez, C. H. Christensen, K. Egeblad, C. H. Christensen, J. C. Groen *Chem. Soc. Rev.* **2008**, *37*, 2530.

[66] A. Müller, H. Reuter, S. Dillinger *Angew. Chem. Int. Ed.* **1995**, *34*, 2328.

[67] D. Connetable, V. Timoshevskii, B. Masenelli, J. Beille, J. Marcus, B. Barbara, A. M. Saitta, G.-M. Rignanese, P. Melinon, S.Yamanaka, X. Blase *Phys. Rev Lett.* **2003**, 247001.

[68] L. Mollnitz, N. Blake, H. Metiu *J. Chem. Phys.* **2002**, *117*, 1302.

[69] C. Myles, J. Dong, O. Sankey *Phys. Rev. B* **2001**, *64*, 165202.

[70] J. T. Zhao, J. Corbett *Inorg. Chem.* **1994**, *33*, 5721.

[71] G. Ramachandran, P. McMillan, J. Dong, O. Sankey *J. Solid State Chem.* **2000**, *154*, 626.

[72] B. Iversen, G. Nolas, G. Stucky *J. Solid State Chem.* **2000**, *149*, 455.

[73] C. Myles, J. Dong, O. Sankey *Phys. Stat. Sol. B* **2003**, *239*, 26.

[74] G. S. Nolas, J. L. Cohn, G. A. Slack, S. B. Schujman *Appl. Phys. Lett.* **1998**, *73*, 178.

2. Experimental section

2.1 Synthesis

The starting materials used for the synthesis in this work are listed in Table 2.1. All manipulations of the reactants were carried out in a glove box (Mbraun 20 G) under Ar atmosphere (purity 99.996%) with O_2 and H_2O levels below 1 ppm per volume. Air-stable reactants were dried under dynamic vacuum (10^{-3} mbar) at 423 K over night prior to use. Air- and moisture-sensitive reactants were stored in the glove box and were used as received. For the alkali metals, surface impurities were removed with a scalpel immediately before loading. Most of the syntheses took place in arc-welded Nb crucibles. Pieces of 4 - 5 cm long tubes (external diameter 10 mm, wall width 0.5 mm) were cut from a longer pipe, washed with concentrated HNO_3 and deionized water in ultrasonic bath and subsequently dried in an oven at 373 K over night. The metal tubes were then pressed together on one end with pliers and sealed with an arc-welder under Ar atmosphere at reduced pressure (400 mbar). The mixture of reactants was loaded in containers previously sealed on one end. The containers were then pressed on the open side with pliers and sealed by arc-welding under Ar. The ampoules were placed in small quartz tubes (about 10 cm long) that were then enclosed in larger quartz tubes with 80 cm length. The tubes were subsequently evacuated and taken into the furnaces.

Table 2.1 Starting materials used for the synthesis.

Substance	Manufacturer	Form	Purity (%)
K	Merck	Pieces	99
Rb	ABCR	Ampoule	>99.9
Cs	Riedel de Haën	Ampoule	>98
WO_3	Aldrich	Powder	>99
Hg	Aldrich	Liquid	>99.99
HgO	Alfa	Powder	99
Ge	ChemPur	Powder (< 250 μm)	99.99
Sn	ChemPur	Granules	99.999

The thermal treatment was carried out in tubular computer-controlled ovens. The ovens (Model LOBA, HTM Reetz GmbH, Berlin) have maximum operating temperature of 1473 K. A type-S thermoelement monitors the actual temperature in the middle of the oven, which is considered as uniform zone without significant temperature variation. For safety reasons, about half the length of the quartz tube was placed in the frunace and

the other half outside for the condensation of gases, e.g. alkali metals or Hg, that might leak in case the Nb ampoule cleaved.

The syntheses were performed according to the temperature programs in Figure 2.1. The first method was used for single-step reactions whereas the second for reactions with subsequent annealing of the products in order to increase their yield and crystallinity. Typical reaction temperatures were 870 - 1100 K with 1 - 3 days duration and for the annealing steps 620 - 770 K with 5 - 30 days duration. All these parameters as well as specific deviations from this general synthetic procedure are discussed in detail in the preparative parts of each chapter.

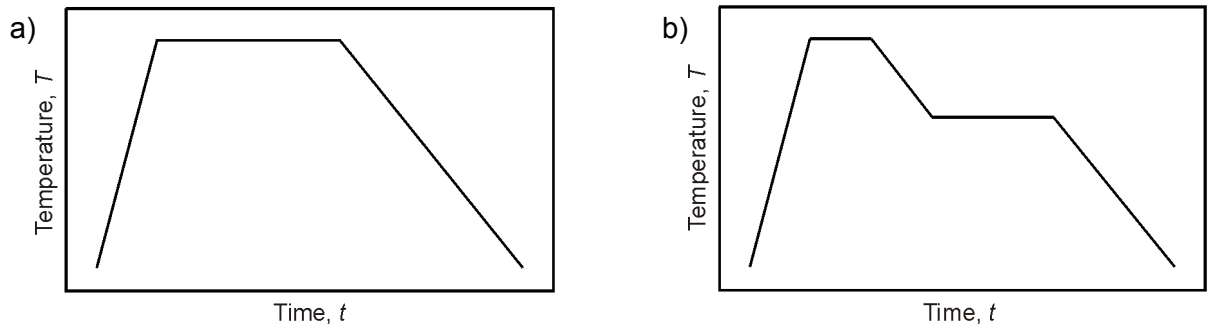

Figure 2.1 Typical thermal-treatment programs: a) one-step reaction and b) two-step reaction.

The crucibles were subsequently opened in the glove box under protecting Ar atmosphere because some of the products were sensitive to air and moisture. The outcome of all reactions was monitored by X-ray powder diffraction. Nb was chosen as reaction container for its high chemical inertness and mechanical properties. It does not form alloys with alkali or transition metals up to 1300 K, but it may react with Ge or Sn towards $NbGe_2$ or Nb_3Sn, respectively. On the other hand, Nb ampoules are relatively easy to arc-weld (compared to Ta and W) and may also tolerate very high vapor pressures. However, certain reactions that required lower temperatures, e.g. the synthesis of A_4Ge_9, were performed in open corundum crucibles that were in turn enclosed in steel autoclaves. Further synthetic or purification procedures below 470 K took place in Schlenk tubes under vacuum or Ar atmosphere.

2.2 X-ray diffraction analysis

Photons interact in many different ways with matter. However, X-rays due to their very small wavelength may be elastically scattered by the electrons of crystalline materials and produce a secondary radiation of unique importance. These so-called reflections

correspond to one set of evenly spaced planes within the crystal, whose position and intensity can be accurately monitored by photographic films or other detectors. The computational combination of the directions of the crystal in the primary monochromatic X-ray beam and the corresponding reflections may determine the size and symmetry of the unit cell, the exact coordinates of the atoms as well as the extent of their oscillation in the solid. With the aid of modern, high-intensity X-rays sources, accurate X-ray detectors and fast computer processors, the crystal-structure determination by X-ray diffraction has become one of the most significant methods in chemical research.[1]

2.2.1 Single crystal X-ray diffraction

Single crystals were selected with a needle in a glove box equipped with an optical microscope (Leica, Germany), fixed at the top of a 0.1 mm glass capillary (Hilgenberg, 80 mm length) with dry silicon grease, which was in turn inserted into another 0.3 mm capillary and sealed with melted wax. The capillaries were dried prior to use at 373 K under dynamic vacuum.

The data collections were performed on the following diffractometers using graphite-monochromated Mo-Kα radiation (λ = 0.71073 Å): a) Stoe-IPDS II equipped with a rotating anode (Nonius, FR591), 2-circle goniometer, 180° ω range, unlimited φ range, image plate detector system (IPDS) with active imaging plate diameter of 340 mm and $2\theta_{max}$ = 77° and open-flow N_2 blower (Oxford cryostream cooler 700) for the temperature range 90 - 400 K, b) APEX II using also a rotating anode (Nonius, FR591) and a CCD detector and c) Oxford Xcalibur3 equipped with a CCD detector and an open-flow N_2 blower (CryojetXL, Oxford Cryosystems) for the temperature range 90 - 300 K. The unit-cell determination and data reduction were carried out with the corresponding software.[2,3] Numerical[4] or multi-scan[5] absorption corrections were applied to the data.

The definitions of the parameters used in the crystal-structure determination by X-ray diffraction are summarized in Table 2.2. The structures were solved by direct methods and refined by least-squares on F^2 with the program package SHELXTL.[6] This contains, among others, the subroutines XPREP for space group determination, SHELXS for structure solution and SHELXL for structure refinement. Note that the occupation factors for defects and split positions were coupled via the PART command for disordered groups. For the pictorial representation of the crystal structures, the software Diamond 3.1f was used.[7]

Table 2.2 Definition of parameters in the X-ray diffraction analysis of single crystals.

Error	$\Delta_1 = \|\|F_o\| - \|F_c\|\|$ and $\Delta_2 = \|F_o^2 - F_c^2\|$ F_o = observed structure amplitude F_c = calculated structure amplitude from the structure model
Conventional R factor or residual factor on F	$R_1 = \frac{\sum_{hkl} \Delta_1}{\sum_{hkl} F_o}$ h, k, l = Miller indices
Weighted R factor	$wR_2 = \sqrt{\frac{\sum_{hkl} w\Delta_2^2}{\sum_{hkl} w(F_o^2)^2}}$ $w = \frac{1}{\sigma^2(F_o^2) + (a\,P)^2 + b\,P}$ a, b = weighting coefficients $\sigma(F_o)$ = standard uncertainty on F_o $P = \frac{1}{3}\max(0, F_o^2) + \frac{2}{3}F_c^2$
Goodness of Fit for the model	$S = \sqrt{\frac{\sum_{hkl} w\Delta_2^2}{m - n}}$ m = number of reflections n = number of refined parameters
Internal R factor	$R_{int} = \frac{\sum_{hkl} (F_o^2 - \overline{F_o^2})}{\sum_{hkl} F_o^2}$
Isotropic displacement parameter, U_{iso}	$f' = f \exp\left(-8\pi^2 U_{iso} \frac{\sin^2\theta}{\lambda^2}\right)$ f = atomic scattering factor f' = corrected atomic scattering factor (to include atomic vibration)
Anisotropic displacement parameter, U_{ij}	$f' = f \exp\left(-2\pi^2(U_{11}h^2a^{*2} + U_{22}k^2b^{*2} + U_{33}l^2c^{*2} + 2U_{23}klb^*c^* + 2U_{13}hla^*c^* + 2U_{12}hka^*b^*\right)$ a^*, b^*, c^* = reciprocal unit-cell vectors
Equivalent isotropic displacement parameter	U_{eq} = 1/3 of the trace of the orthogonalized U^{ij} tensor

2.2.2 Powder X-ray diffraction

Powder X-ray diffraction experiments were performed for the phase analysis of the reaction products. The samples were finely ground in an agate mortar to homogeneous powders. Depending on their air-stability, small amounts of crystallites were either fixed on scotch tape (transmission geometry) or filled into glass capillaries with internal diameter 0.3 mm (Debye-Scherrer geometry). The filled capillaries were then sealed with melted wax under Ar atmosphere.

The powder diagrams were collected on a Stoe STADI P2 diffractometer (Ge(111) monochromator for Cu-Kα radiation with λ = 1.54056 Å) equipped with a linear position sensitive detector. The typical angular range was $10° \leq 2\theta \leq 90°$ and the measuring time at least 12 hours to obtain an adequate signal-to-background ratio. The calculation of

theoretical powder diagrams as well as the data processing of the experimental powder diagrams was performed with the Stoe package WinXPow.[8] Phase analyses were done using the imbedded databank containing crystallographic data from original literature or from the ICSD[9] and the Pearson[10] databases. In some cases, Rietveld analyses of the powder diagrams were performed with the Fullprof package.[11] For all refinements, the peak shape was chosen as pseudo Voigt and the background was linearly interpolated among refineable points.

2.2.3 Synchrotron resonance powder X-ray diffraction

Synchrotron is an advanced type of cyclic particle accelerator in which strong magnetic and electric fields are carefully synchronized with the travelling particle beam. As the particles (electrons or protons) reach the bends at relativistic speeds, a wide spectrum of photons is emitted at the tangent to the orbit. For the purpose of the diffractometry studies, only photons of wavelength in the range of X-rays are used to irradiate the powdered sample. The primary beam, expect for the tunable wavelength, is highly collimated and its intensity is at least two orders of magnitude greater than any laboratory X-ray source.

Multi-temperature synchrotron powder diffraction experiments for A_8Sn_{44} (A = Rb, Cs) were carried out at the BL02B2 beamline of the SPring-8 synchrotron radiation research facility in Japan,[12] with using a large Debye-Scherrer camera with an image plate detector. Powder particles with homogeneous size were packed under Ar atmosphere in 0.1 mm glass capillaries to minimize absorption. The wavelength of the synchrotron radiation for various diffraction measurements was determined using a CeO_2 standard (*a* = 5.411102 Å). Rietveld refinements of the synchrotron diffraction data were done using the Fullprof package.[11]

2.3 Differential thermal analysis

The differential thermal analysis (DTA) monitors the temperature difference between the sample and a thermally indifferent substance, as both are simultaneously heated or cooled in an oven. The method therefore allows the determination of reaction temperatures, melting, boiling or decomposition points as well as an almost quantitative measurement of the enthalpy change (exothermic or endothermic) related to the

transition, with the use of appropriate standards.

The thermal analyses were carried out in the temperature range 298 - 1373 K using custom-made Nb containers for the sample and as reference crucible (Netzsch DSC 404C). The Nb crucibles were loaded with 50 - 300 mg of sample and then closed either by arc-welding or with a screw lid. The DTA curves were recorded under continuous Ar flow (50 mL min^{-1}) to prevent the corrosion of the crucibles at high temperatures. In most cases, two cycles of heating and cooling were performed. After the DTA experiments, the crucibles were opened in the glove box and the products were again analyzed by X-ray powder diffraction. The results of the thermodiagrams were evaluated with the software Netzsch - Proteus Analysis[13] and finally compared to the literature data of binary phase diagrams.[14] For the enthalpy determination of the studied transitions, calibration was carried out via known latent heats for the melting points of naphthalene (T_m = 353.4 K, ΔH_m = –147 J g^{-1}), In (T_m = 429.7 K, ΔH_m = –28.6 J g^{-1}), β-Sn (T_m = 505 K, ΔH_m = –60.5 J g^{-1}) and Al (T_m = 933.4 K, ΔH_m = –397 J g^{-1}) in the heating-cooling rate of ±2 K min^{-1}.

2.4 Scanning electron microscopy

By interference of an electron beam with matter different information, such as secondary electrons, backscattered electrons or X-rays can be detected. Based on the breakthrough invention of E. Ruska,[15] the scanning electron microscope (SEM) uses the interference of electrons with matter to generate a picture. The sample is scanned by high-energy electrons under vacuum. Secondary electrons are emitted and then collected by a positively charged detector which then generates a picture. The more secondary electrons are detected, the brighter the picture becomes. Due to Coulomb interactions the primary electrons can repulse bonded electrons from the samples atoms. However, the secondary electrons have much lower kinetic energies (10^3 - 10^4 times lower) compared to the primary electrons due to the short time for the Coulomb repulsion, so only those that are near the surface (1 - 10 nm) can leave the sample and be detected. The contrast of the sample is caused by the surface topology. Areas with slopes, edges etc. exposed to the same electron beam have a bigger surface and volume from which secondary electrons can be emitted.

Additionally, scanning electron microscopes perform an energy dispersive X-ray analysis (EDX). The fast primary electrons may generate X-rays, whose energy

corresponds to the energy difference of the shells involved in the electron-hole recombination. These X-rays are collected and sorted by intensity and energy. As the radiation is characteristic for each element, the sample's composition can be semi-quantitatively determined. Detection limits range from 10^{-10} to 10^{-14} g for elements with Z > 6. The X-ray spectra of lighter elements are absorbed by the window material covering the detector. EDX analyses were carried out on a JEOL 5900 LV scanning electron microscope operating at 20 kV with a Si(Li) detector. Crystallites of the samples were selected in the glovebox and fixed on a carbon pad on a cylindrical Al-sample holder. During transferring the holder into the microscope's chamber, the samples were briefly exposed to air. Standard measurement times for EDX were 5 minutes for acceptable statistics.

2.5 Mössbauer spectroscopy

The atomic nuclei may undergo a variety of energy-level transitions, often associated with the emission or absorption of photons in the wavelength range of the γ-rays. A free nucleus will conserve its momentum and recoil when the γ-ray is emitted or absorbed. The energy difference between absorbed and emitted photons due to this recoil eventually prevents resonance with the rest nuclei of the system. However as R. Mössbauer discovered,[16] a nucleus in a rigid, solid matrix has a much greater effective mass and therefore the recoil energy is too low to be transmitted as a phonon. If all nuclei are identical then resonance is achieved and a single absorption line of the γ-rays is produced.

The aim of Mössbauer spectroscopy is to accurately determine the transition energies that are influenced by the tiny hyperfine interactions between the nuclei and its environment, both electronic and magnetic. It requires extremely high resolution to detect such fluctuations (e.g. ±5 10^{-9} eV in 14.4 keV for ^{57}Fe) and only few isotopes with low-energy and long-lived excited states can be practically detected. In the frame of this study, the ^{119}Sn spectra of A_8Sn_{44} (A = Rb, Cs) were recorded using a conventional constant-acceleration Mössbauer spectrometer. The samples were measured at 77, 293, 330 and 363 K, with the $Ca^{119m}SnO_3$ source maintained at room temperature. The isomer shifts were referenced to $CaSnO_3$.

2.6 Raman spectroscopy

The scattering of light takes place when an electromagnetic wave encounters matter in solid, liquid or gas state. During the interaction, the electron orbits are perturbed periodically with the same frequency as the electric field of the incident photon. This oscillation or perturbation of the electron cloud results in a periodic separation of charge within the molecules, which is called an induced dipole moment. The oscillating induced dipole moment is manifested as a source of electromagnetic radiation, thereby resulting in scattered light. The majority of light scattered is emitted at the identical frequency of the incident light, a process referred to as Rayleigh scattering. However, a very small percentage of photons is scattered at different frequencies due to the energy loss or gain between vibrational levels of the matter. The corresponding Stokes or anti-Stokes lines are monitored in Raman spectroscopy and provide valuable information about the vibrational states of the compounds (always referring to the ground electronic state).[17]

The backscattered Raman spectra were recorded on a spectrometer (JASCO NR1800) equipped with a triple polychromator and a CCD detector. Radiation of 532 nm from a solid-state laser (Verdi2W) was incident on the sample with a power of 5 mW. The illuminated spot was less than 5 μm in size and the resolution of the spectra about 1 cm^{-1}. High-temperature measurements up to 373 K were performed with a resistive heater and a thermocouple fixed close to the sample under vacuum. In this measurement, the laser power was 10 mW and the spot size about 10 μm.

2.7 Magnetic measurements

A superconducting quantum interference device (SQUID) is used to measure very small magnetic fields down to flux densities of 10^{-14} T and magnetic susceptibility. Therefore, magnetic behaviors such as different forms of paramagnetism, diamagnetism, superconducting transitions, magnetic couplings and field or temperature dependencies of a chemical compound can be determined.[18] The measurements were performed on a MPMS XL 5 (Quantum Design) magnetometer with a temperature range of 1.7 - 400 K and magnetic fields up to 5 T. Approximately 30 mg of the samples were tightly sealed into a gelatin capsule and fixed in the center of a plastic straw (contact with ferromagnetic materials like spatules was avoided as far as possible). Prior to the measurement, the permanent field of the sample chamber was checked with a Hall probe and compensated with a polarized field. Regarding superconductive transitions,

the samples were cooled in the absence of a magnetic field and then heated (shielding) and cooled (Meissner) with an external field of 10 - 20 G. In some cases, the samples were checked afterwards for decomposition with powder X-ray diffraction.

2.8 Thermoelectric and heat-capacity measurements

The transport properties of Rb_8Sn_{44} were carried out on a Physical Property Measurement System (PPMS) from Quantum Design (Figure 2.2).[19] The as-synthesized bulk material was finely ground and compacted by spark plasma sintering (SPS) at a pressure of 100 MPa and a temperature of 550 K. The heating rate was approximately 50 K min^{-1} with a holding time of a few minutes. The electrical resistivity (ρ), thermal conductivity (κ) and thermopower (S) were measured simultaneously with a four-point setup using a quasi-static technique. Hall resistivities (ρ_H) were measured in magnetic fields of 0 - 9 T and temperatures of 10, 100, 200 and 300 K. Conducting silver paste was used for mounting the wires.

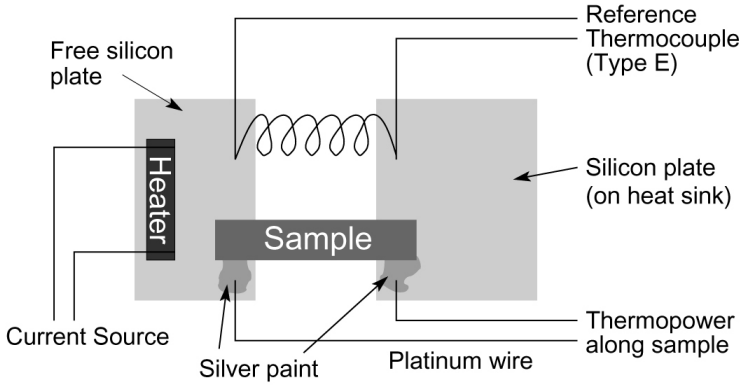

Figure 2.2 Schematic representation of the setup for thermopower measurements.

Electrical resistivity measurements were also performed on single crystals of Rb_8Sn_{44}, $Rb_{1.4}Cs_{6.6}Sn_{44}$ and Cs_8Sn_{44} with a standard four-probe dc method. A direct current of 0.1 mA was passed through the sample and a voltmeter was used to measure the voltage drop over the sample. The data were collected in the temperature range 250 - 400 K during cooling as well as heating runs with a temperature gradient of 0.7 K min^{-1}. Taking the uncertainty in the determination of the non-uniform sample shape into account, a relative error bar of 30% should be assumed for the residual resistivity.

The temperature-dependent heat capacity (C_P) of $Rb_{1.4}Cs_{6.6}Sn_{44}$ was investigated by means of a quasi-adiabatic step heating technique as implemented in the PPMS. The measurements were performed on a powdered sample (ca. 12 mg), which was pressed

into a pellet at 1.4 GPa. The pellet was thermally connected with the specific heat measuring device via Apiezon-N and Apiezon-H grease in the temperature ranges 1.8 - 300 K and 300 - 400 K, respectively. The uncertainty of the data points reported is estimated to be below 5%.

2.9 Neutron time-of-flight scattering

Neutron time-of-flight scattering is used in condensed matter physics to study phonon density of states, low-energy magnetic excitations and molecular diffusion processes. In principal, pulses of neutrons with adjustable velocity are scattered by the sample, then they travel through the flight chamber and finally reach the detectors. The velocity and angular difference between incident and scattered beam infers the inelastic interaction of the neutrons with the sample.

Time-of-flight experiments were performed at the Forschungsneutronenquelle Heinz Maier-Leibniz (FRM II). The TOFTOF instrument is fed with neutrons from the cold source of FRM II with a total flux of about 10^{10} neutrons cm^{-2} s^{-1}.[20] In the primary spectrometer, seven high-speed chopper discs made of carbon-fiber-reinforced plastic select short monochromatic neutrons pulses from the continuous white beam (Figure 2.3). The sample is located in the focus of a radial collimator, which oscillates continuously with ±2.2° amplitude. The detectors are adjusted tangentially to the intersection lines of the Debye-Scherrer cones with the surface of a virtual sphere around the center of the sample and cover the angular range from –15° to 140°. By recording the detection time of the neutrons, their time of flight from the sample to the detectors is measured and from that the neutron spectra are calculated. The instrument offers a good combination of neutron intensity, resolution and signal-to-background ratio.

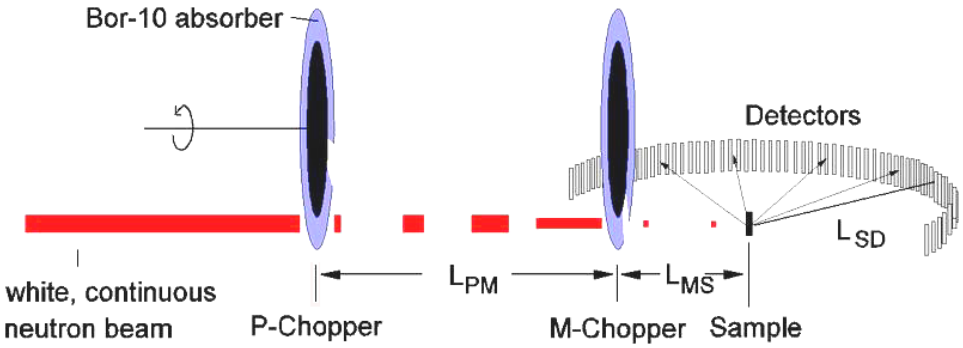

Figure 2.3 Schematic representation of the TOFTOF spectrometer.[21] The incident neutron wavelength can be selected from 1.4 - 12 Å and the rotation frequency of the discs from 10 - 367 s^{-1}. Other characteristics: L_{PM} = 10 m, L_{MS} = 1.4 m, L_{SD} = 4 m.

2.10 References

[1] W. Massa *Kristallstrukturbestimmung* 4. Auflage, Teubner Verlag, **2005**.

[2] X-Area 1.26, Stoe & Cie GmbH, **2004**.

[3] CrysAlis Red, Oxford Diffraction CCD Data Reduction, version 1.171.32.15, **2006**.

[4] X-SHAPE, Stoe & Cie GmbH: Crystal optimization program for numerical absorption correction, Darmstadt, **1997**.

[5] ABSPACK, Oxford Diffraction, **2005**.

[6] SHELXTL, version 5.1 UNIX, Bruker Analytical X-ray Systems, **1997**.

[7] Diamond, version 3.1f, K. Brandenburg, Crystal Impact GbR, Bonn, **2005**.

[8] Stoe WinxPow, version 2.08, Stoe & Cie GmbH, Darmstadt, **2003**.

[9] ICSD/Retrieve, version 1.4.1, FIZ Karlsruhe, **2005**.

[10] P. Villars, K. Cenzual *Pearson´s Crystal Data: Crystal Structure Database for Inorganic Compounds*, Version 1.0, ASM International Materials Park, USA, **2007/8**.

[11] T. Roisnel, J. Rodriguez-Carvajal *FULLPROF,* version 3.20, France, **2007**.

[12] E. Nishibori, M. Takata, K. Kato, M. Sakata, Y. Kubota, S. Aoyagi, Y. Kuroiwa, M. Yamakata, N. Ikeda *J. Phys. Chem. Solids* **2001**, *62*, 2095.

[13] Netzsch Proteus - Thermal Analysis Version 4.3.1, Germany, **2004**.

[14] T. B. Massalski, H. Okamoto, P. R. Subramanian, L. Kacprzak *Binary Alloy Phase Diagrams* 5th ed. ASM International Materials Park, USA, **2004**.

[15] E. Ruska *Rev. Mod. Phys.* **1987**, *59*, 627.

[16] P. A. Flinn *Mössbauer isomer shifts*, Eds. Amsterdam, North Holland, **1978**.

[17] N. B. Colthup, L. H. Daly, S. E. Wiberley *Introduction to Infrared and Raman Spectroscopy* (Third Edition) Academic Press, **1990**.

[18] P. W. Selwood *Magnetochemistry*, 2nd ed. Interscience, New York, **1956**.

[19] O. Maldonado *Cryogenics* **1992**, *32*, 908.

[20] T. Unruh, J. Neuhaus, W. Petry *Nuclear Instruments and Methods in Physics Research A* **2007**, *580*, 1414.

[21] www.frm2.tum.de/wissenschaft/spektrometer/toftof/prinzip-primaerspectrometer/index.html.

3. An order-disorder phase transition in type-I clathrates $Rb_xCs_{8-x}Sn_{44}$ ($0 \le x \le 8$)

3.1 Introduction

The structure of the type-I clathrates K_8Tt_{46} (Tt = Ge, Sn)[1] was first reported in 1969 in complete analogy to Na_8Si_{46}[2] and K_8Si_{46}.[1] The presence of framework defects in Ge and Sn clathrates was proposed later on, so that the compounds could be described as semiconducting and diamagnetic Zintl phases.[3,4] Indeed, several structural reinvestigations have proven the presence of two atomic vacancies (□) per unit cell for $K_8Ge_{44}\square_2$[5] and $A_8Sn_{44}\square_2$ (A = K,[6] Rb,[7,8] Cs[9,10]). The clathrates were found to crystallize in the cubic space group $Pm\bar{3}n$ and the partially occupied positions were distributed along a 4_2 screw axis (Figure 3.1). These framework sites are part of six-membered rings of the tkad and do not belong to the pdod.

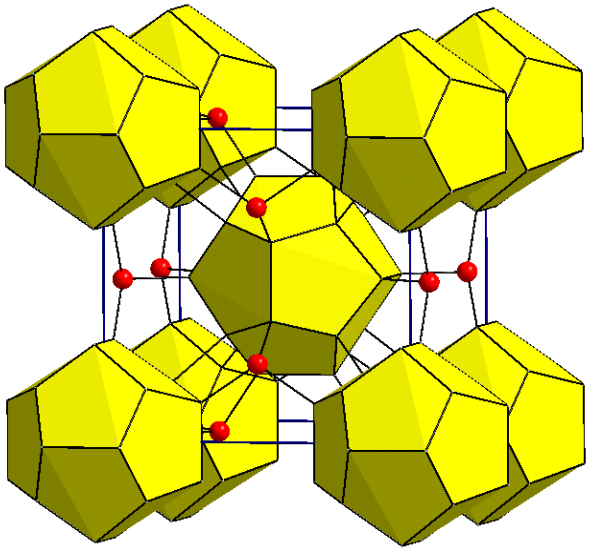

Figure 3.1 A view of the defect clathrate-I A_8Tt_{44} where the underoccupied sites (red atoms) interconnect the pdod (yellow polyhedra).

A Mulliken population analysis on the basis of topological charge stabilization showed that these framework sites (six out of 46) possess the lowest electron density and therefore it is easier to remove a Sn atom from there than from any other position.[11] More recent theoretical studies for Cs_8Sn_{44}[12] and K_8Sn_{44}[13] also indicated that one vacancy per six-membered ring is energetically favored over two vacancies per ring. This implies that the compound may exhibit an even higher ordering of the defects. Such a superstructure was experimentally established for Rb_8Sn_{44},[14] (see also Figure 3.5) which crystallizes with a $2 \times 2 \times 2$ unit cell in the space group $Ia\bar{3}d$ and the partially

occupied sites (three out of 46) are distributed along a 4_1 screw axis. However, the conditions under which the two modifications of Rb_8Sn_{44} ($Pm\bar{3}n$ and $Ia\bar{3}d$) occur or if they may co-exist still remained unclear.

3.2 Synthesis of $Rb_xCs_{8-x}Sn_{44}$ ($0 \le x \le 8$)

The compounds $Rb_xCs_{8-x}Sn_{44}$ were prepared by fusion of the elements in inert atmosphere. The substances were weighted in molar ratios Rb : Cs : Sn = 8 : 0 : 44, 6 : 2 : 44, 4 : 4 : 44, 2 : 6 : 44 and 0 : 8 : 44 (total mass 1 - 1.5 g) in Nb ampoules, which were sealed under reduced Ar pressure. The crucibles were subsequently enclosed in evacuated silica tubes (pressure ~3 10^{-2} mbar), heated for 12 hours to 1023 K, slowly cooled (0.1 K min^{-1}) to 773 K, held at this temperature for 10 days and then air-quenched to ambient temperature.

3.3 Crystal structure determination

3.3.1 Powder X-ray diffraction for A_8Sn_{44} (A = Rb, Cs)

The gray metal-like products were identified as type-I clathrates with a $2 \times 2 \times 2$ supercell, as already reported for Rb_8Sn_{44}.[14] Variation of the reactions conditions such as reaction temperatures between 973 K and 1223 K, annealing steps and cooling rates from 0.1 K min^{-1} to air-quenching did not significantly affect the product's composition, except for the quality and size of the crystals and the disappearance of *β*-Sn by increasing the annealing times. The compounds exhibit moderate air- and moisture-stability. The formation of SnO_2 on the surface of the crystallites was observed upon exposure to air for over one month. No other secondary phase was detected by powder diffractometry or scanning electron microscopy.

The structure of the products was verified by Rietveld analysis of the powder diffraction diagrams. In both cases, split models for the atomic positions adjacent to the partially occupied sites (see also Figure 3.7) were applied. The site occupation factors (SOFs) were set to the standard values for the composition A_8Sn_{44} without further refinement and the thermal displacement parameters of all atoms were refined isotropically.

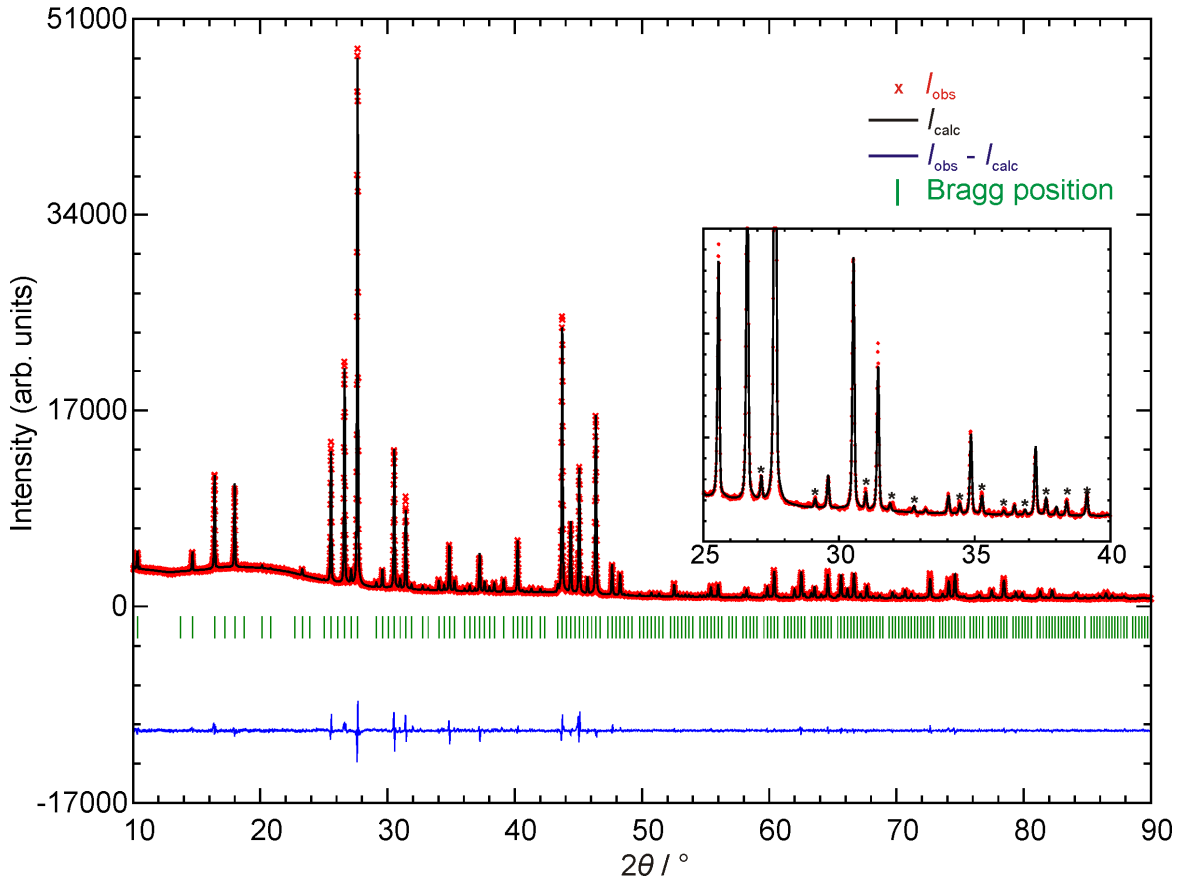

Figure 3.2 Rietveld refinement of the powder diffraction data for Rb_8Sn_{44} obtained at room temperature in transmission mode. The inset zooms in the area 25° ≤ 2θ ≤ 40°, where the superstructure reflections are denoted with black stars.

Table 3.1 Atomic coordinates and isotropic displacement parameters for Rb_8Sn_{44} (space group $Ia\bar{3}d$, a = 24.1194(3) Å, R_{Bragg} = 0.041, χ^2 = 4.31).

Atom	Site	*x*	*y*	*z*	SOF	U_{iso} / Å^2
Rb1	16*a*	0	0	0	1	0.0170(3)
Rb2	48*g*	0.125	0.2483(2)	0.0017(2)	1	0.0460(2)
Sn1	24*d*	0.375	0	0.25	1	0.0137(3)
Sn1´	24*c*	0.125	0	0.25	0.333	0.0203(1)
Sn2	32*e*	0.0908(1)	0.0908(1)	0.0908(1)	1	0.0146(3)
Sn2´	96*h*	0.0897(1)	0.4096(1)	0.0897(1)	1	0.0119(2)
Sn3a	96*h*	0.0027(1)	0.1514(1)	0.0581(1)	0.333	0.0167(7)
Sn3b	96*h*	0.0016(1)	0.1737(1)	0.0668(1)	0.667	0.0102(4)
Sn3´	96*h*	0.4997(1)	0.1538(1)	0.0557(1)	1	0.0091(2)

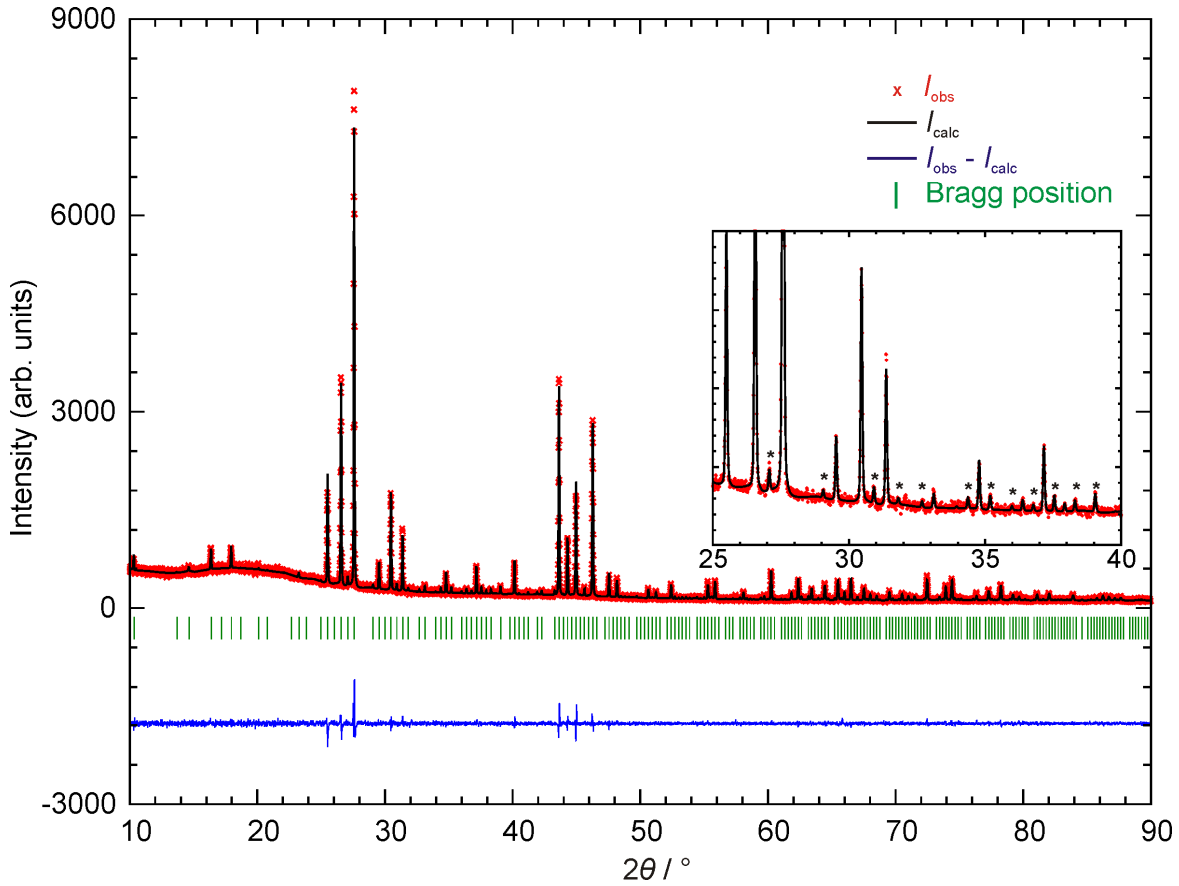

Figure 3.3 Rietveld refinement of the powder diffraction data for Cs_8Sn_{44} obtained at room temperature in transmission mode. The inset zooms in the area $25° \le 2\theta \le 40°$, where the superstructure reflections are denoted with black stars.

Table 3.2 Atomic coordinates and isotropic displacement parameters for Cs_8Sn_{44} (space group $Ia\bar{3}d$, a = 24.2341(3) Å, R_{Bragg} = 0.051, χ^2 = 1.36).

Atom	Site	*x*	*y*	*z*	SOF	U_{iso} / Å^2
Cs1	16*a*	0	0	0	1	0.0151(3)
Cs2	48*g*	0.125	0.2483(1)	0.00167(1)	1	0.0280(2)
Sn1	24*d*	0.375	0	0.25	1	0.0145(3)
Sn1´	24*c*	0.125	0	0.25	0.333	0.0127(2)
Sn2	32*e*	0.0915(1)	0.0915(1)	0.0915(1)	1	0.0143(3)
Sn2´	96*h*	0.0897(1)	0.4096(1)	0.0897(1)	1	0.0159(3)
Sn3a	96*h*	0.0029(1)	0.1514(1)	0.0599(1)	0.333	0.0097(4)
Sn3b	96*h*	0.0011(1)	0.1725(1)	0.0667(1)	0.667	0.0154(4)
Sn3´	96*h*	0.5010(1)	0.1533(1)	0.0559(1)	1	0.0101(3)

3.3.2 Single-crystal X-ray diffraction for Cs_8Sn_{44}

Good quality single crystals were obtained by annealing Cs_8Sn_{44} at 623 K for 10 days. One plate-like crystal was transferred into a glass capillary that was in turn mounted on the STOE IPDS-IIT diffractometer. The cell parameters were determined at 293 K, 313 K, 333 K, 353 K and 373 K, whereas the actual temperature of the crystal was additionally checked by an external thermocouple. Full data sets were collected at 373 K and then after cooling down to 293 K. Numerical absorption corrections were applied to the data after the integration.

At room temperature, Cs_8Sn_{44} crystallizes with cubic symmetry in a $2 \times 2 \times 2$ supercell of the type-I clathrate, exhibiting high ordering of the vacancies in the Sn framework. The crystal transformed reversibly and without change of the crystallinity over 353 K to the primitive cell with lower ordering of the defects (Figure 3.4). The low-temperature modification is named as *α*-Cs_8Sn_{44} and the high-temperature modification as *β*-Cs_8Sn_{44}. The parameters of the structure refinements are listed in Table 3.3.

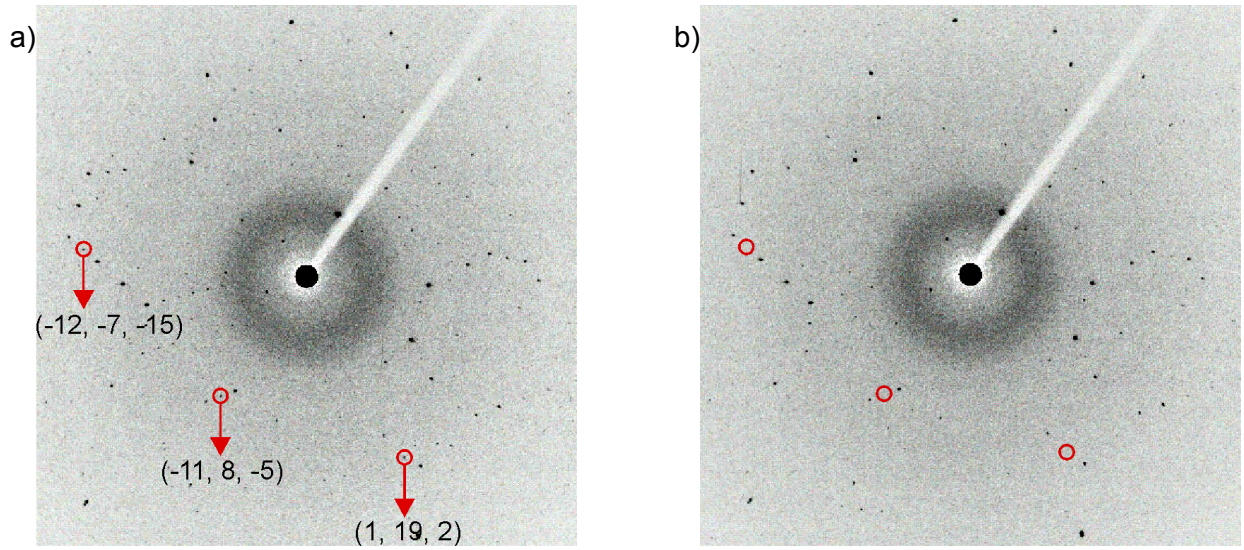

Figure 3.4 Selected frame from the single-crystal data collection for Cs_8Sn_{44} at 353 K (a) and 373 K (b) on an image plate detector where the superstructure reflections (some are marked with *h*, *k*, *l* indices) disappear due to the $Ia\bar{3}d \rightarrow Pm\bar{3}n$ transition.

Table 3.3 Crystal and structure refinement data for α-Cs_8Sn_{44} and β-Cs_8Sn_{44}.

Chemical formula	α-$Cs_8Sn_{44.02(1)}$	β-$Cs_8Sn_{44.12(3)}$
Space group (No.)	$Ia\bar{3}d$ (230)	$Pm\bar{3}n$ (223)
Formula weight	6287.53	6299.88
Temperature, T / K	293	373
Diffractometer	STOE IPDS-IIT	STOE IPDS-IIT
Radiation, λ / Å	Mo-Kα, 0.71073	Mo-Kα, 0.71073
Z	8	1
a / Å	24.256(3)	12.135(1)
V / Å^3	14272(3)	1787.1(4)
$\rho_{calc.}$ / g cm^{-3}	5.851	5.840
Absorption coeff., μ / mm^{-1}	19.10	19.06
F(000)	21120	2640
θ range for data collection / °	2.06 - 25.25	4.11 - 25.24
Index ranges	$0 \le h \le 16$, $0 \le k \le 20$, $2 \le l \le 29$	$0 \le h \le 8$, $0 \le k \le 10$, $2 \le l \le 14$
Reflections collected	85339	27209
Independent reflections	1083 (R_{int} = 0.085)	317 (R_{int} = 0.108)
Parameters	53	23
Goodness-of-fit on F^2	1.065	0.815
Weighting parameters	a = 0.0244, b = 0	a = 0.0232, b = 0
Final R indices (I > 2σ(I))	R_1 = 0.035, wR_2 = 0.054	R_1 = 0.020, wR_2 = 0.042
R indices (all data)	R_1 = 0.054, wR_2 = 0.058	R_1 = 0.035, wR_2 = 0.043
Largest diff. peak and hole / e Å^{-3}	0.77 in 2.29 Å from Cs2 –1.18 in 0.18 Å from Sn2'	0.68 in 1.46 Å from Sn3a –1.31 in 0.00 Å from Cs1

In α-Cs_8Sn_{44}, the partly occupied Sn1´ sites of the polyanionic framework are distributed around a 4_1 screw axis through the Cs atoms that reside in the tkad (Figure 3.5 and Table 3.4). As a consequence, a split model for the adjacent 96*h* site is adopted, giving rise to Sn3a atoms and Sn3b atoms that correspond to occupied and vacant Sn1´ sites, respectively (Figure 3.6). Also, the Sn2 atom has relatively large U_{iso} = 0.0263(3) Å^2 probably because three out of its four neighbors are the split Sn3a/Sn3b atoms (Table 3.5). Nevertheless, no split model could be applied for this position. Furthermore, two crystallographically non-equivalent positions for the Cs atoms are observed: a) Cs1 located in the dodecahedra and b) Cs2 located in the tetrakaidecahedra. In both cases the sites are fully occupied. The isotropic ADPs are 0.0193(3) Å^2 and 0.0378(2) Å^2 for Cs1 and Cs2 respectively, proving the stronger “rattling” of the guest in the larger cavities. It also worth’s mentioning that the Cs2 atoms reside not exactly in the center of

the cavities, but tend to the opposite site of the vacancy, namely closer to the Sn1 atom (24*d* Wyckoff position). This fact causes a slight deviation from linearity (178.88°) for the Cs2-Cs2-Cs2 chain parallel to the cubic axes and a displacement of the guest from the center of the cage by 0.0593 Å.

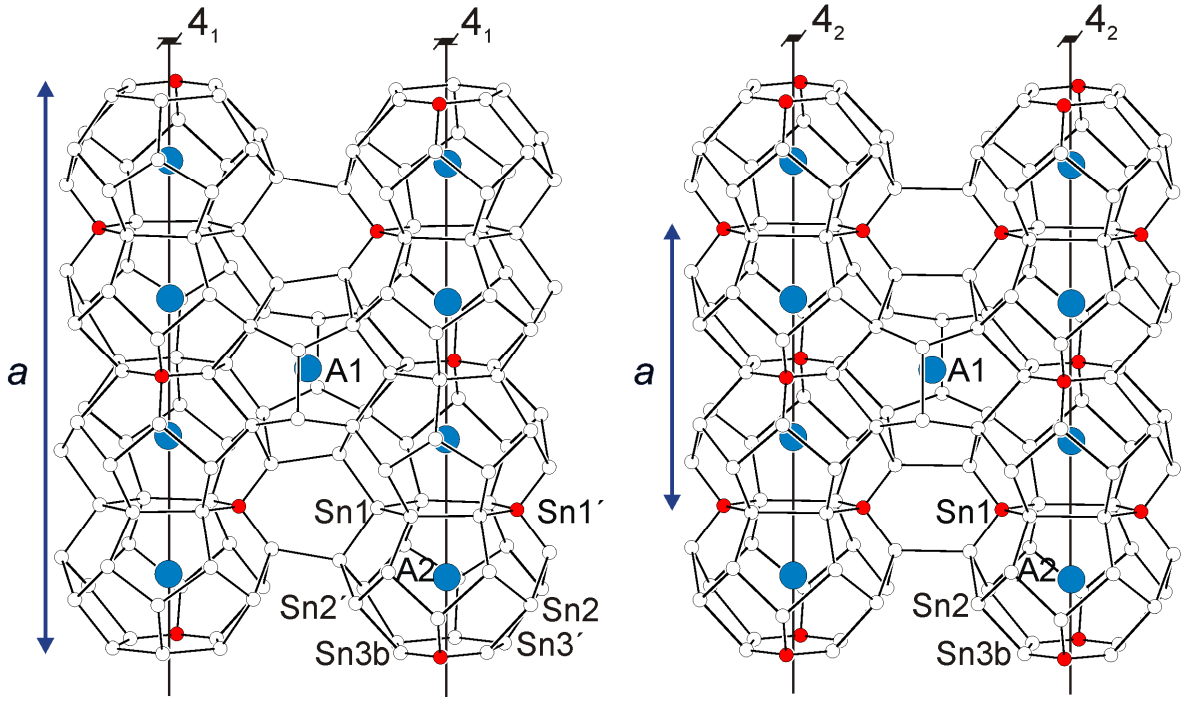

Figure 3.5 Partial view of the Cs_8Sn_{44} structures composed of two chains of tkad and one pdod. (a) In the *α* form, the partially occupied 24*c* sites (red Sn1´ atoms, SOF = 0.339) are distributed along a 4_1 helical axis. (b) In the *β* form, the partially occupied 6*c* sites (red Sn1 atoms, SOF = 0.687) are distributed along a 4_2 axis. In both cases, only the Sn atoms of the split positions with closer contacts to the vacancies are shown.

Table 3.4 Atomic coordinates and equivalent isotropic displacement parameters for *α*-Cs_8Sn_{44}.

Atom	Site	*x*	*y*	*z*	SOF	U_{eq} / Å^2
Cs1	16*a*	0	0	0	1	0.0193(3)
Cs2	48*g*	0.125	0.24827(3)	0.00173(3)	1	0.0378(2)
Sn1	24*d*	0.375	0	0.25	1	0.0145(3)
Sn1´	24*c*	0.125	0	0.25	0.339(6)	0.016(1)
Sn2	32*e*	0.09130(3)	0.09130(3)	0.09130(3)	1	0.0263(3)
Sn2´	96*h*	0.08969(3)	0.40950(3)	0.08969(3)	1	0.0179(2)
Sn3a	96*h*	0.0029(2)	0.1513(2)	0.0599(2)	0.339(6)	0.0167(7)
Sn3b	96*h*	0.0011(1)	0.1725(1)	0.06679(9)	0.661(6)	0.0185(4)
Sn3´	96*h*	0.50096(3)	0.15332(2)	0.05598(2)	1	0.0170(2)

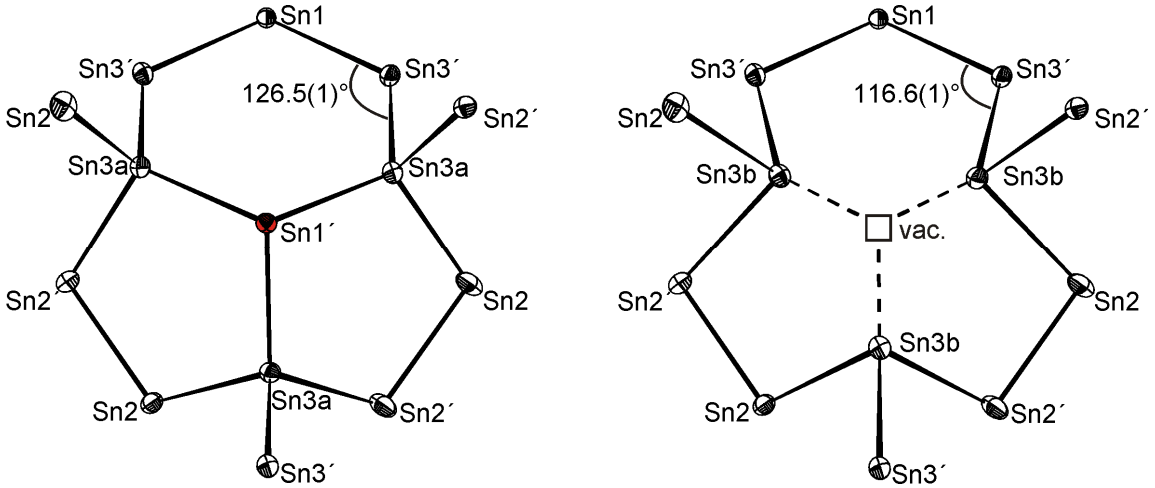

Figure 3.6 Split model applied for the Sn1´ site in α-Cs_8Sn_{44}. All ellipsoids are drawn at 50% probablity level.

Table 3.5 Anisotropic ADPs for α-Cs_8Sn_{44} (in Å^2).

Atom	U_{11}	U_{22}	U_{33}	U_{12}	U_{13}	U_{23}
Cs1	0.0193(3)	U_{11}	U_{11}	0.0003(3)	0.0003(3)	0.0003(3)
Cs2	0.0223(4)	0.0456(3)	U_{22}	0.0002(3)	0.0002(3)	–0.0029(5)
Sn1	0.0137(4)	0.0137(4)	0.0161(6)	0	0	0
Sn1´	0.016(1)	U_{11}	0.013(2)	0	0	0
Sn2	0.0263(3)	U_{11}	U_{11}	0.0064(3)	0.0064(3)	–0.0064(3)
Sn2´	0.0196(4)	0.0165(3)	0.0178(4)	0.0024(2)	–0.0037(3)	0.0004(2)
Sn3a	0.017(1)	0.015(2)	0.018(1)	0	0	0
Sn3b	0.0188(5)	0.0177(10)	0.0189(7)	0.0007(9)	0.0011(5)	0.0022(7)
Sn3´	0.0173(3)	0.0151(3)	0.0187(3)	0.0005(3)	0.0010(3)	0.0028(2)

In β-Cs_8Sn_{44}, the 6*c* Wyckoff site corresponds to the Sn1 atom with SOF = 0.687(7) (Table 3.6). Within the standard 3σ deviation this value is equivalent to the value of the *I*-centered crystals at room temperature and to 2/3, as anticipated for an electron-precise Zintl phase. The adjacent 24*k* site is better refined by means of a Sn3a/Sn3b split model with occupancies 0.687(7) and 0.313(7), respectively (Figure 3.7). Once again, the Cs atoms that reside in the large framework cavities exhibit much higher atomic displacement parameters than those in the smaller cavities (Table 3.7). The β modification exhibits overall larger ADPs than the α modification and the room-temperature data of an older refinement,[9] as expected from the temperature dependence in the Einstein's oscillator model (see also Chapter 4.2). On the other hand, the Sn-Sn-Sn angles have comparable values: 94.84(7)° - 126.52(9)° for the I-lattice and 94.68(1)° - 125.2(1)° for the primitive lattice.

Table 3.6 Atomic coordinates and equivalent isotropic displacement parameters for β-Cs_8Sn_{44}.

Atom	Site	*x*	*y*	*z*	SOF	U_{eq} / Å^2
Cs1	2*a*	0	0	0	1	0.0223(5)
Cs2	6*d*	0.25	0.5	0	1	0.0478(6)
Sn1	6*c*	0.25	0	0.5	0.687(7)	0.0197(9)
Sn2	16*i*	0.18314(4)	0.18314(4)	0.18314(4)	1	0.0259(3)
Sn3a	24*k*	0	0.3064(2)	0.1136(3)	0.687(7)	0.0233(5)
Sn3b	24*k*	0	0.3447(6)	0.1344(6)	0.313(7)	0.025(1)

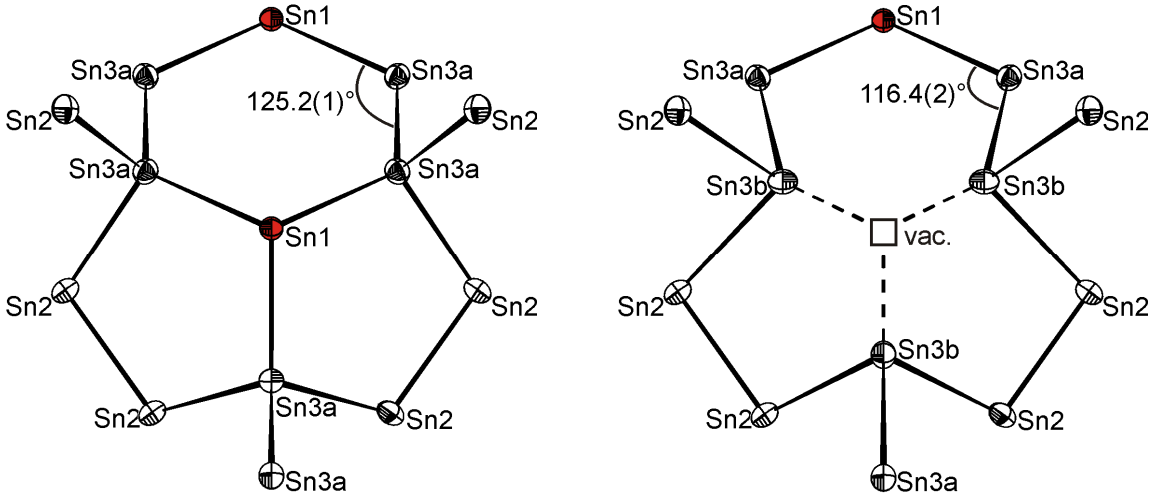

Figure 3.7 Split model applied for the Sn1 site in β-Cs_8Sn_{44}. All ellipsoids are drawn at 50% probablity level.

Table 3.7 Anisotropic ADPs for β-Cs_8Sn_{44} (in Å^2).

Atom	U_{11}	U_{22}	U_{33}	U_{12}	U_{13}	U_{23}
Cs1	0.0223(5)	U_{11}	U_{11}	0	0	0
Cs2	0.0278(9)	0.0577(8)	U_{22}	0	0	0
Sn1	0.020(1)	0.0197(9)	U_{22}	0	0	0
Sn2	0.0259(3)	U_{11}	U_{11}	–0.0045(2)	U_{12}	U_{12}
Sn3a	0.0227(7)	0.022(1)	0.025(1)	0	0	–0.0031(9)
Sn3b	0.0222(16)	0.032(4)	0.021(3)	0	0	0

The symmetry relationship between the two modifications is described as a “klassengleiche” transition of index 4 (Table 3.8). The unit cell parameters are doubled as the primitive cell transforms to the bcc cell. The latter possesses lower symmetry as indicated by the splitting of certain framework positions.

Table 3.8 Group-subgroup relationship between the *β*- and *α*-modification of Cs_8Sn_{44}.

	2Cs1 2*a*	6Cs2 6*d*	4Sn1 6*c*	16Sn2 16*i*	16Sn3a 24*k*	8Sn3b 24*k*
$Pm\bar{3}n$	0 0 0	0.25 0.5 0	0.25 0 0.5	0.18314 0.18314 0.18314	0 0.3064 0.1136	0 0.3447 0.1344
*k*4 2 × 2 × 2						

	2Cs1 16*a*	6Cs2 48*g*	24Sn1 24*d*	8Sn1´ 24*c*	32Sn2 32*e*	96Sn2´ 96*h*	32Sn3a 96*h*	64Sn3b 96*h*	96Sn3´ 96*h*
$Ia\bar{3}d$	0 0 0	0.125 0.2483 0.0017	0.375 0 0.25	0.125 0 0.25	0.0913 0.0913 0.0913	0.0897 0.4095 0.0897	0.0029 0.1513 0.0599	0.0011 0.1725 0.0668	0.5009 0.1533 0.0559

Focusing now on the ordering of the vacancies, each (almost planar) hexagon in *α*-$Cs_8Sn_{44}\square_2$ may either be defect free or possess one defect with a relaxation of the neighboring atoms that drift towards the vacancy (Figure 3.8 and Table 3.9). In *β*-Cs_8Sn_{44}, except for the above configurations with similar structures, a third configuration with two defects per hexagons in *para*-position may also occur (Figure 3.9). Consequently, the bonds between the remaining four atoms are even more elongated (3.26(2) Å), that is about 0.3 Å longer than typical distances between 3b-Sn^- atoms, like the tetrahedral $[Sn_4]^{4-}$ clusters in Cs_4Sn_4 with *d*(Sn-Sn) = 2.939(2) Å.[15]

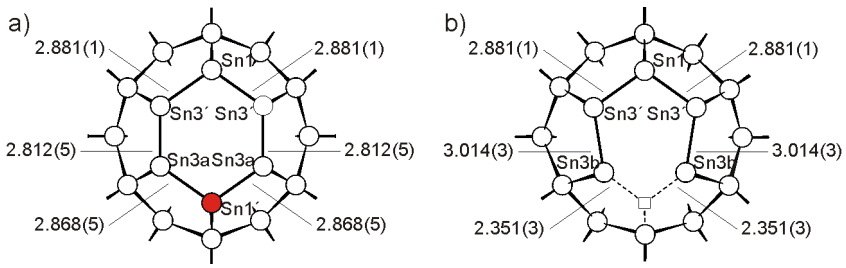

Figure 3.8 Perpendicular view of a hexagon in *α*-Cs_8Sn_{44}: a) no defects and b) one defect. All distances are given in Å.

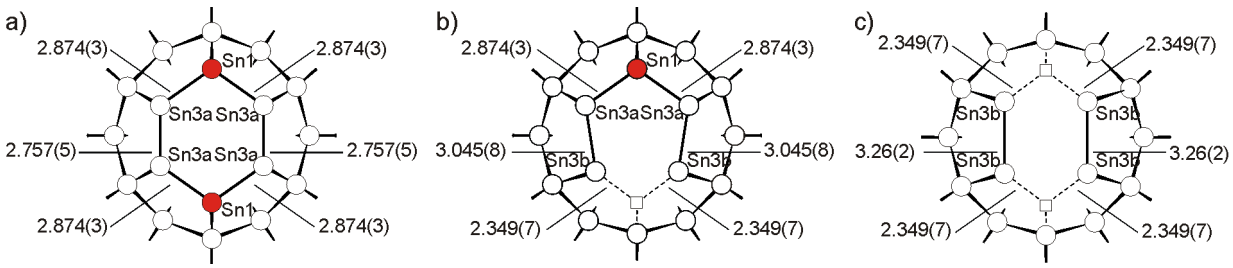

Figure 3.9 Perpendicular view of a hexagon in *β*-Cs_8Sn_{44}: a) no defects b) one defect c) two defects. All distances are given in Å.

Table 3.9 Interatomic distances for *α*- and *β*-Cs_8Sn_{44}.

α-Cs_8Sn_{44}		*β*-Cs_8Sn_{44}	
Atomic pairs	*d* / Å	Atomic pairs	*d* / Å
Sn1 -Sn3′	2.881(1) 4×	Sn1 -Sn3a	2.874(3) 4×
Sn1′ -Sn3a	2.868(5) 4×	-Sn3b	2.349(7) 4×
-Sn3b	2.350(2) 4×		
Sn2 -Sn2	2.832(1)	Sn2 -Sn2	2.8107(7)
-Sn3a	2.700(4) 3×	-Sn3a	2.809(3) 3×
-Sn3b	3.003(3) 3×	-Sn3b	3.022(5) 3×
Sn2′ -Sn2′	2.809(1)		
-Sn3a	2.737(4)		
-Sn3b	2.959(2)		
-Sn3′	2.854(1)		
-Sn3′	2.8600(9)		
Sn3a -Sn3′	2.812(5)	Sn3a -Sn3a	2.757(5)
Sn3b -Sn3′	3.014(3)	-Sn3b	3.045(8)
		Sn3b -Sn3b	3.26(2)
Cs1 -Sn2	3.8358(8) 2×	Cs1 -Sn2	3.8494(5) 8×
-Sn2′	3.8487(8) 6×		
-Sn3a	3.948(5) 6×	-Sn3a	3.965(3) 12×
-Sn3b	4.488(2) 6×	-Sn3b	4.489(7) 12×
-Sn3′	3.9591(7) 6×		
Cs2 -Sn1	4.2585(6) 2×	Cs2 -Sn1	4.2905(3) 4×
-Sn1′	4.3179(6) 2×		
-Sn2	4.572(1) 2×	-Sn2	4.5148(6) 8×
-Sn2′	4.432(1) 2×		
-Sn2′	4.516(1) 2×		
-Sn2′	4.535(1) 2×		
-Sn3a	4.116(4) 2×	-Sn3a	4.077(2) 8×
-Sn3b	3.935(2) 2×	-Sn3b	3.926(5) 8×
-Sn3a	4.171(4) 2×	-Sn3a	4.739(2) 4×
-Sn3b	3.936(2) 2×	-Sn3b	4.583(7) 4×
-Sn3a	4.697(5) 2×		
-Sn3b	4.632(2) 2×		
-Sn3′	4.0461(9) 2×		
-Sn3′	4.0598(9) 2×		
-Sn3′	4.714(1) 2×		

3.3.3 Synchrotron resonance powder X-ray diffraction for A_8Sn_{44} (A = Rb, Cs)

The order-disorder phase transition in A_8Sn_{44} (A = Rb, Cs) was further investigated with synchrotron diffraction methods at various temperatures. The experiments were performed using the following setups:

1. For Rb_8Sn_{44} in the temperature range 90 - 300 K with λ = 0.481566 Å and steps of 15 K.
2. For Rb_8Sn_{44} and Cs_8Sn_{44} in the temperature range 300 - 510 K with λ = 0.432650 Å and steps of 35 K.
3. For Rb_8Sn_{44} in the temperature range 303 - 673 K with λ = 0.499658 Å and steps of 10 K and 20 K, including one measurement at 303 K after cooling down the sample.

For setups 1 and 2, the powder diagrams were refined with the Rietveld method and the detailed tables are given in Appendix B. The measurements at 90 - 300 K showed pure phase of the Rb_8Sn_{44} superstructure (Figure 3.10). No structural changes occurred apart from the normal isotropic expansion of the unit cell edges and the increase of the ADPs with increasing temperature, as will be discussed in Chapter 4.2.

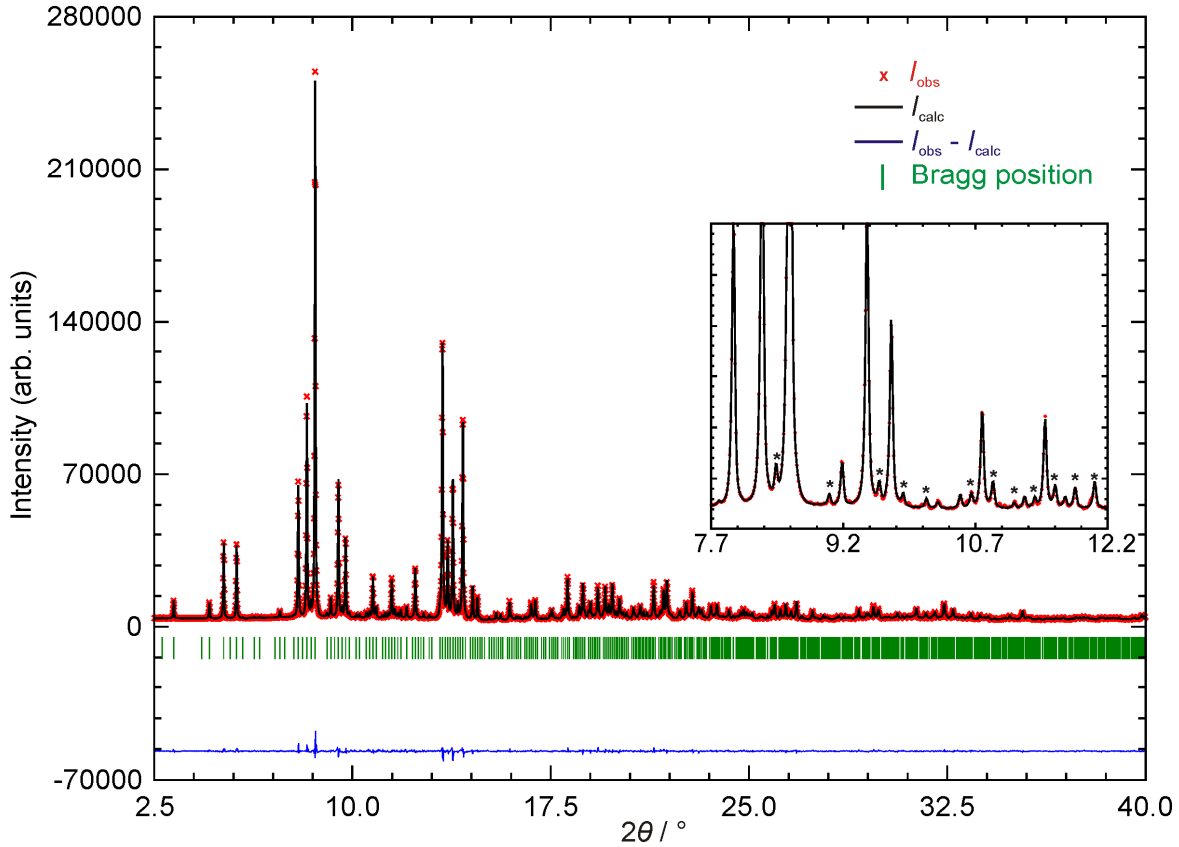

Figure 3.10 Rietveld refinement of the synchrotron diffraction data for α-Rb_8Sn_{44} obtained at 90 K in Debye-Scherrer mode. The inset zooms in the area 7.7° ≤ 2θ ≤ 12.2°, where the superstructure reflections are denoted with black stars.

In setup 2, the samples contained small amounts of *β*-Sn (2.5(1)% and 0.7(1)% scaled for Rb_8Sn_{44} and Cs_8Sn_{44}, respectively). The temperature dependence of the unit-cell parameters from the data collections below and above 300 K is shown in Figure 3.11. For both samples the parameters smoothly increase as a function of temperature and the value of Cs_8Sn_{44} is on average 0.053(1) Å larger than that of Rb_8Sn_{44}. The difference is considerably less than the difference in ionic radii 1.52 Å and 1.67 Å of Rb^+ and Cs^+, respectively.

The phase transformation takes place for both clathrates between 335 and 370 K. Above 370 K, Rb_8Sn_{44} gradually decomposes into *β*-Sn and another phase in small amount that remains unindexed. A similar decomposition of Ba_8Ge_{43} into *α*-Ge and Ba_6Ge_{25} over 700 K has been recently reported.[16] At 510 K, Rb_8Sn_{44} is almost fully decomposed and this diffraction pattern will not be used in the discussion for the ADPs. Cs_8Sn_{44} decomposes above 440 K, again the decomposition is detected as an increase in the intensity of the *β*-Sn reflections. Unlike the order-disorder transition, the decomposition reactions are not reversed by cooling the samples.

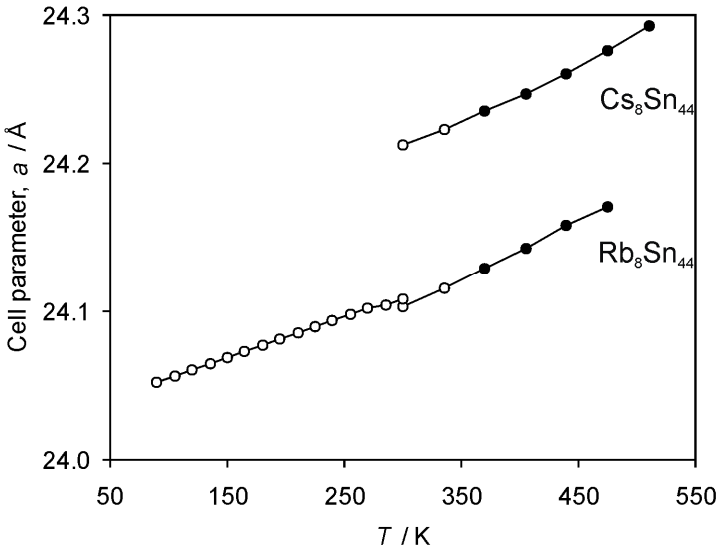

Figure 3.11 Unit-cell parameters of Rb_8Sn_{44} and Cs_8Sn_{44} as a function of temperature. The closed circles refer to the double of the unit-cell size of the *β*-modification.

The phase transition and the decomposition reaction in Rb_8Sn_{44} are explicitly shown in the powder patterns obtained with setup 3 (Figure 3.12). The superstructure reflections disappear over 353 K, however no noticeable change of the intensity or shape of the remaining peaks occurs. A weak peak of *β*-Sn is observed at temperatures over 373 K. By cooling the sample to room temperature, the superstructure reflections appear again. According to the subsequent Rietveld analysis, the residue contains about

15% *β*-Sn per weight.

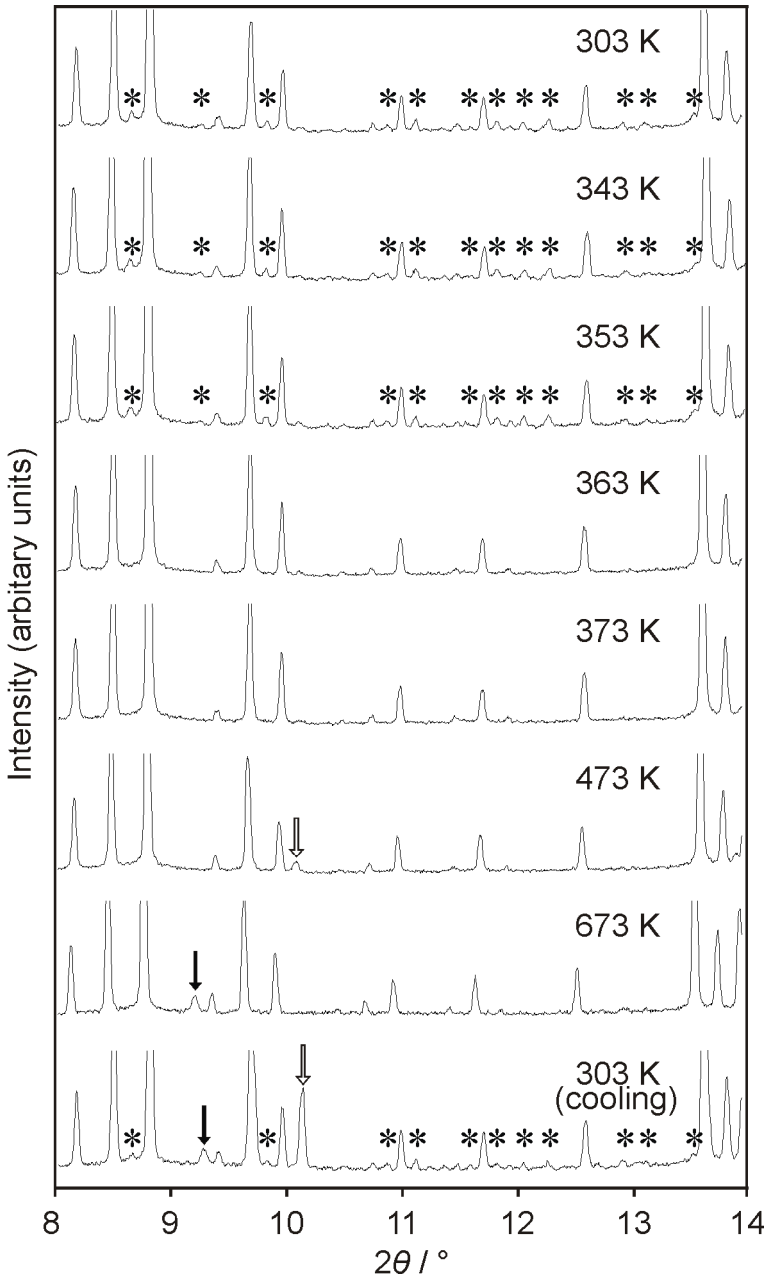

Figure 3.12 Parts of the synchrotron powder diagrams for Rb_8Sn_{44}. Superstructure reflections, unindexed peaks and *β*-Sn are denoted with black stars, black arrows and white arrows, respectively.

3.3.4 Powder X-ray diffraction for $Rb_xCs_{8-x}Sn_{44}$ (x = 2.1, 1.4, 1.3)

The main products of the reaction stoichiometries Rb : Cs : Sn = 2 : 6 : 44, 4 : 4 : 44 and 6 : 2 : 44 were gray, metal-like crystals with the type-I clathrate structure. The powder patterns were indexed in the same 2 × 2 × 2 supercell as for the binary compounds A_8Sn_{44} (A = Rb, Cs). In all cases, the presence of Rb, Cs and Sn was confirmed by EDX analysis on the clathrates. However, the samples were not phase pure and contained also *β*-Sn and at least one binary Rb-Sn compound that remains unidentified. Upon exposure to O_2 or H_2O, this secondary phase decomposed into *β*-Sn and alkali-metal oxides. The concentration of admixtures in the reaction products is more pronounced for the molar ratios Rb : Cs : Sn = 4 : 4 : 44 and 6 : 2 : 44. Only the reaction stoichiometry 2 : 6 : 44 resulted in an almost pure-phase product. According to the corresponding Rietveld analysis (Figure 3.13 and Table 3.10), the composition of this clathrate is $Rb_{0.98(3)}Cs_{7.02(3)}Sn_{44}$.

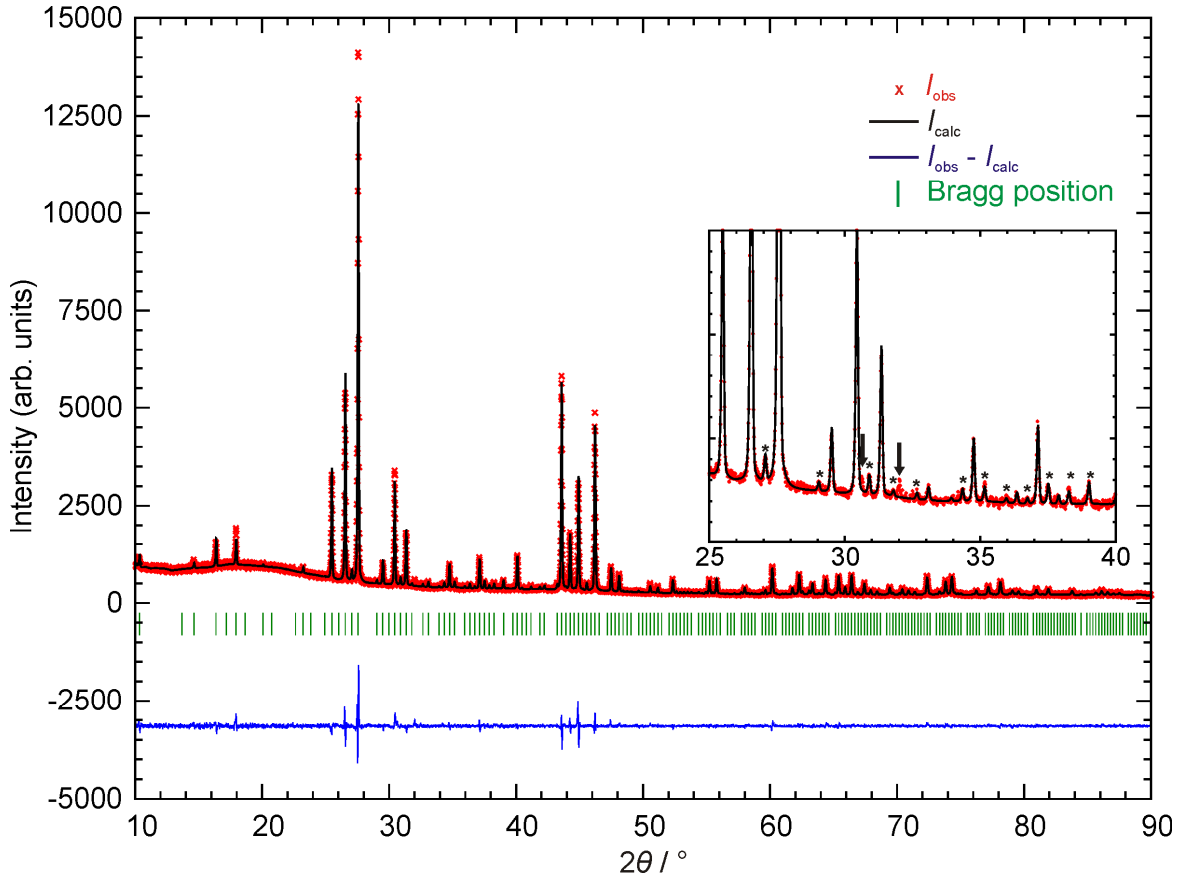

Figure 3.13 Rietveld refinement of the powder diffraction data for *α*-$Rb_{0.98(3)}Cs_{7.02(3)}Sn_{44}$ obtained at room temperature in transmission mode. The inset zooms in the area 25° ≤ 2*θ* ≤ 40°, where the superstructure reflections and the traces of *β*-Sn are denoted with black stars and black arrows, respectively.

Table 3.10 Atomic coordinates and isotropic displacement parameters for $Rb_{0.98(3)}Cs_{7.02(3)}Sn_{44}$ (space group $Ia\bar{3}d$, a = 24.1971(4) Å, R_{Bragg} = 0.047, χ^2 = 1.98).

Atom	Site	*x*	*y*	*z*	SOF	U_{iso} / Å^2
Rb/Cs1	16*a*	0	0	0	0.09/0.91(2)	0.0172(3)
Rb/Cs2	48*g*	0.125	0.2487(1)	0.0017(1)	0.18/0.82(3)	0.0355(3)
Sn1	24*d*	0.375	0	0.25	1	0.01
Sn1´	24*c*	0.125	0	0.25	0.333	0.01
Sn2	32*e*	0.0917(1)	0.0917(1)	0.0917(1)	1	0.01
Sn2´	96*h*	0.0888(1)	0.4088(1)	0.0888(1)	1	0.01
Sn3a	96*h*	0.0029(1)	0.1514(1)	0.0599(1)	0.333	0.01
Sn3b	96*h*	0.0012(1)	0.1743(1)	0.0671(1)	0.667	0.01
Sn3´	96*h*	0.5010(1)	0.1533(1)	0.0559(1)	1	0.01

3.3.5 Single-crystal X-ray diffraction for $Rb_xCs_{8-x}Sn_{44}$ (x = 2.1, 1.4, 1.3)

The composition of the ternary clathrates was refined with higher accuracy from the single-crystal data. The same single crystals were also checked with the EDX method (Table 3.11). More specifically, $Rb_{2.12}Cs_{5.88}Sn_{44}$ and $Rb_{1.42}Cs_{6.58}Sn_{44}$ were obtained from the loading mixtures Rb : Cs : Sn = 6 : 2 : 44 and 2 : 6 : 44, respectively. Annealing of the reaction product from the latter stoichiometry for 40 days at 723 K gave rise to $Rb_{1.32}Cs_{6.68}Sn_{44}$ (Table 3.12).

Table 3.11 Composition of the ternary clathrates $Rb_xCs_{8-x}Sn_{44}$ determined by single-crystal and powder X-ray diffraction as well as EDX analysis.

Reaction stoichiometry (x)	Single-crystal analysis (x)	Rietveld analysis (x)	EDX analysis (Rb : Cs : Sn)
2	1.42(8)	0.98(3)	5(1) : 5(1) : 44(2)
2 (annealed)	1.32(8)	1.36(6)	5(1) : 1.5(5) : 44(3)
4	—	3.1(2)	—
6	2.1(1)	—	3.5(1) : 1.9(5) : 44(2)

Obviously, the composition of the clathrates depends only slightly on the reaction's stoichiometry. According to the single-crystal analysis for x = 1.4, 1.3 and 2.1, mixed occupancy for Rb and Cs is observed in the cationic sites 16*a* and 48*g* (Table 3.13, Figure 3.14). No underoccupancy was found on these sites upon free refinement of the SOFs. However, the corresponding occupation factors are unavoidably correlated to the thermal displacements of the atoms, implying that the actual deviation is larger than the estimated value by the least-square refinement.

Table 3.12 Crystallographic data and refinement parameters for $Rb_xCs_{8-x}Sn_{44}$ (x = 2.1, 1.4, 1.3).

Chemical formula	$Rb_{2.1(1)}Cs_{5.9(1)}Sn_{44}$	$Rb_{1.42(8)}Cs_{6.58(8)}Sn_{44}$	$Rb_{1.32(8)}Cs_{6.68(8)}Sn_{44}$
Space group (No.)	$Ia\bar{3}d$ (230)	$Ia\bar{3}d$ (230)	$Ia\bar{3}d$ (230)
Formula weight	6183.79	6218.22	6223.20
Temperature, T / K	293	293	293
Diffractometer	Oxford Xcalibur3	Oxford Xcalibur3	Oxford Xcalibur3
Radiation, λ / Å	Mo-Kα, 0.71073	Mo-Kα, 0.71073	Mo-Kα, 0.71073
Z	8	8	8
a / Å	24.1764(1)	24.197(1)	24.2015(2)
V / Å^3	14131.1(1)	14167(1)	14175.1(2)
$\rho_{calc.}$ / g cm^{-3}	5.815	5.831	5.832
Absor. coeff., μ / mm^{-1}	19.66	19.49	19.46
F(000)	20815	20915	20930
θ range for data collection / °	3.15 - 25.31	3.77 - 25.32	3.15 - 25.28
Index ranges	$-24 \le h \le 29$, $-25 \le k \le 29$, $-28 \le l \le 29$	$-29 \le h \le 27$, $-29 \le k \le 22$, $-28 \le l \le 29$	$-28 \le h \le 29$, $-22 \le k \le 29$, $-28 \le l \le 28$
Reflections collected	43741	42009	41731
Indep. reflections	1082 (R_{int} = 0.054)	1085 (R_{int} = 0.076)	1080 (R_{int} = 0.072)
Parameters	55	55	55
Goodness-of-fit on F^2	1.136	1.021	1.116
Weighting parameters	a = 0.0223, b = 1089	a = 0.0525, b = 0	a = 0.0263, b = 425.4
Final R indices (I > 2σ(I))	R_1 = 0.037, wR_2 = 0.078	R_1 = 0.032, wR_2 = 0.087	R_1 = 0.030, wR_2 = 0.071
R indices (all data)	R_1 = 0.049, wR_2 = 0.086	R_1 = 0.046, wR_2 = 0.091	R_1 = 0.043, wR_2 = 0.077
Largest diff. peak and hole / e Å^{-3}	0.9 in 2.2 Å from Cs2 –0.9 in 2.2 Å from Sn3b	1.0 in 1.4 Å from Sn3´ –1.1 in 0.6 Å from Sn2´	0.7 in 0.8 Å from Sn2´ –0.9 in 0.0 Å from Cs1

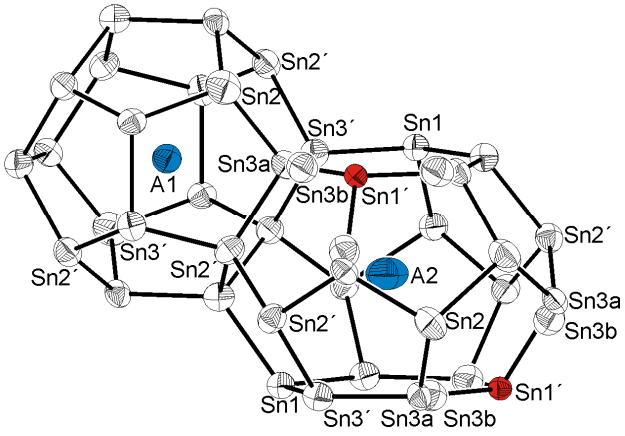

Figure 3.14 Partial view of the $Rb_{1.42}Cs_{6.58}Sn_{44}$ crystal structure. Displacement ellipsoids are drawn at 90% probability level. A1: Rb (46%), Cs (54%) and A2: Rb (8%), Cs (92%).

The Cs atoms occupy preferably the centres of tkad rather than the pdod. $Rb_{1.42}Cs_{6.58}Sn_{44}$ and $Rb_{1.32}Cs_{6.68}Sn_{44}$ differ only in the occupation factors of the alkali metals in the pdod. Furthermore, the unit cell expands to some extent as the Cs content of the clathrates increases. The anisotropic displacement parameters of all refined crystal structures showed also the rattling of the alkali metals in the centre of the tkad (Table 3.14).

Table 3.13 Atomic coordinates and equivalent isotropic displacement parameters for $Rb_xCs_{8-x}Sn_{44}$ (x = 2.1, 1.4, 1.3) (in Å^2).

Atom	Site	*x*	*y*	*z*	SOF	U_{eq} / Å^2
			$Rb_{2.12}Cs_{5.88}Sn_{44}$			
Rb/Cs1	16*a*	0	0	0	0.60/0.40(2)	0.0210(8)
Rb/Cs2	48*g*	0.125	0.24837(4)	0.00173(4)	0.15/0.85(2)	0.0406(5)
Sn1	24*d*	0.375	0	0.25	1	0.0187(4)
Sn1′	24*c*	0.125	0	0.25	0.333	0.0111(8)
Sn2	32*e*	0.09124(3)	0.09124(3)	0.09124(3)	1	0.0287(4)
Sn2′	96*h*	0.09429(3)	0.40942(3)	0.08968(3)	1	0.0201(2)
Sn3a	96*h*	0.0030(1)	0.1516(2)	0.0597(2)	0.333	0.0152(8)
Sn3b	96*h*	0.0009(1)	0.1729(1)	0.0669(1)	0.667	0.0248(5)
Sn3′	96*h*	0.50086(3)	0.15342(3)	0.05590(3)	1	0.0215(2)
			$Rb_{1.42}Cs_{6.58}Sn_{44}$			
Rb/Cs1	16*a*	0	0	0	0.46/0.54(2)	0.0239(7)
Rb/Cs2	48*g*	0.125	0.24833(3)	0.00167(3)	0.08/0.92(1)	0.0449(5)
Sn1	24*d*	0.375	0	0.25	1	0.0240(2)
Sn1′	24*c*	0.125	0	0.25	0.333	0.0233(2)
Sn2	32*e*	0.09127(3)	0.09127(3)	0.09127(3)	1	0.0318(4)
Sn2′	96*h*	0.09436(3)	0.40945(3)	0.08967(3)	1	0.0203(8)
Sn3a	96*h*	0.0028(2)	0.1516(2)	0.0597(2)	0.333	0.0273(4)
Sn3b	96*h*	0.0011(1)	0.1728(1)	0.0670(1)	0.667	0.0206(3)
Sn3′	96*h*	0.50089(3)	0.15334(3)	0.05595(3)	1	0.0156(7)
			$Rb_{1.32}Cs_{6.68}Sn_{44}$			
Rb/Cs1	16*a*	0	0	0	0.40/0.60(2)	0.0219(6)
Rb/Cs2	48*g*	0.125	0.24830(4)	0.00170(4)	0.08/0.92(1)	0.0409(5)
Sn1	24*d*	0.375	0	0.25	1	0.0219(2)
Sn1′	24*c*	0.125	0	0.25	0.333	0.0209(2)
Sn2	32*e*	0.09128(3)	0.09128(3)	0.09128(3)	1	0.0296(3)
Sn2′	96*h*	0.09430(3)	0.40944(3)	0.08974(3)	1	0.0153(7)
Sn3a	96*h*	0.0028(2)	0.1518(2)	0.0598(2)	0.333	0.0253(4)
Sn3b	96*h*	0.0010(1)	0.1728(1)	0.0670(1)	0.667	0.0189(3)
Sn3′	96*h*	0.50083(3)	0.15340(3)	0.05596(3)	1	0.0126(7)

Table 3.14 Anisotropic displacement parameters for $Rb_xCs_{8-x}Sn_{44}$ (x = 2.1, 1.4, 1.3) (in $Å^2$).

Atom	U_{11}	U_{22}	U_{33}	U_{12}	U_{13}	U_{23}
			$Rb_{2.12}Cs_{5.88}Sn_{44}$			
Rb/Cs1	0.0210(8)	U_{11}	U_{11}	0	0	0
Rb/Cs2	0.0256(7)	0.0482(7)	U_{22}	0	0	–0.0024(6)
Sn1	0.0182(5)	0.0182(5)	0.0198(8)	0	0	0
Sn1′	0.010(1)	0.010(1)	0.013(2)	0.002(2)	0	0
Sn2	0.0287(4)	U_{11}	U_{11}	0.0062(3)	0.0062(3)	–0.0062(3)
Sn2′	0.0219(4)	0.0185(4)	0.0200(4)	0.0023(3)	–0.0039(3)	–0.0004(3)
Sn3a	0.016(1)	0.016(2)	0.014(1)	0	–0.003(1)	0
Sn3b	0.0229(8)	0.026(1)	0.025(1)	0	0.0014(7)	0.004(1)
Sn3′	0.0192(4)	0.0211(4)	0.0243(4)	0	0.0009(3)	0
			$Rb_{1.42}Cs_{6.58}Sn_{44}$			
Rb/Cs1	0.0239(7)	U_{11}	U_{11}	0	0	0
Rb/Cs2	0.0286(7)	0.0530(6)	U_{22}	0	0	–0.0032(5)
Sn1	0.0198(4)	0.0198(4)	0.0222(7)	0	0	0
Sn1′	0.015(1)	0.015(1)	0.015(1)	0.001(1)	0	0
Sn2	0.0318(4)	U_{11}	U_{11}	0.0059(3)	0.0059(3)	–0.0059(3)
Sn2′	0.0247(4)	0.0215(4)	0.0236(4)	0.0022(3)	–0.0036(3)	0
Sn3a	0.022(1)	0.021(2)	0.018(1)	0.003(2)	0.001(1)	–0.004(2)
Sn3b	0.0260(7)	0.028(1)	0.0278(9)	0.001(1)	0.0013(6)	0.0025(9)
Sn3′	0.0227(4)	0.0227(4)	0.0267(4)	0	0.0011(3)	0
			$Rb_{1.32}Cs_{6.68}Sn_{44}$			
Rb/Cs1	0.0219(6)	U_{11}	U_{11}	0	0	0
Rb/Cs2	0.0258(6)	0.0484(6)	U_{22}	0	0	0
Sn1	0.0184(4)	0.0184(4)	0.0199(7)	0	0	0
Sn1′	0.012(1)	0.012(1)	0.014(2)	0.002(1)	0	0
Sn2	0.0296(3)	U_{11}	U_{11}	0.0059(3)	0.0059(3)	–0.0059(3)
Sn2′	0.0229(4)	0.0190(4)	0.0207(4)	0.0024(3)	–0.0037(3)	0
Sn3a	0.017(1)	0.016(2)	0.013(1)	0	0	0
Sn3b	0.0234(7)	0.026(1)	0.0263(9)	0	0.0009(6)	0.0029(9)
Sn3′	0.0205(4)	0.0213(4)	0.0240(4)	0	0.0008(3)	0.0007(3)

Multi-temperature diffraction experiments were performed on the single crystal of $Rb_{1.42}Cs_{6.58}Sn_{44}$. At 173 K the reflections were consistent with the space group $Ia\bar{3}d$. The crystal was then heated to 373 K in steps of 10 K. The intensity of the supercell reflections decreased gradually as the temperature exceeded 333 K. At 373 K the crystal was completely transformed to primitive (Appendix C). The inverse phenomenon was observed by cooling, whereas the crystal was perfectly preserved. Note that small deviations in the unit-cell size are attributed to the settings of different X-ray detectors.

3.4 Thermal analysis

The order-disorder transformation in A_8Sn_{44} (A = Rb, Cs) is also detectable by differential thermal analysis (DTA). At about 355 K and 368 K a weak endothermic peak is observed for Rb_8Sn_{44} and Cs_8Sn_{44} (Figure 3.15), respectively and is attributed to the $Ia\bar{3}d \rightarrow Pm\bar{3}n$ transition. The reverse phenomenon takes place as an exothermic peak during cooling. The hysteresis of the peaks depends significantly on the heating and cooling rates. On average of the experimental maxima, one can define the transition temperature at T_t = 353 K for Rb_8Sn_{44} and T_t = 363 K for Cs_8Sn_{44}. The latent heat of the transformation in Cs_8Sn_{44} was found to be ΔH_t = –0.38 J g^{-1}, which is very low compared to other first-order transitions, like α-Sn → β-Sn at 286.2 K with ΔH_t = –17.6 J g^{-1} or –2089 J mol^{-1}.[17] The XRPD diagrams and the SEM studies on the residues of the thermal analysis did not show traces of β-Sn or other phases.

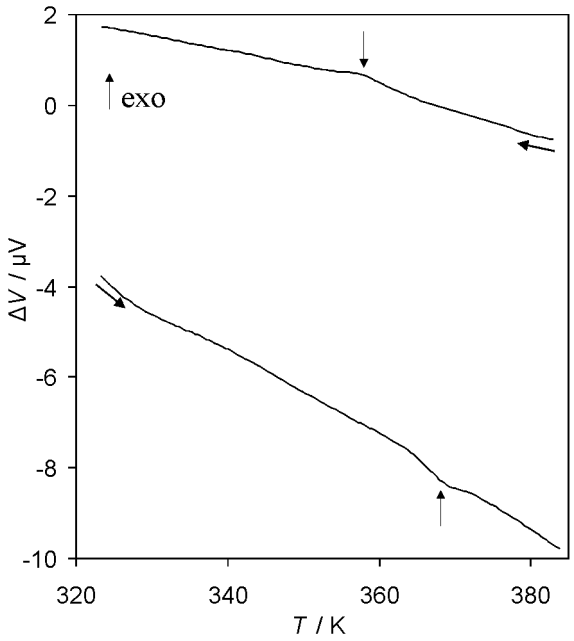

Figure 3.15 Section of the DTA diagram for Cs_8Sn_{44} recorded in the temperature range 298 - 393 K with 1 K min^{-1} heating/cooling rate. Vertical arrows show the endo- and exothermic peaks of the phase transition.

Further heating of Cs_8Sn_{44} to 1273 K with the rate of 5 K min^{-1} leads first to a weak peak around 510 K due to the melting of β-Sn, which arised from the partial decomposition of the clathrate (figure is not depicted here). A strong endothermic peak at 850 K (onset) is then observed, which according to the phase diagram (Appendix A) is attributed to peritectical decomposition of Cs_8Sn_{44} into Sn and $CsSn_2$. At 1103 K the relatively weak endothermic peak of the liquidus line is observed. On the cooling steps each peak has an exothermic corresponding phenomenon at 1083 K, 783 K and 488 K.

The DTA curves recorded with this heating/cooling rate showed virtually no effect of the phase transition, probably because the peaks became extremely broad. The XRPD diagram of the DTA residue after heating to 1273 K confirmed the presence of *α*-Cs_8Sn_{44} with a lower degree of crystallinity as well as the partial formation of *β*-Sn, in agreement with the synchrotron diffraction data. The thermal behavior of Rb_8Sn_{44} resembles that of Cs_8Sn_{44}. The onsets of the decomposition and liquidus points are at slightly lower temperature, namely 784 K and 1040 K, respectively.

The ternary clathrate $Rb_{1.42}Cs_{6.58}Sn_{44}$ melts incongruently at 846 K, indicating very similar thermal stability to Cs_8Sn_{44}, whereas the broad liquidus peaks are observed at about 1100 K (Figure 3.16). The exothermal reformation of the clathrate takes place on the cooling steps around 740 K, pointing out significant hysteresis. Once again, the partial decomposition even below 846 K is confirmed by the melting of *β*-Sn at 507 K. This becomes more visible on the second heating-cooling cycle, which hints for a certain irreversibility of the thermal effects. However, the DTA curves of $Rb_{1.42}Cs_{6.58}Sn_{44}$ did not show any peak below 373 K even with the use of lower heating/cooling rates, like 1 K min^{-1}. This is attributed to the diffuse character of the phase transition in $Rb_{1.42}Cs_{6.58}Sn_{44}$, in contrast to the binary clathrates.

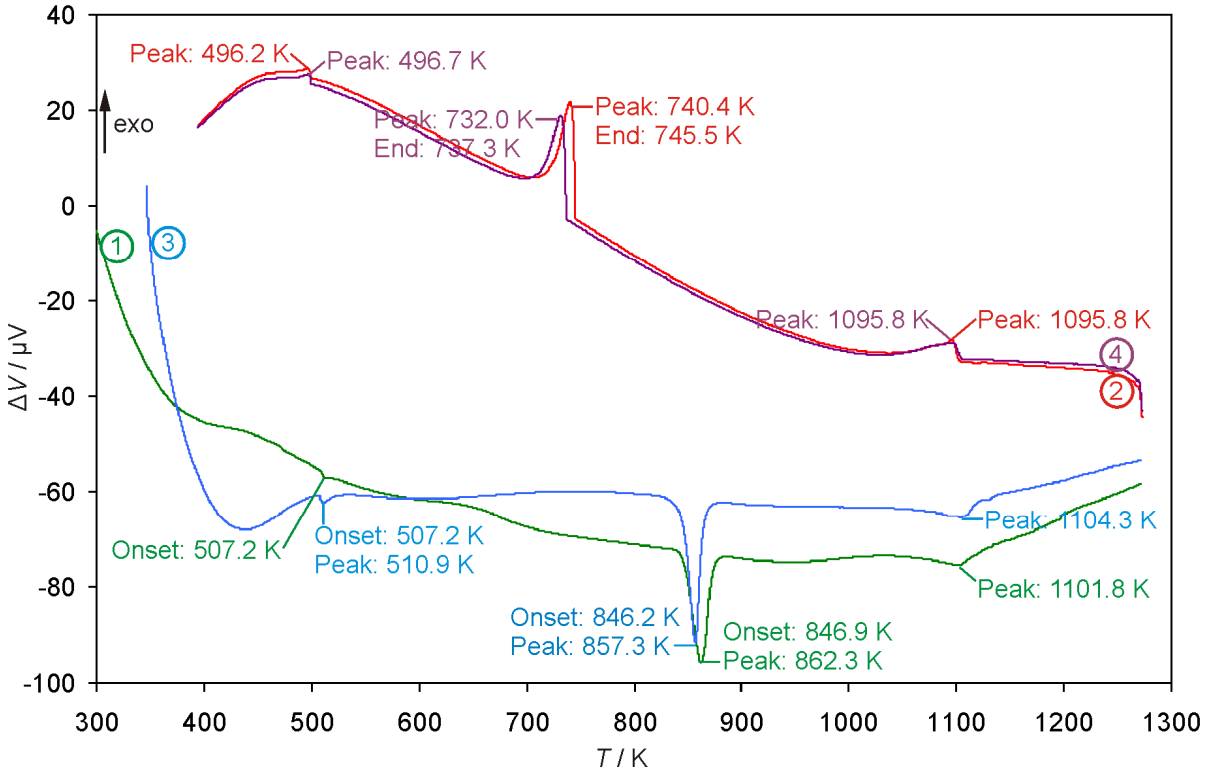

Figure 3.16 DTA diagram for $Rb_{1.42}Cs_{6.58}Sn_{44}$ in the temperature range 298 - 1273 K with 10 K min^{-1} heating/cooling rate. The numbers ①, ②, ③ and ④ denote the heating-cooling sequence. The isothermal steps (5 min duration) have been removed.

To investigate further the phase transition on the ternary compounds, the specific heat capacity (C_P) of $Rb_{1.42}Cs_{6.58}Sn_{44}$ was measured (Figure 3.17). From 4 K to about 340 K the heat capacity increases monotonically according to the Debye model, whereas in the region 340 - 375 K a symmetric anomaly with its maximum at 361 K occurs. The shape of the peak is indicative of a first-order phase transition. No hysteretical behavior between cooling and warming sequences was observed. The difference in the heat capacity ΔC_P (insert (a)) was obtained by subtracting a linear background mainly due to phonon contributions. The resulting entropy change of the anomaly for $Rb_{1.42}Cs_{6.58}Sn_{44}$ (insert (b)) is about ΔS = 2.5 J mol^{-1} K^{-1}, which accords with a first-order structural phase transition.

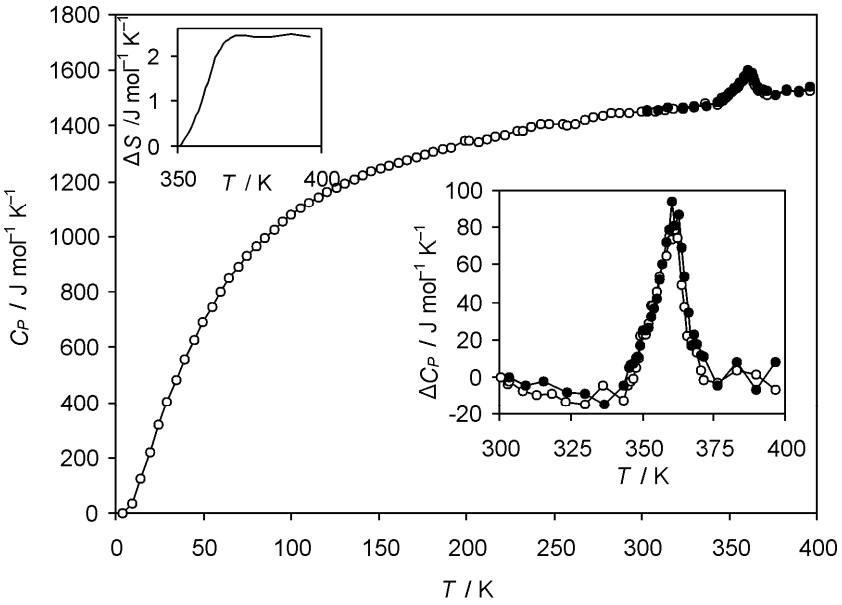

Figure 3.17 Specific heat capacity as a function of temperature for $Rb_{1.42}Cs_{6.58}Sn_{44}$. Insert (a) shows an enlarged view of the C_P anomaly after subtracting a linear background mainly due to phonon contributions. Insert (b) displays the entropy change observed during the phase transition. Closed circles denote heating steps and open circles cooling steps.

3.5 Mössbauer spectroscopy

The ^{119}Sn Mössbauer spectra of Rb_8Sn_{44} and Cs_8Sn_{44} were recorded at 293 K and indicate the variety of both formal oxidation states and local environment of the Sn atoms (Figure 3.18). The main peak broadens due to the similarity of the hyperfine parameters of possibly several components. To account for all possible contributions, the reconstruction of the distribution function[18] of the single Lorentz line position ($p(v)$) was performed. The reconstruction clearly shows that the two spectra are similar and each can be described as a superposition of three spectral components.

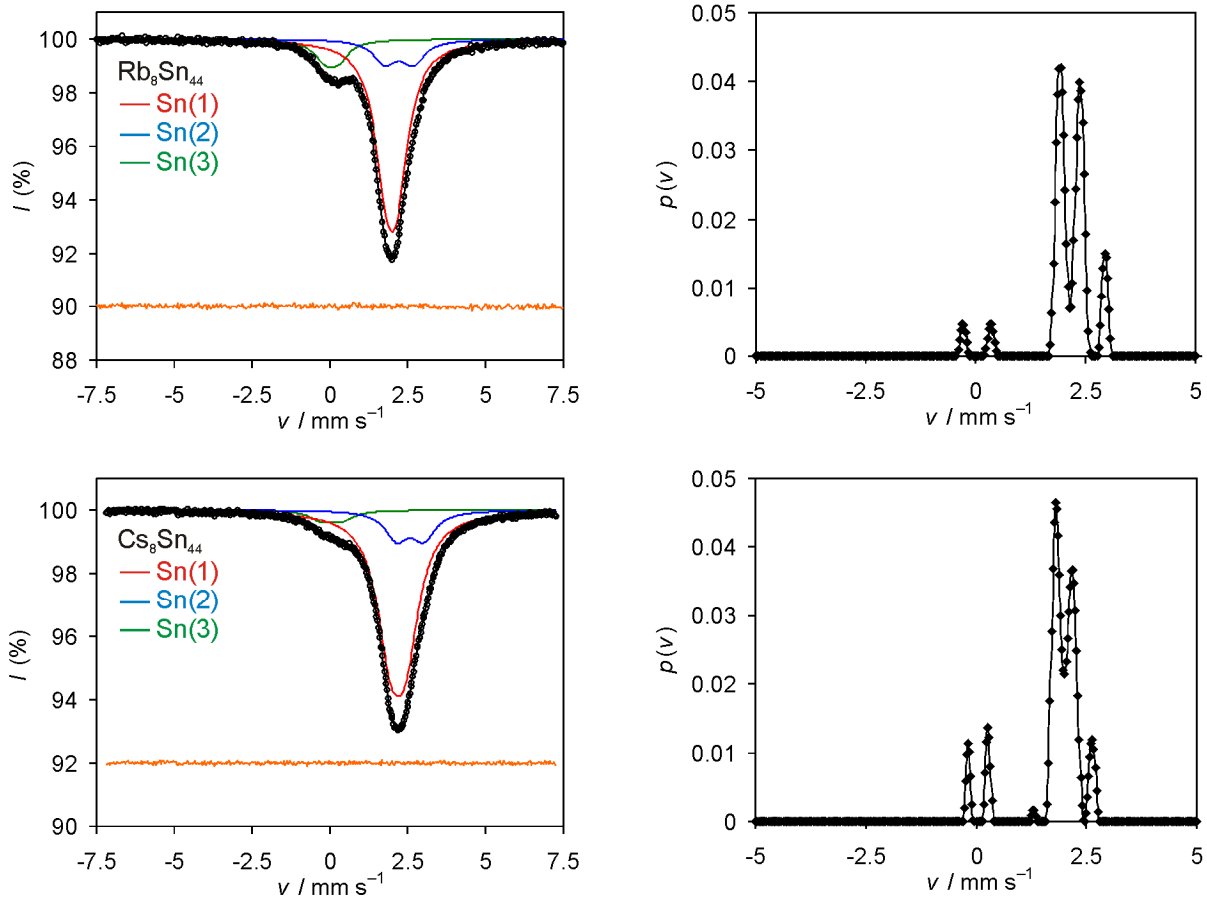

Figure 3.18 The ^{119}Sn Mössbauer spectra (left) of A_8Sn_{44} (A = Rb, Cs) measured at 293 K and the respective reconstruction (right) of the distribution function of the single Lorentz line position ($p(v)$). The orange lines represent the difference between the experimental and the simulated spectra.

The analysis of the isomer shifts (δ) and quadrupole splitting (Δ) suggests that the Sn(3) component should be attributed to an oxygen-containing Sn(IV) species (Table 3.15).[19] This component is most probably amorphous SnO_2 forming on the surface as the samples were exposed to oxygen for long periods. The remaining components are present in the ratio of 1 : 0.23 for Rb_8Sn_{44} and 1 : 0.21 for Cs_8Sn_{44}, which accords with the ratio of four-bonded and three-bonded Sn atoms, 1 : 0.222, in their crystal structures.

The Sn(1) component with δ = 2.11 and 2.19 mm s^{-1} for Rb_8Sn_{44} and Cs_8Sn_{44}, respectively is attributed to the four-bonded Sn atoms. These isomer shifts are close to the corresponding value for *α*-Sn (δ = 2.1 mm s^{-1}). A small increase of the isomer shifts compared to *α*-Sn is attributed to a slight augmentation of the electron density caused by Rb or Cs atoms. Since the isomer shift increases with the increase of the 5*s*-orbital population of ^{119}Sn, the experimentally observed shifts were used to calculate the orbital population of the Sn atoms according to the equation:

$$\delta_{Sn(1)} = -0.2 + 3.01n_{5s} - 0.2n_{5s}^2 - 0.17n_{5s}n_{5p}$$

where $3n_{5s} = n_{5p}$ are the populations of the 5*s* and 5*p* orbitals of Sn(1) for the sp^3 hybridized state.[20] The substitution of the observed isomer shifts for $\delta_{Sn(1)}$ results in n_{5s} = 1.01 and 1.06 for Rb_8Sn_{44} and Cs_8Sn_{44}, respectively. This confirms that the electropositive alkali metals transfer electron density to increase the orbital population of the Sn atoms. The higher population in the case of Cs_8Sn_{44} reflects the lower ionization energy for Cs. The non-zero values of the quadrupole splitting merely reflect the distortion of the tetrahedral environment of Sn atoms, whereas the slightly increased line width ($\Gamma_{½}$) indicates the contribution of five crystallographically independent Sn atoms to the Sn(1) component. The Sn(2) spectral component is attributed to the three-bonded Sn atoms, that surround the vacancy. This component displays a rather high value of the isomer shift ($\delta_{Sn(2)}$ = 2.4 - 2.6 mm s^{-1}) and quadrupole splitting ($\Delta_{Sn(2)}$ = 0.8 - 0.9 mm s^{-1}) typical for Sn atoms with three bonds and one lone electron pair. The localization of the electron pair leads to the increase of the 5*s* electron density as well as to the higher asymmetry of the electron density on the Sn atom.

Table 3.15 Hyperfine parameters for the ^{119}Sn Mössbauer spectra of A_8Sn_{44} at 293 K.

Compound	Component	δ / mm s^{-1}	Δ / mm s^{-1}	$\Gamma_{1/2}$ / mm s^{-1}	A (%)
Rb_8Sn_{44}	Sn(1)	2.11(2)	0.36(6)	0.90(1)	72.2(1)
	Sn(2)	2.36(8)	0.80(3)	0.93(9)	16.8(1)
	Sn(3)	0.07(1)	0.42(5)	0.85(4)	11.0(2)
Cs_8Sn_{44}	Sn(1)	2.19(1)	0.49(1)	1.05(1)	78.4(1)
	Sn(2)	2.57(9)	0.87(5)	0.91(4)	16.1(1)
	Sn(3)	0.05(1)	0.63(5)	0.90(5)	5.5(2)

The analysis of fine features of the spectra reveals only a subtle difference between the spectra acquired at various temperatures. Figure 3.19 shows a slight, almost within the experimental error, increase of the line half-width corresponding to the Sn(1) and

Sn(2) components. Such a minor line broadening, from about 0.9 mm s^{-1} at 77 K to about 1.1 mm s^{-1} at 363 K, along with the almost unchanged isomer shift and quadrupole splitting indicates that the structural changes in Rb_8Sn_{44} above 353 K are not accompanied by a variation in the environment of the Sn atoms, which is consistent with the following model. The phase transition in Rb_8Sn_{44} is an order-disorder process, upon which various domains of the crystalline phase orient randomly, virtually without changing the local environment of the Sn atoms, leading to the formation of the high-temperature "average" structure, similar to the situation reported for $Sn_{20.5}As_{22}I_8$.[21] The latter possesses domains with a variation of the vacancy concentration, thus, with uneven distribution of the two kinds of Sn atoms within an average unit cell. In turn, this causes a slight variation in the hyperfine parameters for these atoms upon passing from one domain to another. The difference between the hyperfine parameters is too low itself to be observed, but the averaging of these parameters leads to the line broadening. In Rb_8Sn_{44}, the low-temperature modification is ordered and apparently devoid of the domain misalignment. Therefore it is characterized by a line width of 0.8 mm s^{-1} that is only slightly higher than that typically observed for the ^{119}Sn nucleus.[19]

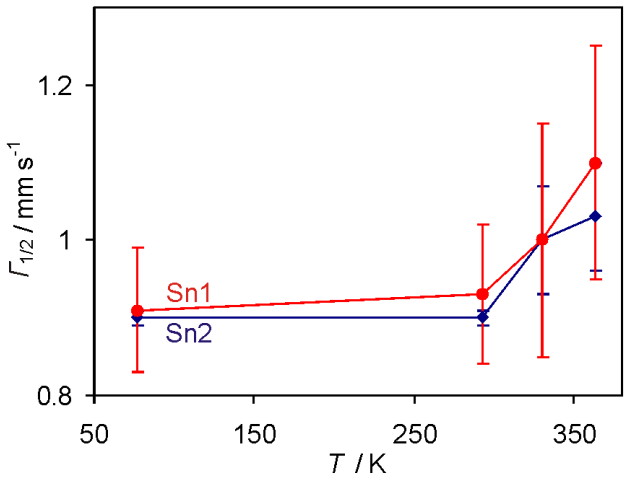

Figure 3.19 Temperature dependence of the line width ($\Gamma_{1/2}$) with standard deviations for the Sn(1) and Sn(2) components in the Mössbauer spectra of Rb_8Sn_{44}.

3.6 Raman spectroscopy

The Raman spectra at ambient conditions for Rb_8Sn_{44}, $Rb_{1.4}Cs_{6.6}Sn_{44}$ and Cs_8Sn_{44} are shown in Figure 3.20. The rattling vibrations of guest Rb and Cs atoms occur in a low frequency region 25 - 40 cm^{-1}. The higher-frequency Sn framework vibrations occur at 44 - 170 cm^{-1}. More specifically, the rattling modes were observed at 34 and 40 cm^{-1} for Rb_8Sn_{44}, 31 and 36 cm^{-1} for $Rb_{1.4}Cs_{1.6}Sn_{44}$ and 25 and 32 cm^{-1} for Cs_8Sn_{44}. Raman active modes can only stem from the guest atoms in the large, low symmetry tetrakaidecahedra whereas no active mode is expected for the smaller pentagonal dodecahedra of the type-I clathrates.[23]

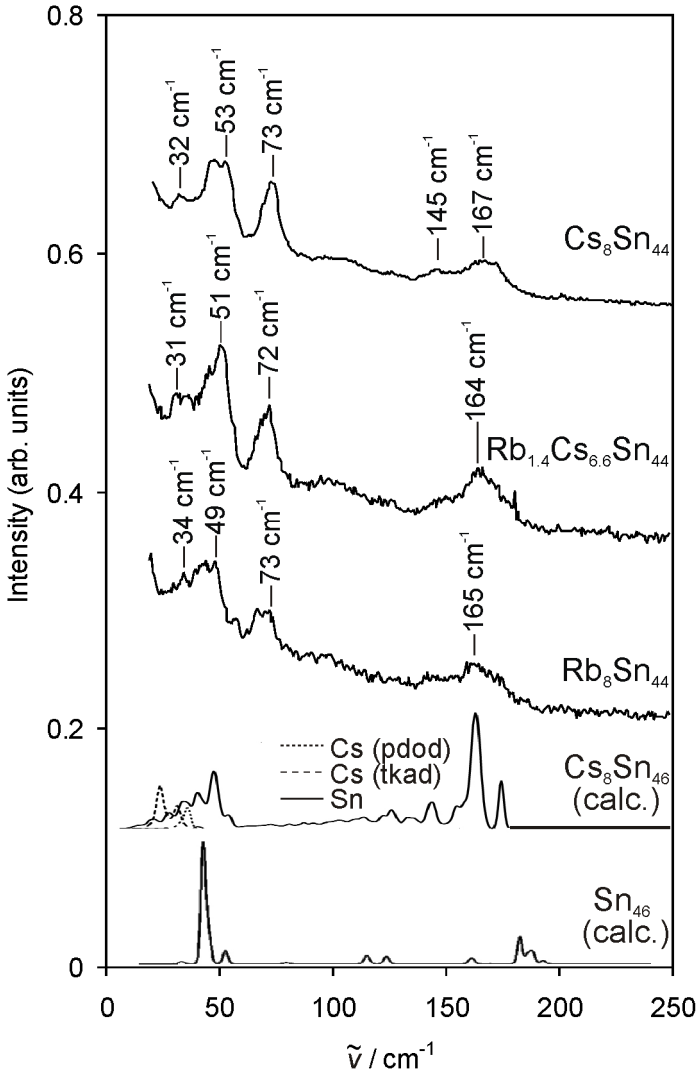

Figure 3.20 Raman spectra of the defect clathrates Rb_8Sn_{44}, $Rb_{1.4}Cs_{6.6}Sn_{44}$ and Cs_8Sn_{44}. For comparison, the theoretical PDOS for hypothetical Cs_8Sn_{46}[22] and the theoretical spectrum of the guest-free clathrate Sn_{46} are given.[23]

The Rb rattling modes are located at slightly higher frequencies than the corresponding Cs bands. Usually, the rattling frequency (ν) can be estimated by the

relationship of a harmonic oscillator model:

$$v = \frac{1}{2\pi}\sqrt{\frac{k}{m}}$$

where k is the bonding strength and m the oscillator's mass. If one assumes an equal bonding strength, the v_{Rb} / v_{Cs} ratio can be calculated at about 1.25 by using m_{Rb} = 85.5 and m_{Cs} = 132.9. Taking into account that the wavenumber ratios are 34 / 25 = 1.36 and 40 / 32 = 1.25, the k values, i.e. the guest-host interactions, are nearly equal. Although the k is expected to be sensitive for the guest-host distance, this result is reasonable because Sn clathrates have large cages and the difference in both guest sizes is relatively small (Cs / Rb = 1.14). In the case of $Rb_{1.4}Cs_{6.6}Sn_{44}$, the spectral bands are broad because the tetrakaidecahdra are statistically occupied with both types of guest atoms, namely SOF(Rb) = 0.08 and SOF(Cs) = 0.92.

As already mentioned, the bands over 44 cm^{-1} are attributed to the Sn framework vibrations. The results are well compared to the phonon density of states for the hypothetical Cs_8Sn_{46}[22] and the Raman spectrum of the guest-free model Sn_{46} calculated by a bond-polarizability model.[23] However, the strong extra peaks at 69 and 73 cm^{-1} for Rb_8Sn_{44}, at 72 cm^{-1} $Rb_{1.4}Cs_{6.6}Sn_{44}$ and at 73 cm^{-1} for Cs_8Sn_{44} seem to originate from the framework vacancies. The neighbouring atoms drift towards these vacancies leading to interatomic distances typical for 3b-Sn^{-1} species. These vacancy-induced vibrational modes are observed for the first time in the group-14 defect clathrates. Other defect-free Sn clathrates like $Cs_8Ga_8Sn_{38}$[23] and $Rb_8Hg_4Sn_{42}$ (Chapter 5.5) lack this characteristic. Finally, Figure 3.21 shows the temperature dependence of the Rb_8Sn_{44} Raman spectra in the region 293 - 389 K. One can discern only a slight intensity decrease and broadening of the vacancy-induced vibrational modes around 70 cm^{-1} which are expected to be the most sensitive to the vacancy disordering. This indicates that the chemical environment of the Sn atoms remains the same even in β-Cs_8Sn_{44}.

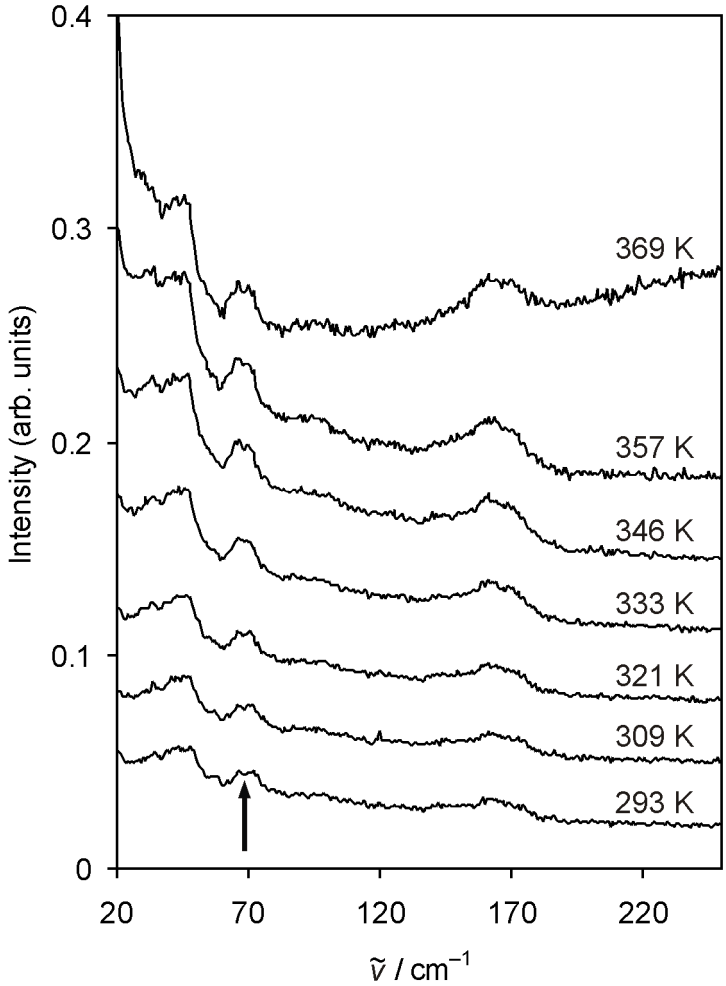

Figure 3.21 Temperature dependence of the Rb_8Sn_{44} Raman spectra from 293 K to 369 K over the order-disorder phase transition point at 353 K. The vertical arrow indicates the Sn vacancy-induced bands around 70 cm^{-1}.

3.7 Mechanism of the phase transition

The solid-solid phase transitions are usually classified according to the structural and thermodynamic changes that occur during the transformation.[24] Regarding first the atomic rearrangement, the low-energy enantiotropic transformation in $Rb_xCs_{8-x}Sn_{44}$ ($0 \le x \le 8$) can be rationalized as a displacive rather than a reconstructive process. Two ways of achieving the migration of certain Sn atoms are proposed (Figure 3.22): a) A three-step mechanism including migration via two split positions within a six-membered ring is indicated as solid arrows. Migration occurs along spiro-connected six-membered rings only. Due to the cubic symmetry the spiro motive shown in Figure 3.19 appears in chains along all three directions in space and allows atoms' rearrangement in the framework. b) A four-step mechanism with migration through two split and one non-split atomic positions, the latter being part of five-membered rings only indicated as dashed arrows. Large displacement vectors of the involved atoms favor the first mechanism.

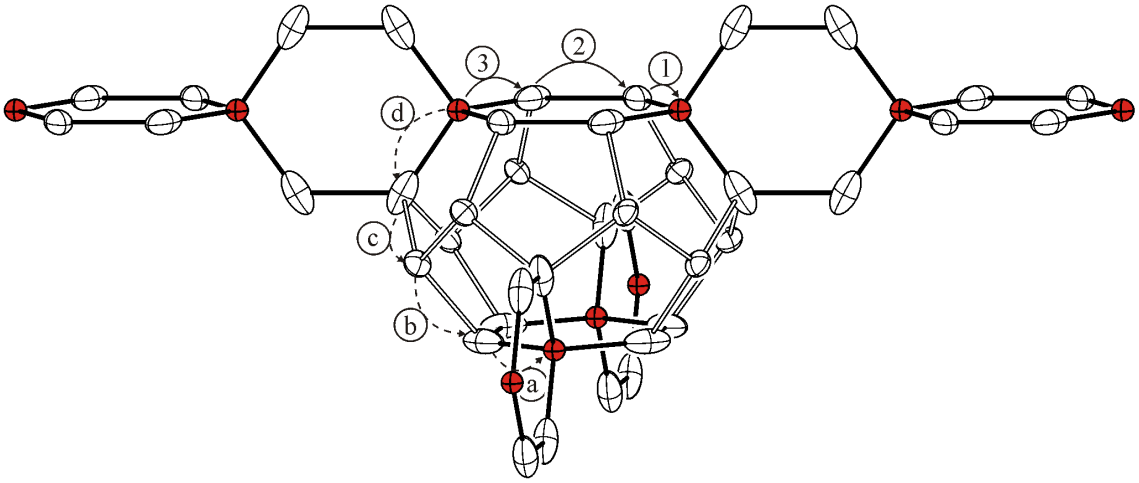

Figure 3.22 Two possible mechanisms of atom migration for the $Pm\bar{3}n$ to $Ia\bar{3}d$ phase transition. Fully and partially occupied Sn sites are drawn in white and red color, respectively with thermal ellipsoids at 80% probability level, without split positions for the atoms adjacent to the vacancies.

In thermodynamic terms, the order-disorder transition in A_8Sn_{44} (A = Rb, Cs) is considered as first-order mechanism, due to the latent heat and the hysteresis found by thermal analysis. As for the ternary $Rb_{1.4}Cs_{6.6}Sn_{44}$, the transition occurs in a more diffuse manner and its thermodyamic order cannot be deduced with certainty. First-order phase transitions, like in CsCl, always show an abrupt enthalpy change and significant hysteresis whereas typical cases of second-order phase transitions, like in Cu_3Au, show -apart from the crystallographic group-subgroup relationship and the relatively wide temperature range for the transformation- an asymmetric change (λ type) in the heat capacity.[24]

3.8 Discussion

The X-ray diffraction studies and thermal analysis have established a temperature-induced order-disorder phase transition in $Rb_xCs_{8-x}Sn_{44}$ ($0 \le x \le 8$) well below their melting point. The transformation is completely reversible and quenching of the compounds from 373 K or 973 K into liquid N_2 does not give rise to the high-temperature modification. On the other hand, application of external pressure up to 500 MPa at room temperature has no effect on the superstructure, probably because both modifications of the clathrates have the same density. The lighter analogue K_8Sn_{44} was also synthesized but the low crystallinity of the samples rendered impossible the determination of the superstructure. No DTA peak was found for this compound in the temperature range 293 - 400 K. The *β* modification of $Rb_xCs_{8-x}Sn_{44}$ ($0 \le x \le 8$) possesses higher symmetry and lower ordering than the *α* form. As expected, this more disordered modification is favored at elevated temperatures by means of an entropy-driven phase transition.

In general, the formation of a superlattice can avoid under- or mixed- occupancy of certain atomic sites. Four other examples of superstructures have been discussed so far for doped and/or defect type-I clathrates: a) $I_8[Sn_{14}In_{10}P_{21.2}\square_{0.8}]$ crystallizes in the tetragonal space group $P4_2/m$ exhibiting partial ordering of the defects,[25] b) $Ba_8[Cu_{16}P_{30}]$ (the only semiconducting clathrate that does not contain group-14 elements) crystallizes in the orthorhombic space group *Pbcn* and exhibits full ordering of the Cu and P atoms,[26] c) $[Si_{46-x}P_x]Te_y\square_{8-x}$ ($y = 7.35, 6.98, 6.88$, $x \le 2y$)[27] in the cubic space group $Pm\bar{3}$ with segregation of the Si and P sites and partial ordering of the Te vacancies and finally d) $Ba_8Ge_{43}\square_3$ is characterized as a fully ordered superstructure when fast quenched from 1073 K or as partly ordered when allowed to cool slowly to ambient conditions.[28] In fact, the occurrence of a superstructure in Ba_8Ge_{43} was first proposed with the aid of electron diffraction experiments, although the crystal structure was not completely solved at that time.[29]

In $Rb_xCs_{8-x}Sn_{44}$ ($0 \le x \le 8$) and Ba_8Ge_{43} a “klassengleiche” symmetry reduction from $Pm\bar{3}n$ to $Ia\bar{3}d$ takes places. However, the absence of a distinct transition temperature and the higher thermodynamic stability of the disordered modification for Ba_8Ge_{43} contradict with the results for A_8Sn_{44} (A = Rb, Cs). Another crucial difference in the latter is the crystallographic disorder found even for the *α* modification. Full ordering of the two vacancies could occur only in an enlarged, isomorphic $3 \times 3 \times 3$ unit cell of $Pm\bar{3}n$ symmetry or a $6 \times 6 \times 6$ unit cell of $Ia\bar{3}d$ symmetry, where the underoccupied Sn1

Wyckoff site of the initial cell would split to seven or nine crystallographically independent sites, respectively.[30] Nevertheless, no such superlattices were found by single-crystal and synchrotron diffraction analysis above 90 K. The full ordering of the defects Ba_8Ge_{43} is also reflected in the larger deviation of the guest atom Ba from the ideal center of the tkad. The larger dislocation of the Ba atoms by 0.0844 Å originates from the presence of a full vacancy on each framework hexagon whereas in A_8Sn_{44} from the only partially vacant sites. The corresponding dislocation for Cs_8Sn_{44} was experimentally determined at 0.0593(7) Å.

The composition of $Rb_xCs_{8-x}Sn_{44}$ ($0 \le x \le 8$) complies with the Zintl concept. According to the crystallographic analysis, the cationic sites are fully occupied whereas the free refinement of the underoccupied Sn sites led always to SOFs that within the standard 3σ deviation fulfill the formal composition A_8Sn_{44}. In the ternary $Rb_xCs_{8-x}Sn_{44}$ (x = 2.1, 1.4, 1.3), both types of framework cavities show clear trend towards encapsulation of the larger alkali metal, namely Cs rather than Rb (Figure 3.23). A certain homogeneity range close to the composition $Rb_2Cs_6Sn_{44}$ is observed, although the cations are not fully ordered even in the long-annealed samples.

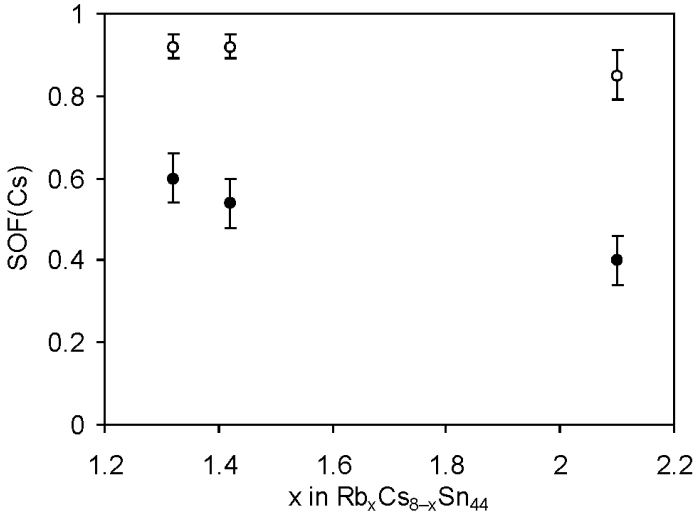

Figure 3.23 Site occupation factors with standard deviations of the Cs atoms in pdod (closed circles) and tkad (open circles) for $Rb_xCs_{8-x}Sn_{44}$ (x = 1.32, 1.42, 2.1).

Some other cases of clathrate-I compounds with two different types of encaged atoms have been so far structurally characterized: a) the compound $K_{1.6}Cs_{6.4}Sn_{44}$[8] that also exhibits mixed occupancy in both cationic positions, b) solid solutions of polycationic $[Sn_{24}P_{19.3}]Br_xI_{8-x}$ ($0 \le x \le 8$) and $[Sn_{24}P_{19.3}]Cl_yI_{8-y}$ ($y \le 0.8$),[31] c) $Na_2Ba_6Si_{46}$ with pdod and tkad fully occupied by Na and Ba, respectively[32] and d) $K_6Eu_2[Ga_{10}Ge_{36}]$[33] also with fully ordered cations. The rattling of the encaged cations is a significant (in)stability factor and

therefore the well fitting Cs radius in the relatively large framework cavities of the Sn atoms justifies the trend towards type-I clathrate formation. Lighter alkali metals would result to both type-I and the corresponding type-IX $A_{8-x}Sn_{25}$ clathrate, whereas mixing of two alkali metals of very different size such as Na and Cs would give rise to type-II and type-III clathrates.[34,35]

Both Mössbauer and Raman spectroscopy explicitly determine the negatively charged, three-bonded Sn atoms as a result of introducing vacancies in the framework. Furthermore, no significant difference is observed in the spectra for *α*-Rb_8Sn_{44} and *β*-Rb_8Sn_{44}, implying that the phase transition takes place without altering the local environment of the Sn atoms (Figure 3.9c), but by varying the concentration of vacancies in different domains of the crystal.

3.9 Literature

[1] J. Gallmeier, H. Schäfer, A. *Z.* Weiss *Naturforsch.* **1969**, *24b*, 665.

[2] J. Kasper, P. Hagenmuller, M. Pouchard, C. Cros *Science* **1965**, *150*, 1713.

[3] H.-G. von Schnering *Nova Acta Leopoldina* **1985**, *59*, 168.

[4] Yu. Grin, L. Melekhov, K. Chuntonov, S. Yatsenko *Kristallografyia* **1987**, *32*, 497.

[5] G. Ramachandran, P. McMillan, J. Dong, O. Sankey *J. Solid State Chem.* **2000**, *154*, 626.

[6] M. Baitinger *Ph. D. Thesis*, T.U. Darmstadt **2000**.

[7] S. Bobev, S. Sevov *J. Solid State Chem.* **2000**, *153*, 92.

[8] J. T. Zhao, J. Corbett *Inorg. Chem.* **1994**, *33*, 5721.

[9] H.-G. von Schnering, R. Kröner, M. Baitinger, K. Peters, R. Nesper, Yu. Grin *Z. Kristallogr. NCS* **2000**, *215*, 205.

[10] G. S. Nolas, B. C. Chakoumakos, B. Mahieu, G. J. Long, T. J. R. Weakley *Chem. Mater.* **2000**, *12*, 1947.

[11] S. Kauzlarich *Chemistry, Structure and Bonding of Zintl Phases and Ions*, VCH Publishers, Inc. **1996**.

[12] C. Myles, J. Dong, O. Sankey *Phys. Rev. B* **2001**, *64*, 165202(11).

[13] L. Mollnitz, N. Blake, H. Metiu *J. Chem. Phys.* **2002**, *117*, 1302.

[14] F. Dubois, T. Fässler *J. Am. Chem. Soc.* **2005**, *127*, 3264.

[15] M. Baitinger, Yu. Grin, H.-G. von Schnering, R. Kniep *Z. Kristallogr. NCS* **1999**, *214*, 457.

[16] N. L. Okamoto, M. W. Oh, T. Nishii, K. Tanaka, H. Inui *J. Appl. Phys.* **2006**, *99*, 033513.

[17] I. Barin, O. Knacke *Thermochemical Properties of Inorganic Substances*, Springer-Verlag, Berlin, **1973**.

[18] I. Presniakov, A. Baranov, G. Demazeau, V. Rusakov, A. Sobolev, J. A. Alonso, M. J. Martinez-Lope, K. Pokholok *J. Phys.: Condens. Matter*. **2007**, *19*, 036201.

[19] J. G. Stevens, M. A. Goforth *^{119}Sn Mössbauer Spectroscopy*; Mössbauer Effect Data Center, Asheville, NC, **1993**.

[20] P. A. Flinn *Mössbauer isomer shifts* edited by G. K. Shenoy, F. E. Wagner: Eds. Amsterdam. North Holland. **1978**.

[21] J. V. Zaikina, K. A. Kovnir, A. V. Sobolev, I. A. Presniakov, Yu. Prots, M. Baitinger, W. Schnelle, A. V. Olenev, O. I. Lebedev, G. van Tendeloo, Yu. Grin, A. V. Shevelkov *Chem. Eur. J.* **2007**, *13*, 5090.

[22] J. S. Tse, Z. Li, K. Uehara *Europhys. Lett.* **2001**, *56*, 261.

[23] C. W. Myles, J. Dong, O. F. Sankey, C. A. Kendziora, G. S. Nolas *Phys. Rev. B* **2002**, *65*, 235208.

[24] A. R. West *Solid State Chemistry and its Applications*, John Wiley & Sons Ltd., **1984**.

[25] M. M. Shatruk, K. A. Kovnir, M. Lindsjö, I. A. Presniakov, L. A. Kloo, A. Shevelkov *J. Solid*

State Chem. **2001**, *161*, 233.

[26] J. Duenner, A. Z. Mewis *Anorg. Allg. Chem.* **1995**, *621*, 191.

[27] J. Zaikina, K. A. Kovnir, U. Schwarz, H. Borstmann, A. V. Shevelkov *Z. Kristallogr. NCS* **2007**, *222*, 177.

[28] W. Carrilo-Carbera, S. Budnyk, Y. Prots, Yu. Grin *Z. Anorg. Allg. Chem.* **2004**, *630*, 2267.

[29] R. Herrmann, K. Tanigaki, T. Kawaguchi, S. Kuroshima, O. Zhou *Phys. Rev. B* **1999**, *60*, 13245.

[30] H. Wondratschek, U. Müller, *International Tables for Crystallography, Volume A1 Symmetry Relations Between Space Groups*, Kluwer Academic Publishers, **2004**.

[31] J. Zaikina, W. Schnelle, K. Kovnir, A. Olenev, Yu. Grin, A. Shevelkov *Solid State Sci.* **2007**, *9*, 664.

[32] M. Baitinger, H.-G von Schnering, J.-H. Chang, K. Peters, Yu. Grin *Z. Kristallogr. NCS* **2007**, *222*, 87.

[33] S. Paschen, S. Budnyk, U. Köhler, Yu. Prots, K. Hiebl, F. Steglich, Yu. Grin *Physica B* **2006**, *383*, 89.

[34] S. Bobev, S. Sevov *J. Am. Chem. Soc.* **1999**, *121,* 3795.

[35] S. Bobev, S. Sevov *J. Am. Chem. Soc.* **2001**, *123,* 3389.

4. Phase-transition effects on the physical properties of $Rb_xCs_{8-x}Sn_{44}$ (0 ≤ x ≤ 8)

4.1 Introduction

In principal, a crystal is perfect in only one way but may be imperfect in an infinity of ways.[1] The defects, regardless of their dimensionality, always reduce the flow of heat and electric current in the solid. The framework vacancies in $A_8Sn_{44}\square_2$ may also be considered as isolated point imperfections, which drastically alternate the electronic band structure, in comparison to the hypothetical A_8Sn_{46}.[2,3] In this context, the effect of the order-disorder phase transition on the magnetic and transport properties in the clathrate compounds is studied.

4.2 Einstein and Debye temperatures

As already mentioned in Chapter 3.3.3, the crystal structure of the binary clathrates A_8Sn_{44} (A = Rb, Cs) was also refined from the multi-temperature synchrotron data. The displacement parameters of all Sn atoms (average value) and the A1 atoms were isotropically refined whereas the A2 atoms were anisotropically refined. Figure 4.1 shows the atomic displacement parameters for Rb_8Sn_{44} in the temperature range 90 - 300 K. The ADPs of Rb2 (U_{22} = U_{33}) in the equatorial plane of the large tkad have the largest amplitude, whereas the perpendicular vibrations, the guest-atom vibrations in the pdod and the host structure vibrations have similar smaller magnitude.

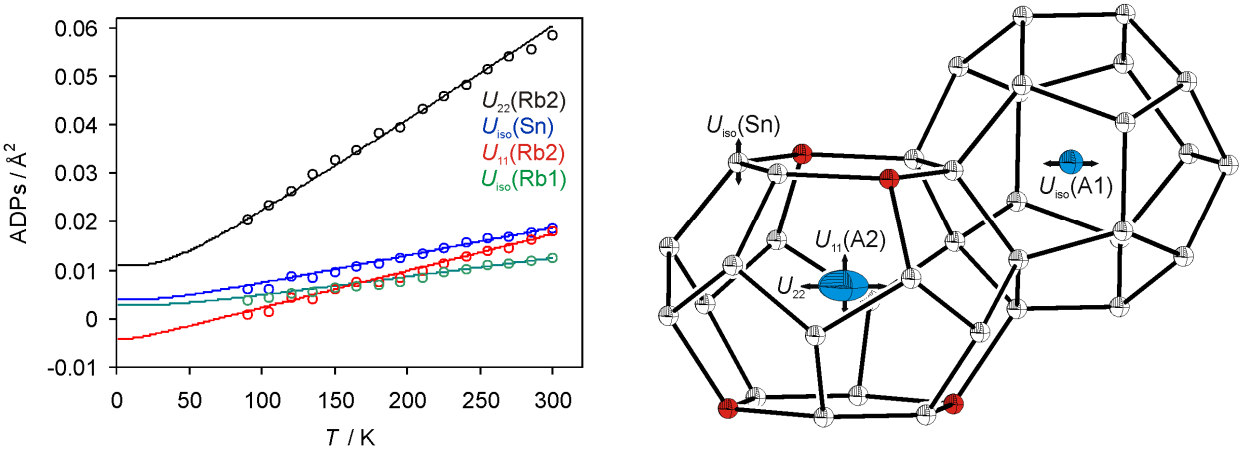

Figure 4.1 Temperature dependence of the ADPs extracted from the synchrotron Rietveld refinements for Rb_8Sn_{44}. The solid lines represent Einstein fits and a Debye fit to the guest and host atoms, respectively.

The multi-temperature anisotropic ADPs may provide qualitative information about the guest atom dynamics. The guest-atom ADPs are modeled as an Einstein oscillator using the function:

$$U_{ii} = \frac{\hbar^2}{2mk_B\theta_{E,ii}} \coth\left(\frac{\theta_{E,ii}}{2T}\right) + d_{ii}^2$$

where d is the temperature-independent disorder and θ_E the Einstein temperature. The index ii refers to the direction of vibration vector. The disorder parameters are strongly affected by systematic errors such as absorption. The ADPs are mainly determined by the high-angle reflections, where the powder diffraction data are weak and uncorrected the absorption effects are larger. However, the slope of the ADP curve is relatively unaffected by such systematic errors and reliable Einstein temperatures can be extracted. The ADPs of the host structure can be better approximated by the Debye expression:

$$U_{iso} = \frac{3\hbar^2 T}{mk_B\theta_D^2}\left[\frac{T}{\theta_D}\int_0^{\theta_D/T}\frac{x}{e^x+1}dx + \frac{\theta_D}{4T}\right] + d^2$$

where θ_D is the Debye temperature and d describes the temperature-independent disorder.

The extracted Einstein and Debye temperatures for Rb_8Sn_{44} are listed in Table 4.1. The free refinement of the disorder parameter resulted in an unphysical negative value, which points to a slight systematic error in the determination of the ADPs. The Rb1 atom in the small cages has the largest Einstein temperature, namely 92(1) K. The perpendicular displacement parameter U_{11} of the Rb2 in the large cages has the intermediate value of 81(1) K and the lowest value is found for the parallel displacement U_{22} at 54.2(3) K. A similar decreasing trend for the guest atom Einstein temperatures was found for Ba in $Ba_8Ga_{16}Ge_{30}$ (U_{iso}(Ba1) = 108(1) K, U_{11}(Ba2) = 90(1) K and U_{22}(Ba2) = 62(1) K).[4] However, the observed $\theta_{E,ii}$ for Rb_8Sn_{44} are slightly lower than the corresponding values for $Ba_8Ga_{16}Ge_{30}$. The Einstein temperature is determined by the strength of the guest-host interaction as well as the atomic mass of the guest. A weaker bonding and a larger guest atom mass causes a lower Einstein temperature. Rb has lower $\theta_{E,ii}$ despite that its mass is 1.61 times smaller than that of Ba. The ionic radius of Rb^+ (1.52 Å) is larger than that of Ba^{2+} (1.35 Å).

Table 4.1 Einstein and Debye temperatures for A_8Sn_{44} extracted from fits to the ADPs obtained from the multi-temperature powder diffraction data collected below 300 K.

	θ_E / K	d / Å
U_{iso}(Rb1)	92(1)	0.0012(3)
U_{11}(Rb2)	81(1)	–0.0065(4)
U_{22}(Rb2)	54.2(3)	0.0073(5)
	θ_D / K	d / Å
U_{iso}(Sn)	152(1)	0.0002(2)

In a simple approximation the space available per guest atom can be estimated by disregarding the host structure atoms, i.e. the unit cell volume divided by the number of guest atoms. This gives 219 and 157 $Å^3$/(guest atom) for Rb^+ and Ba^{2+}, respectively. Taking the difference in guest atom volume into account, the Rb^+ guest atom in Rb_8Sn_{44} has 1.06 time more space than Ba^{2+} in $Ba_8Ga_{16}Ge_{30}$. Since the available space is comparable for Rb and Ba while the mass is lower for Rb, the lower Einstein temperature points to a significantly weaker bond for Rb. Chemically it is not surprising since Rb is in +1 oxidation state compared with Ba, which is in +2 oxidation state.

The Debye temperature for Rb_8Sn_{44} was found to be 152(1) K, which is fairly close to that for elemental Sn (θ_D = 200 K), but considerably lower than for other clathrates such as $Ba_8Ga_{16}Ge_{30}$ (θ_D = 269(7) K). The reason for this is the mass of the host structures, which enters the Debye expression inversely. It can be estimated that the Debye temperature of $Ba_8Ga_{16}Ge_{30}$ should be about 1.66 times larger than that of Rb_8Sn_{44} due to the larger mass of Sn compared with Ga/Ge. Experimentally, it is 1.77 times larger. Despite the simplification of the Debye model the result shows that reasonable Debye temperature values can be extracted even in complex systems such as the clathrates.

The high-temperature diffraction data show a linear increase of the ADPs without visible effect over the phase transition (Figure 4.2). The displacement factors of Rb_8Sn_{44} and Cs_8Sn_{44} are similar, except for the equatorial vector of the alkali metals in the tkad, where U_{22}(Rb1) is about 1.3 times larger than U_{22}(Cs1). Unfortunately, the high-temperature data were collected close to the absorption edge of Sn (λ = 0.4245 Å) and the refinements are affected by anomalous scattering and increased absorption. The f-prime value for atomic Sn is f'_{Sn}(0.4326 Å) = –3.3 at the chosen wavelength and is depends strongly on the radiation wavelength as well as the valence of Sn. The close proximity to the absorption edge of Sn causes a relatively poor description of Sn and together with increased absorption effects this strongly affects the ADPs.

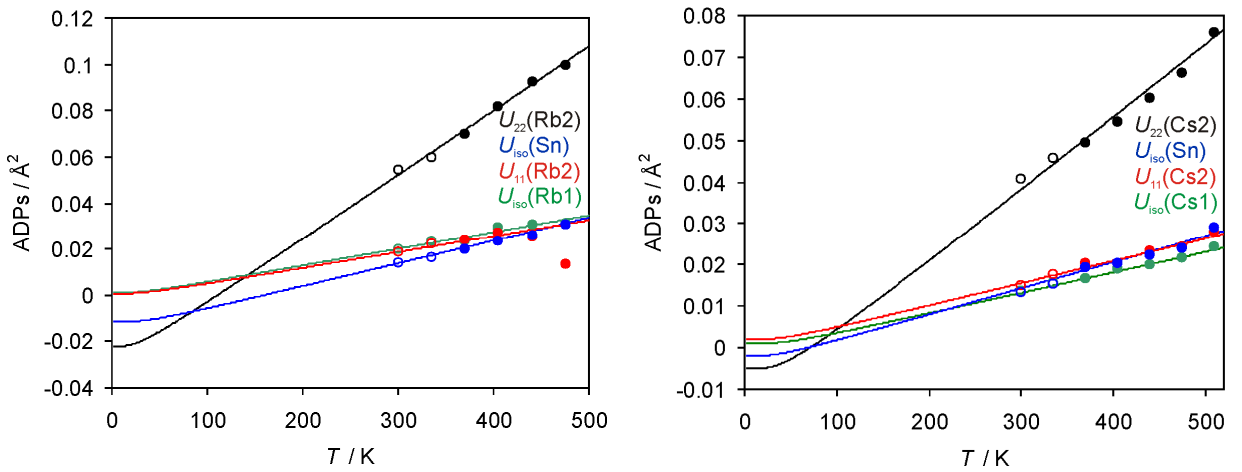

Figure 4.2 Temperature dependence of the ADPs extracted from the synchrotron Rietveld refinements for Rb_8Sn_{44} (left) and Cs_8Sn_{44} (right) above 300 K. The solid lines represent Einstein fits and a Debye fit to the guest and host atoms, respectively. Open cricles refer to the *α*-modification and closed circles to the *β*-modification.

The lattice thermal conductivity is, to a first approximation, proportional to the Debye temperature through the velocity of sound (v_s):

$$\kappa_L = \frac{C_P v_s d}{3}$$

C_P refers to the heat capacity and d to the distance between scattering centers. Thus, Rb_8Sn_{44} should have considerably lower thermal conductivity than $Ba_8Ga_{16}Ge_{30}$ (κ_L = 1.4 W m^{-1} K^{-1}) but in fact the values are comparable.[5] This could be due to the mass variation in $Ba_8Ga_{16}Ge_{30}$ though this effect is fairly small as Ga and Ge are neighboring elements in the periodic table. Another possible explanation is that Rb has weaker bonds than Ba and as a consequence the scattering of acoustic phonons is lower in Rb_8Sn_{44} than in $Ba_8Ga_{16}Ge_{30}$.

4.3 Magnetic properties

The magnetic susceptibility of the clathrates was measured on microcrystalline samples. A_8Sn_{44} (A = Rb, Cs) exhibit weak and almost temperature-independent diamagnetic behavior. In general, no significant differences between the heating and cooling steps are observed. The structural transition at 353 K and 363 K for Rb_8Sn_{44} and Cs_8Sn_{44} respectively, does not affect the magnetization as indicated by high- and low-field measurements. Figure 4.3 shows the magnetic behavior of Cs_8Sn_{44}. Traces of *β*-Sn, below the detection limit of XRPD, were found as the overall magnetization increased rapidly below 20 K. This impurity was also detectable in all samples via the superconducting-magnetic transition at 3.7 K. By subtracting the paramagnetic contributions of the impurity and the diamagnetic core increments of the clathrate, a weak residual diamagnetism of $\chi(Cs_8Sn_{44}) = -2.3\ 10^{-8}\ m^3\ mol^{-1}$ is found.

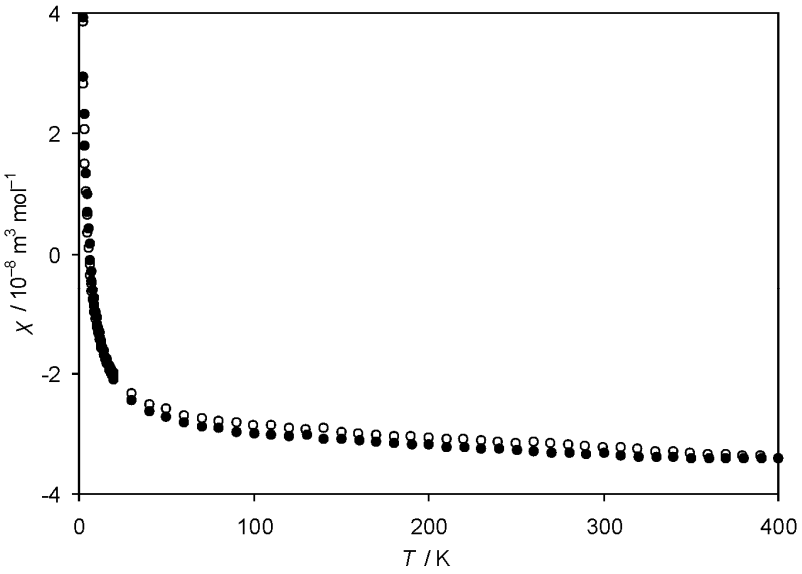

Figure 4.3 Magnetic susceptibility for Cs_8Sn_{44} in a field of 0.5 Tesla. Closed circles denote heating steps and open circles cooling steps.

4.4 Electrical resistivity

Electrical resistivity measurements were performed on single crystals of Rb_8Sn_{44}, $Rb_{1.42}Cs_{6.58}Sn_{44}$ and Cs_8Sn_{44} (Figure 4.4). Down to 360 K, the electrical resistivity increases with decreasing temperature as anticipated for semiconductors.[6,7] In the temperature range 360 - 310 K, the resistivity increase is even more pronounced and characterized by appreciable differences between cooling and heating sequences. The hysteresis is larger in the case of $Rb_{1.42}Cs_{6.58}Sn_{44}$ where the characteristic temperatures of the reversal points of the cooling and heating curves are $T_2 \approx 332$ K and $T_1 \approx 350$ K, respectively. In all samples the electrical resistivity changes during the disorder-order transition by a factor of about 4. Noteworthy, the ternary compound is significanlty less conductive than the binary compounds Rb_8Sn_{44} and Cs_8Sn_{44}.

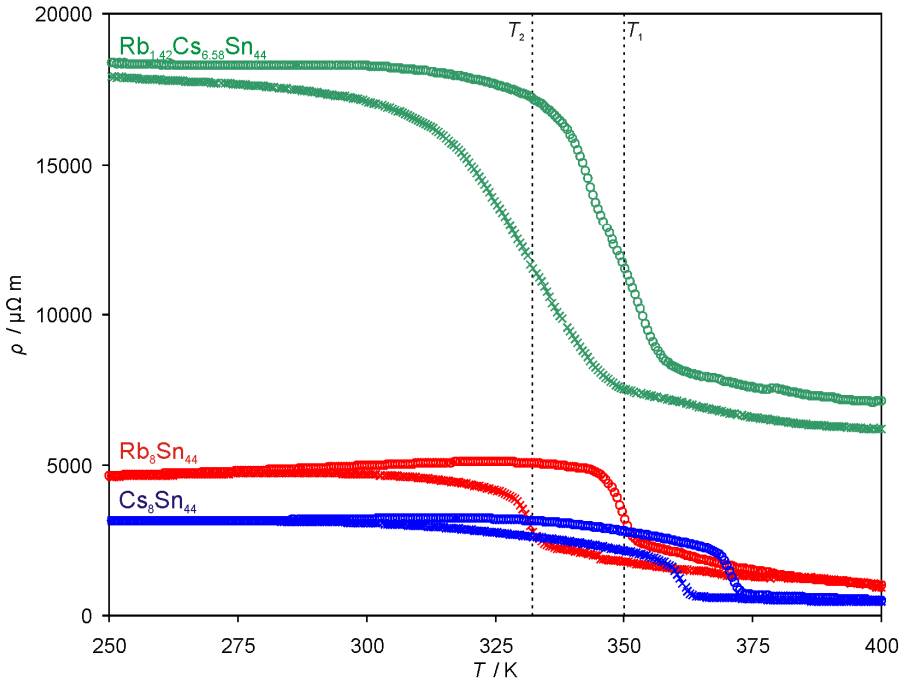

Figure 4.4 Electrical resistivity for single crystals of Rb_8Sn_{44}, $Rb_{1.42}Cs_{6.58}Sn_{44}$ and Cs_8Sn_{44} in the temperature range 250 - 400 K. The dashed lines indicate the reversal points of the heating (open circles) and cooling (×) sequences.

4.5 Thermoelectric properties

Transport measurements were carried out on Rb_8Sn_{44}. The sample was compacted to a 3.45 mm high cylinder with a diameter of 8.30 mm. A rod with dimensions 6.4 × 2.8 × 2.1 mm^3 was cut from the disk. The density was measured to be 5.12 g cm^{-3} using an immersion technique, which corresponds to 92% of the theoretical X-ray density. Unfortunately, the hot pressing with the SPS technique caused partial decomposition of

the clathrate. According to the Rietveld refinement of the powder diffractogram after the thermoelectric measurements, the pressed sample contained 8.6(2)% *β*-Sn (Figure 4.5).

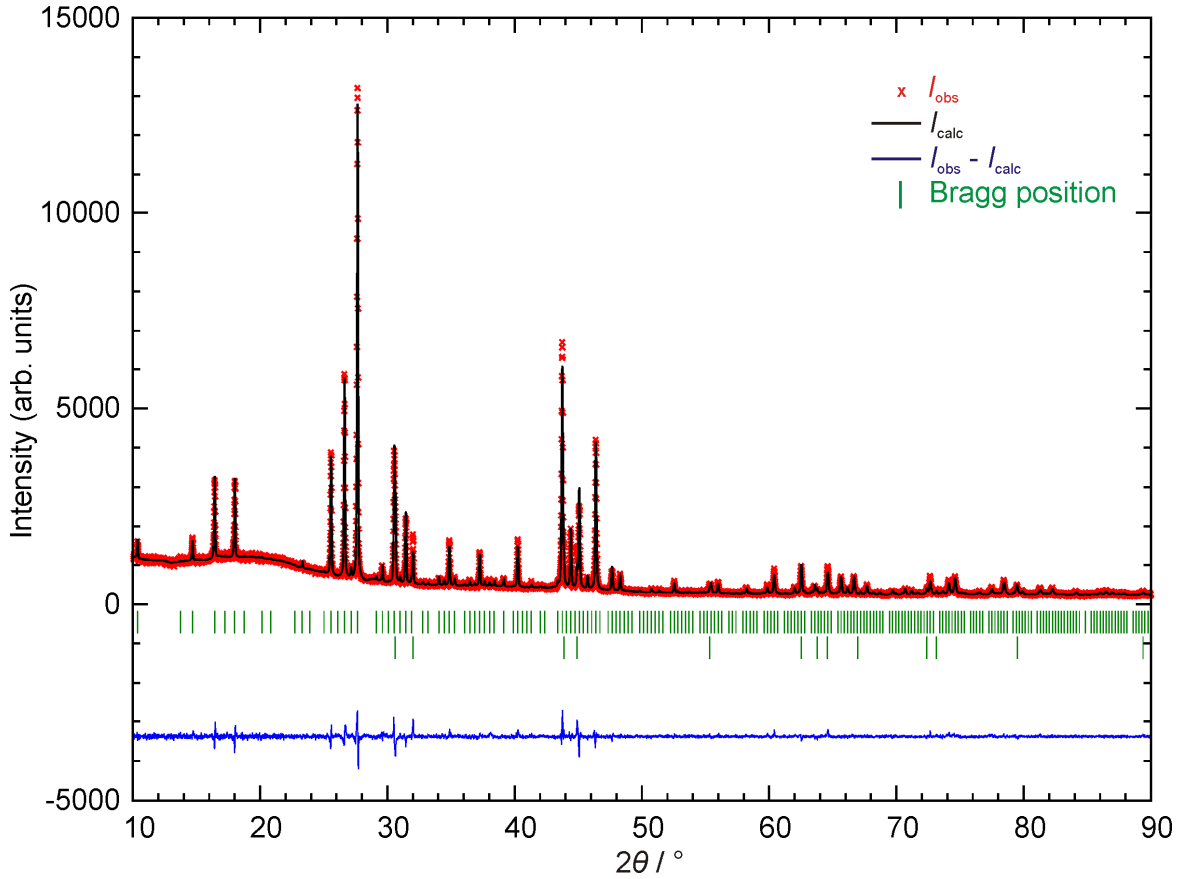

Figure 4.5 Rietveld refinement of the powder diffraction data for *α*-Rb_8Sn_{44} obtained after the SPS pressing for the thermoelectric measurements. The lower row of Bragg reflections refers to the secondary *β*-Sn phase.

The thermoelectric properties revealed significant changes at 353 K coinciding with the structural phase transition. Figure 4.6 shows the electrical resistivity (ρ) and the thermopower (S) and discontinuities in both properties are evident at the phase transition. In the temperature range 4 - 350 K, ρ and S are characteristic of a metallic system. The moderate valued S decreases linearly whereas ρ increases with increasing T. At the phase transition there is a remarkable increase in the absolute value of the Seebeck coefficient. Extrapolating the values for the ordered phase to 395 K yields a hypothetical value of $S_{\alpha\text{-form}}(395\ K) = -10.1\ \mu V\ K^{-1}$. This denotes an increase by a factor of 4 compared to the actual value of the disordered phase at that temperature, $S(395\ K) = -42.8\ \mu V\ K^{-1}$.

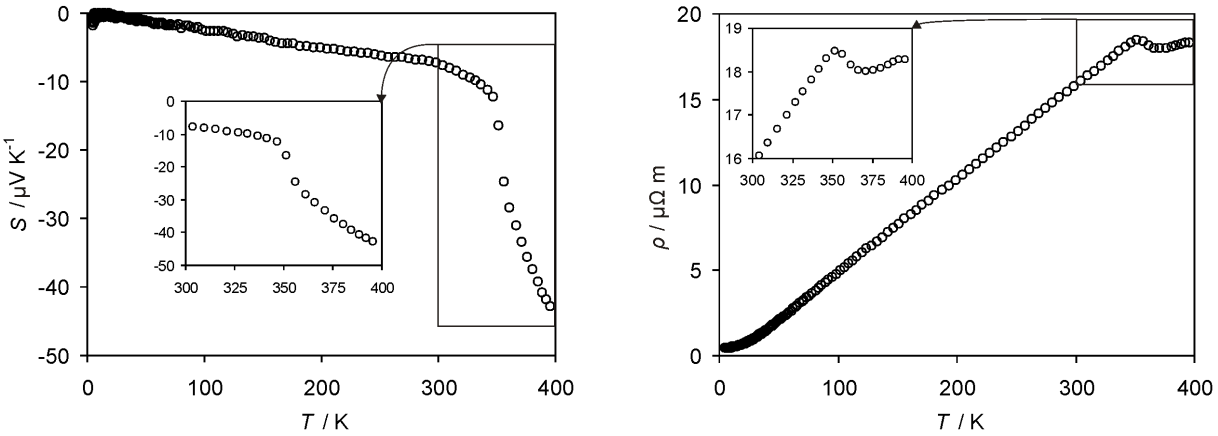

Figure 4.6 Seebeck coefficient (left) and electrical resistivity (right) for a pressed pellet of Rb_8Sn_{44}. The insets zoom in the phase-transition temperature. Values below 3.8 K have been removed due to a small superconducting Sn impurity.

The increased disorder induced by the phase transition does not affect the thermal conductivity (κ_{tot}). This is evident in Figure 4.7, where the κ_{tot} of the sample is plotted as a function of T. The subtracted electronic contribution (κ_e) was estimated using the Wiedemann-Franz law:

$$\kappa_e = \frac{L\,T}{\rho}$$

where L = 2.44 10^{-8} W Ω K^{-2}. Above 200 K the thermal radiation becomes significant and the data above this temperature must be corrected to be quantitative. However, since the thermal radiation correction is a smoothly varying function, it cannot hide a possible discontinuity in the thermal conductivity.

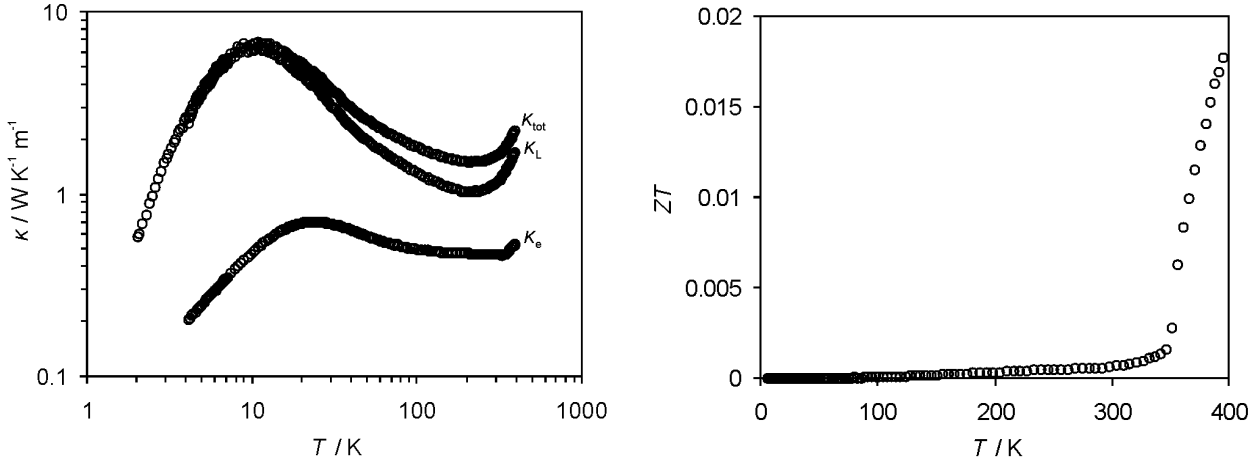

Figure 4.7 Thermal conductivity in logarithmic scale (left) and thermoelectric FOM (right) for a pressed pellet of Rb_8Sn_{44}. Values below 3.8 K have been removed due to a small superconducting Sn impurity.

The transport properties of Rb_8Sn_{44} are summarized in Table 4.2. The lattice thermal conductivity (κ_L) is estimated at 200 K. The remaining quantities are evaluated at 300 K.

The effective mass (m^*) is estimated using the thermopower (S) and the Hall charge carrier concentration (n_H) assuming a single parabolic band dominated by acoustic phonon scattering. The Hall mobility (μ_H) is estimated using n_H and the resistivity (ρ). As for the overall figure of merit (ZT), the sample shows rather low thermoelectric efficiency up to 350 K. Noteworthy, the room-temperature value of $\rho(Rb_8Sn_{44})$ for the pressed sample is about 300 times smaller than for the measurement on the single crystal due to the β-Sn admixture. Over the transition temperature ZT increases almost by a factor of 10 and reaches the value of 0.0018 at 400 K, which is still much lower than the currently most efficient thermoelectric clathrates (Chapter 1.5).

Table 4.2 Experimental transport data for Rb_8Sn_{44} at 300 K.

κ_L / W m^{-1} K^{-1}	S / μV K^{-1}	ρ / μΩ m	n_H / e uc^{-1}	μ_H / cm^2 V^{-1} s^{-1}	m^*/m_e
1.02(2)	–7.34(5)	15.896(4)	14.0(5)	0.49(2)	1.32(4)

4.6 Neutron time-of-flight scattering

The phonon density-of-states (PDOS) for Rb_8Sn_{44} and Cs_8Sn_{44} were determined experimentally by time-of-flight neutron scattering. Multi-temperature measurements were performed on powdered samples of approximately 8 g each. The samples were placed in Al containers under Ar atmosphere and were irradiated for about 4 hours at each temperature step. General parameters and background corrections were set by using a suitable V standard. Figure 4.8 shows the generalized PDOS for A_8Sn_{44} (A = Rb, Cs) at various temperatures.

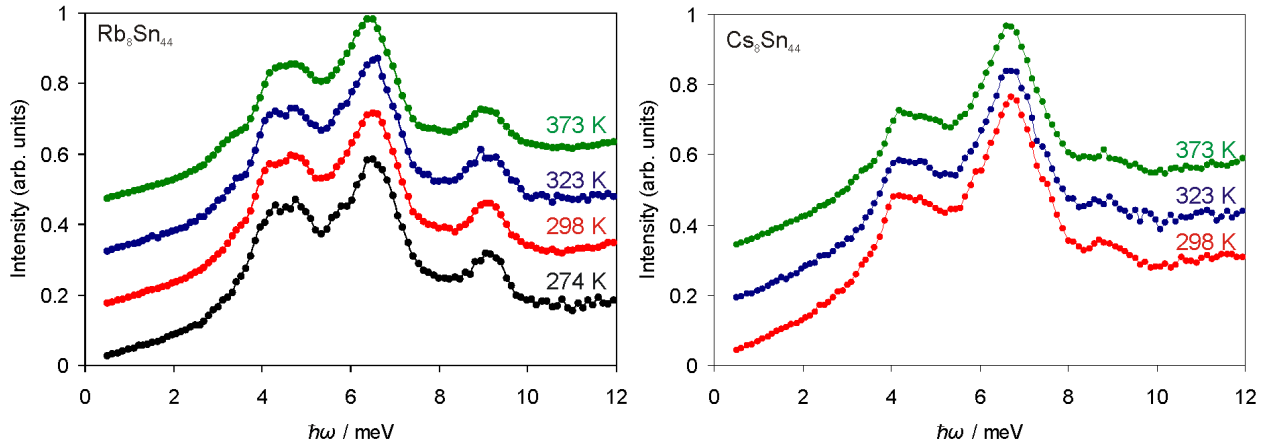

Figure 4.8 Generalized phonon density-of-states for Rb_8Sn_{44} and Cs_8Sn_{44}. The temperatures have been Bose-Einstein corrected.

As expected, the PDOS of the two clathrates are similar and only small shifts are found due to different mass of the alkali metals. The strongest peaks are observed between 6.2 - 6.8 meV which correspond to Sn vibrations in the crystal lattice as well as the Raman shifts at 50 - 55 cm^{-1}. Vacancy-induced bands are found in this case around 9 meV for Rb_8Sn_{44} and 8.5 meV for Cs_8Sn_{44}. The data reveal also a small effect of the phase transition on the PDOS and more specifically on the rattling vibrations of the alkali metals that reside in both types of framework cavities. An intensity increase is observed for Rb_8Sn_{44} at 3.2 meV whereas in Cs_8Sn_{44} the effect much weaker. This change was not observed in the multi-temperature Raman spectra of Rb_8Sn_{44} (Chapter 3.6).

4.7 Discussion

Many cases of clathrate compounds are known that undergo temperature- or pressure- induced structural transformations and alternate their physical properties: a) a magnetocaloric effect was reported for the doped $Eu_8Ga_{16}Ge_{30}$ due to the ferromagnetic transition from the type-I to type-VIII structure,[8,9] b) the type-IX clathrate Ba_6Ge_{25}[10,11] tunes its electrical properties through a two-step phase transition related with ordering of the Ba atoms in the framework cavities, c) the defect-free type-I K_8Si_{46} changes drastically its phonon band structures upon pressing[12] and d) the fully ordered Ba_8Ge_{43} exhibits unexpected semiconducting behavior.[13]

The phase transition in A_8Sn_{44} significantly influences the charge-carrier properties. Electrical resistivity measurements on single crystals of Rb_8Sn_{44} and $Rb_{1.42}Cs_{6.58}Sn_{44}$ indicated that the lower ordering of the defects in the solid increases significantly the flow of electric current. The effect is also completely reserved by cooling the crystals to room temperature. Furthermore, the thermopower of Rb_8Sn_{44} changes rapidly over the transition temperature. However, the pressed sample contained some *β*-Sn admixture and therefore a comparison of the thermoelectric efficiency to other materials is not possible. The enhancement of the charge-carrier properties in the *β*-modification may be caused by the alternation of the concentration of vacancies in the domains of the solid.

Figure 4.9(a) depicts a qualitative band structure for the hypothetical guest-free Sn_{46}. Disregarding core electron states, and considering only the sp^3 states, four bonding and four antibonding states are found per atom. This yields a total of 184 states in both valence and conduction band. With each Sn atom contributing four valence electrons the hypothetical Sn_{46} compound is expected to be a perfect semiconductor. This was also

predicted in a theoretical work where the minimum band gap was calculated to be 0.855 eV.[3] The introduction of vacancies significantly alters the band structure. Charge compensation is realized by introducing A atoms in the framework cages hence the 184 valence electrons persist. Atoms neighboring vacancies have lone-pair electrons. Due to their nonbonding nature, these states are expected within the band gap. In the ordered phase significant hybridization between these states can be expected and hence bands of dangling-bond states are formed. These bands are energetically placed within the band gap. This has been proved for the clathrate-IX K_6Sn_{25}.[14,15] Moreover, a theoretical study for Cs_8Sn_{44} did indeed show dangling bonds forming within the band gap (Figure 4.9(b)).[3]

The scenarios of dangling bond bands overlapping each other and/or the conduction band are qualitatively depicted in Figure 4.9(c) and (d). In such cases even metallic properties are expected. A linear field dependence was found for $\rho_H(B)$ at all temperatures. Low mobility is expected for charge carriers in dangling bond bands. In the disordered phase less hybridization between dangling bonds can be expected. Thus a possible explanation is that a band structure qualitatively similar to the one calculated by Myles et al. emerges (Figure 4.9(b)).[3] From a purely kinetic viewpoint, decreased mobility and hence higher resistivity is expected in the disordered phase. However, since the mobility is already extremely low in the ordered phase a further decrease is unlikely.

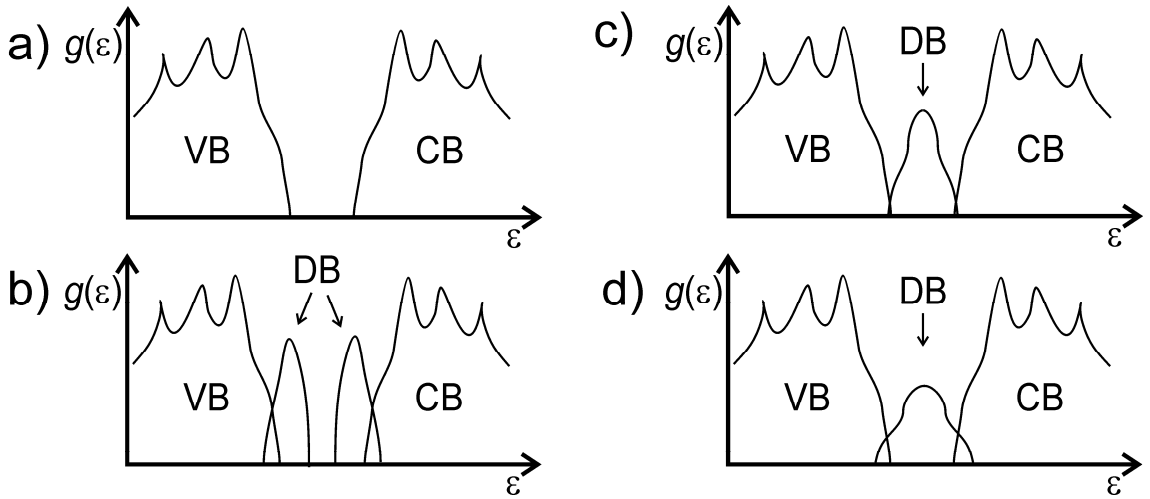

Figure 4.9 Qualitative band structure representations for different scenarios in type-I $A_{8-x}Sn_{46-y}$: a) a guest-free Sn_{46} model, b), c) and d) various possibilities for the vacancy containing clathrate A_8Sn_{44}. The term VB refers to the valence band, CB to the conduction band and DB to the dangling bands.

On the other hand, the magnetic properties, thermal conductivity and phonon density of states of the clathrates are virtually unaffected by the structural transformation. In the low-temperature modification, the two vacancies are distributed in three out of 46 framework positions, whereas in high-temperature modification in six out of 46 positions. Thus, even in the ordered phase there is a high density of scattering centers. Two scenarios are possible. Either: a) another mechanism is responsible for the major part of the phonon scattering, e.g. resonant scattering by the Rb guest atoms or b) the density of scattering centers is sufficiently large in the ordered phase and further disorder will not increase the phonon scattering. A minimum scattering length of ~2 Å is expected for the phonons and this is achievable even with the density of scattering centers in the *β*-phase.

4.8 References

[1] J. M. Ziman *Electrons and Phonons. The Theory of Transport Phenomena in Solids*, Claredon Press, Oxford, U.K., **2001**.

[2] L. Mollnitz, N. Blake, H. Metiu *J. Chem. Phys.* **2002**, *117*, 1302.

[3] C. Myles, J. Dong, O. Sankey *Phys. Rev. B* **2001**, *64*, 165202.

[4] M. Christensen, N. Lock, J. Overgaard, B. Iversen *J. Am. Chem. Soc.* **2006**, *128*, 15657.

[5] A. Bentien, M. Christensen, J. D. Bryan, A. Sanchez, S. Paschen, F. Steglich, G. D. Stucky, B. Iversen *Phys. Rev. B* **2004**, *69*, 045107.

[6] J. L. Cohn, G. S. Nolas, V. Fessatidis, T. H. Metcalf, G. A. Slack *Phys. Rev. Lett.* **1999**, *82*, 779.

[7] M. Baitinger *Ph.D. Thesis*, T.U. Darmstadt **2000**.

[8] S. Srinath, J. Gass, D. J. Rebar, G. T. Woods, H. Srikanth, G. Nolas *J. Appl. Phys.* **2006**, *99*, 08K902(3).

[9] S. Paschen, W. Carrillo-Carbera, A. Bentien, V. H. Tran, M. Baenitz, Yu. Grin, F. Steglich *Phys. Rev. B* **2001**, *64*, 214404(11).

[10] H. Q. Yuan, F. M. Grosche, W. Carrillo-Carbera, V. Pacheco, G. Sparn, M. Baenitz, U. Schwarz, Yu. Grin, F. Steglich *Phys. Rev. B* **2004**, *70*, 174512(6).

[11] S. Paschen, V. H. Tran, M. Baenitz, W. Carrillo-Carbera, Yu. Grin, F. Steglich *Phys. Rev. B* **2002**, *65*, 134435(9).

[12] J. S. Tse, S. Desgreniers, Z. Li, M. R. Ferguson, Y. Kawazoe *Phys. Rev. Lett.* **2002**, *89*, 195507(4).

[13] N. L. Okamoto, M. W. Oh, T. Nishii, K. Tanaka, H. Inui *J. Appl. Phys.* **2006**, *99*, 033513.

[14] T. F. Fässler, C. Kronseder *Z. Anorg. Allg. Chem.* **1998**, *624*, 561.

[15] T. F. Fässler *Z. Anorg. Allg. Chem.* **1998**, *624*, 569.

5. Mercury substituted type-I clathrates $A_8Hg_4Sn_{42}$ (A = K, Rb, Cs)

5.1 Introduction

As already mentioned in Chapter 1.4, the interest in clathrate compounds has focused lately on ternary and quaternary systems where the use of different elements as substituents may result in a variety of new compounds. Usually, the Tt framework in type-I or type-II clathrates is substituted by Tr elements or late transition metals (see also Figure 1.5). Over the last decade, many reports regarding physical properties came to the front and in contrast to the binary clathrates, some of their ternary analogues, e.g. $Sr_8Ga_{16}Ge_{30}$,[1,2] $Ba_8Ga_{16}Ge_{30}$[3] and $Ba_8Ga_{16}Sn_{30}$[4] can reach relatively high thermoelectric figure of merit at ambient conditions. It is well established that even subtle alternations in the composition of the framework may affect significantly the electron and phonon bands and ultimately the electrical and thermal conductivity of the materials.[5,6]

From the chemical point of view, the stereoselectivity of the doping is predominantly controlled by the electronegativity of the elements. Since the 6*c* site of the type-I clathrates (space group $Pm\bar{3}n$) possesses the lower electron density among the framework sites, the more electropositive triel elements or transition metals will first occupy this position (Table 5.1). With increasing dopant content, the substitution occurs also in the 16*i* sites. In heavily doped systems like $Ba_8[Ga_{16}Ge_{30}]$[3] the crystallographic studies show mixed occupancy for all three framework sites and the SOFs depend only slightly on the preparation conditions. The only exception from this general subsititution trend is $K_7[B_7Si_{39}]$[7] where the dopant atoms occupy preferably the 16*i* site.

Table 5.1 Substitution sites in ternary type-I clathrates $G_8[M_xTt_{46-x}]$ (space group $Pm\bar{3}n$).

Substitution site of M	Example
6*c*	$Ba_8[Mn_2Ge_{44}]$[8]
	$Cs_8[Zn_4Sn_{42}]$[9]
	$Ba_8[Cu_6Ge_{40}]$[10]
6*c* and 16*i*	$Ba_8[Cd_8Ge_{38}]$[11]
6*c*, 16*i* and 24*k*	$Ba_8[Ga_{16}Ge_{30}]$[3]
	$K_8[Al_{23}Si_{23}]$[12]
16*i*	$K_7[B_7Si_{39}]$[13]

5.2 Synthesis

Stoichiometric mixtures of the reagents with total mass of 1.0 - 1.5 g were loaded in Nb ampoules. Precautions were taken to prevent the evaporation of Hg while weld-sealing the ampoules. The mixtures were heated in a rate of 2 K min^{-1} to 823 K, held at this temperature for 24 hours, then annealed at 673 K for $K_8Hg_4Sn_{42}$ or 723 K for $Rb_8Hg_4Sn_{42}$ and $Cs_8Hg_4Sn_{42}$ for 10 days and subsequently cooled down to room temperature in a rate of –3 K min^{-1}. Moderately air-stable, metal-like crystals of the corresponding clathrates were extracted from the reaction mixtures.

5.3 Crystal structure determination

5.3.1 Powder X-ray diffraction

The clathrates decompose upon extended exposure to O_2 towards formation of SnO_2 on the surface of the crystallites, as indicated by SEM pictures and XPRD. Therefore, the samples were better kept in inert atmosphere. The reaction products contained small amounts of the amalgam $HgSn_9$.[14] This admixture, like $A_8Hg_4Sn_{42}$ (A = K, Rb, Cs), was insoluble in H_2O and could not be removed from the reaction products. The yield of the ternary clathrates follows the descending order Cs > Rb > K. For $K_8Hg_4Sn_{42}$ significant amounts of $HgSn_9$ as well as *β*-Sn and the type-IX clathrate $K_{8-x}Sn_{25}$[15] were detected by X-ray powder diffraction. In contrast to the $Rb_8Hg_4Sn_{42}$ and $Cs_8Hg_4Sn_{42}$ samples (Figures 5.1 and 5.2), the XRPD pattern of $K_8Hg_4Sn_{42}$ was not adequate for Rietveld analysis due to relatively low crystallinity. In the following refinements, the Hg : Sn ratio was set to the standard value of 0.667 : 0.333 that corresponds to the overall composition $A_8Hg_4Sn_{42}$.

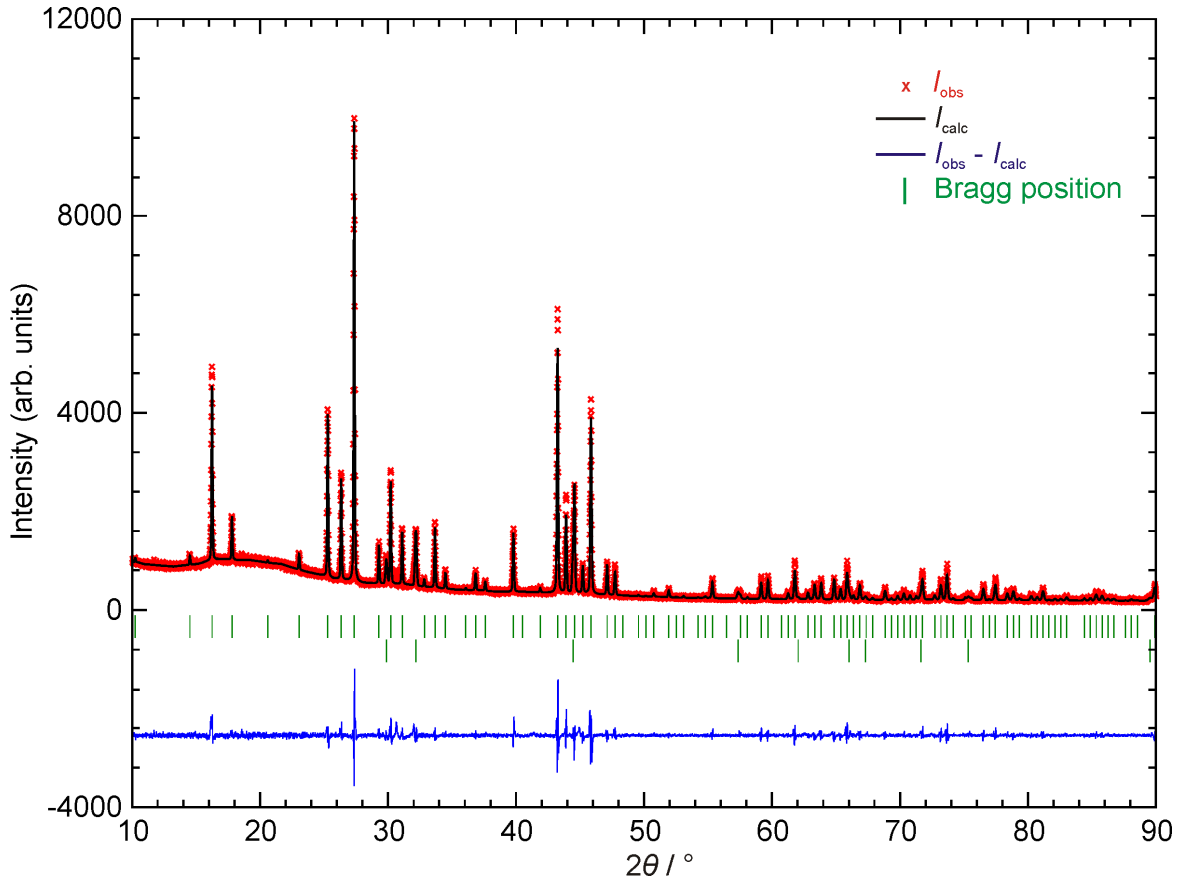

Figure 5.1 Rietveld refinement of powder diffraction data for $Rb_8Hg_4Sn_{42}$ obtained at room temperature in transmission mode. The lower row of Bragg positions refers to $HgSn_9$. Phase distribution: $Rb_8Hg_4Sn_{42}$ 90.7% and $HgSn_9$ 9.3%.

Table 5.2 Atomic coordinates and isotropic displacement parameters for $Rb_8Hg_4Sn_{42}$ (space group $Pm\bar{3}n$, a = 12.1894(1) Å, R_{Bragg} = 0.055, χ^2 = 3.18).

Atom	Site	*x*	*y*	*z*	SOF	U_{iso} / Å^2
Rb1	2*a*	0	0	0	1	0.017(4)
Rb2	6*d*	0.25	0.5	0	1	0.061(3)
Hg/Sn1	6*c*	0.5	0.25	0	0.667/0.333	0.01
Sn2	16*i*	0.1825(1)	0.1825(1)	0.1825(1)	1	0.01
Sn3	24*k*	0.3109(2)	0.1182(1)	0	1	0.01

Table 5.3 Atomic coordinates and isotropic displacement parameters for $HgSn_9$ (space group *P*6/*mmm*, a = 3.21032(1) Å, c = 2.98943(1) Å, R_{Bragg} = 0.053).

Atom	Site	*x*	*y*	*z*	SOF	U_{iso} / Å^2
Hg/Sn1	1*a*	0	0	0	0.1/0.9	0.01

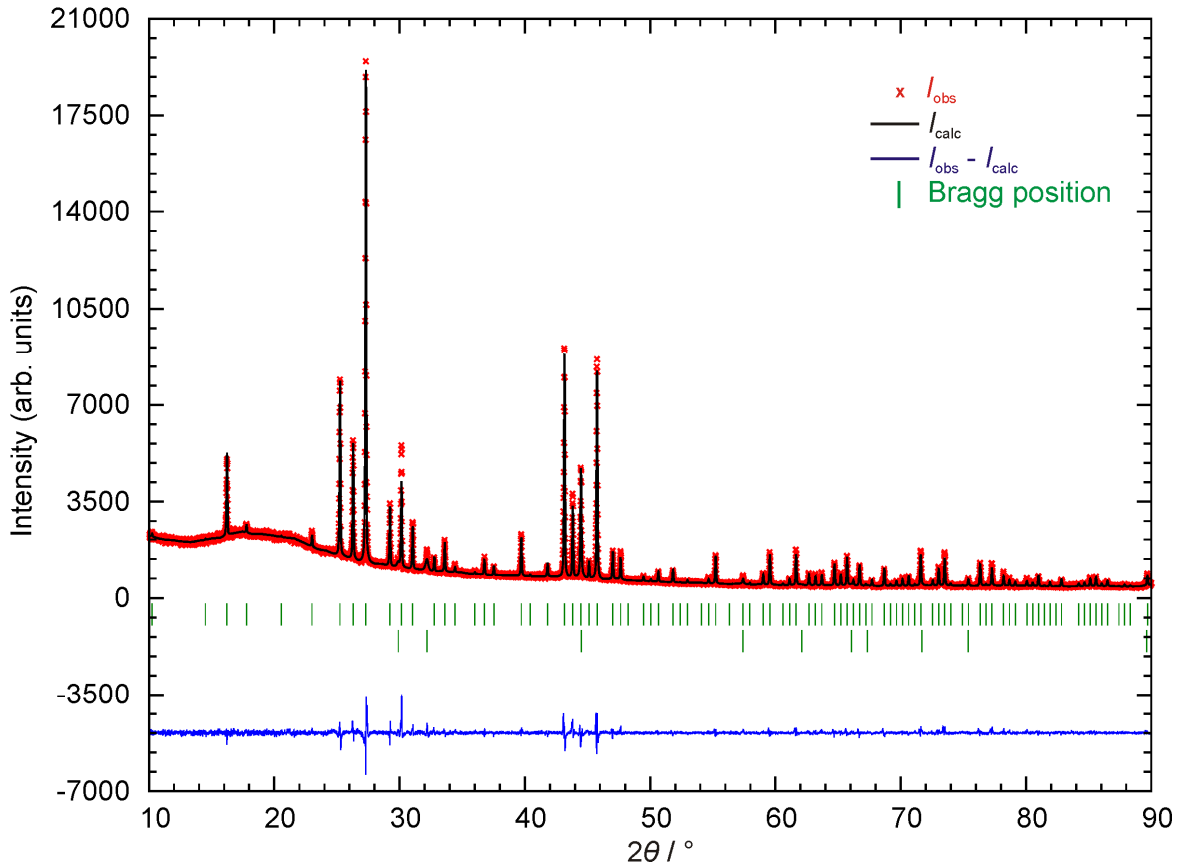

Figure 5.2 Rietveld refinement of powder diffraction data for $Cs_8Hg_4Sn_{42}$ obtained at room temperature in transmission mode. The lower row of Bragg positions refers to $HgSn_9$. Phase distribution: $Cs_8Hg_4Sn_{42}$ 94.8% and $HgSn_9$ 5.2%.

Table 5.4 Atomic coordinates and isotropic displacement parameters for $Cs_8Hg_4Sn_{42}$ (space group $Pm\bar{3}n$, a = 12.2121(4) Å, R_{Bragg} = 0.040, χ^2 = 3.20).

Atom	Site	*x*	*y*	*z*	SOF	U_{iso} / Å^2
Cs1	2*a*	0	0	0	1	0.00527(4)
Cs2	6*d*	0.25	0.5	0	1	0.01206(4)
Hg/Sn1	6*c*	0.5	0.25	0	0.667/0.333	0.00541(7)
Sn2	16*i*	0.1836(3)	0.1836(3)	0.1836(3)	1	0.00313(2)
Sn3	24*k*	0.3116(5)	0.1182(4)	0	1	0.00465(2)

Table 5.5 Atomic coordinates and isotropic displacement parameters for $HgSn_9$ (space group *P*6/*mmm*, a = 3.2086(1) Å, c = 2.9865(1) Å, R_{Bragg} = 0.031).

Atom	Site	*x*	*y*	*z*	SOF	U_{iso} / Å^2
Hg/Sn1	1*a*	0	0	0	0.1/0.9	0.01

5.3.2 Single-crystal X-ray diffraction

Good quality single crystals of $A_8Hg_4Sn_{42}$ (A = K, Rb, Cs) were mounted on the Oxford Xcalibur3 diffractometer for full data collections at room temperature. Three series of 138 frames were recorded with exposure times of 30 sec and a crystal-detector distance of 50 mm. The reflections were corrected for absorption (multi scan) using the program CrysAlis RED (Oxford Diffraction Ltd). Systematic absence conditions were consistent with the space group $Pm\bar{3}n$. Relevant crystallographic and refinement data are listed in Table 5.6.

Table 5.6 Crystallographic data and refinement parameters for $A_8Hg_4Sn_{42}$ (A = K, Rb, Cs).

Chemical formula	$K_8Hg_4Sn_{42}$	$Rb_8Hg_4Sn_{42}$	$Cs_8Hg_4Sn_{42}$
Space group (No.)	$Pm\bar{3}n$ (223)	$Pm\bar{3}n$ (223)	$Pm\bar{3}n$ (223)
Formula weight	6100.14	6471.10	6850.62
Temperature, T / K	293	293	293
Diffractometer	Oxford Xcalibur3	Oxford Xcalibur3	Oxford Xcalibur3
Radiation, λ / Å	Mo-Kα, 0.71073	Mo-Kα, 0.71073	Mo-Kα, 0.71073
Z	1	1	1
a / Å	12.1255(4)	12.1838(4)	12.2130(4)
V / Å^3	1782.8(1)	1808.6(1)	1821.7(1)
$\rho_{calc.}$ / g cm^{-3}	5.682	5.941	6.245
Absorp. coeff., μ / mm^{-1}	23.44	27.99	26.42
F(000)	2572	2716	2860
θ range for data collection / °	3.36 - 25.39	3.34 - 25.26	3.34 - 25.19
Index ranges	–14 ≤ h ≤ 14, –14 ≤ k ≤ 14, –14 ≤ l ≤ 8	–14 ≤ h ≤ 14, –14 ≤ k ≤ 14, –6 ≤ l ≤ 14	–13 ≤ h ≤ 14, –14 ≤ k ≤ 12, –14 ≤ l ≤ 12
Reflections collected	10422	10588	10592
Independent reflections	323 (R_{int} = 0.064)	323 (R_{int} = 0.032)	323 (R_{int} = 0.031)
Parameters	16	16	16
Goodness-of-fit on F^2	1.337	1.178	1.339
Weighting parameters	a = 0.0217, b = 12.63	a = 0.0190, b = 19.46	a = 0.0110, b = 19.04
Final R indices (I > 2σ(I))	R_1 = 0.019, wR_2 = 0.051	R_1 = 0.017, wR_2 = 0.043	R_1 = 0.017, wR_2 = 0.038
R indices (all data)	R_1 = 0.020, wR_2 = 0.051	R_1 = 0.018, wR_2 = 0.044	R_1 = 0.018, wR_2 = 0.039
Largest diff. peak and hole / e Å^{-3}	0.8 in 1.3 Å from Sn3 –0.8 in 0.6 Å from Sn3	0.6 in 0.8 Å from Sn3 –1.3 in 0.0 Å from Sn1	0.6 in 1.5 Å from Sn3 –0.9 in 0.2 Å from Sn1

The compounds $A_8Hg_4Sn_{42}$ (A = K, Rb, Cs) adopt the clathrate-I structure (Figure 5.3), where the framework of the Sn atoms is partially substituted by Hg atoms and the guest sites are fully occupied by the alkali metals. The crystallographic sites of the tetrahedrally bonded framework atoms are 6*c*, 16*i* and 24*k* and those of the endohedral guest atoms are 2*a* and 6*d* (Table 5.7). The Hg atoms have a strict preference for the 6*c* site, which is mixed occupied with Sn1. The total occupancy of these sites is constrained during the refinement cycles to unity.

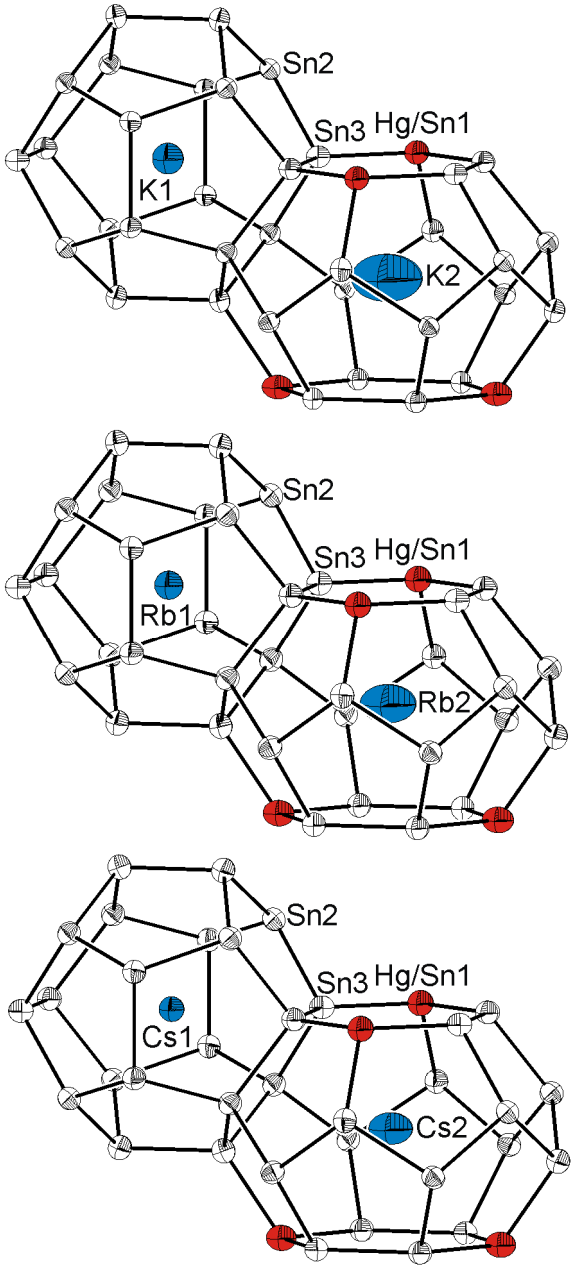

Figure 5.3 Partial view of the crystal structures of $A_8Hg_4Sn_{42}$ (A = K, Rb, Cs) with atom labeling. All thermal ellipsoids are presented at 90% probability. The extent of rattling for the encaged alkali metals in the tkad follows the order K > Rb > Cs.

The mixed-occupied 6*c* sites are distributed along a 4_2 screw axis that runs through the centres of the hexagonal faces and the centres of the tetrakaidecahedra. As a result, the compounds contain no Hg-Hg bonds. Possible superstructure reflections indicating lowering of the symmetry due to the ordering of Hg in the substituted position were observed neither in powder nor in the single-crystal diffraction patterns, measured even at 130 K.

Table 5.7 Atomic coordinates and equivalent isotropic ADPs for $A_8Hg_4Sn_{42}$ (A = K, Rb, Cs).

Atom	Site	*x*	*y*	*z*	SOF	U_{eq} / Å^2
			$K_8Hg_4Sn_{42}$			
K1	2*a*	0	0	0	1	0.027(2)
K2	6*d*	0.25	0.5	0	1	0.118(4)
Hg/Sn1	6*c*	0.5	0.25	0	0.667/0.333	0.0200(3)
Sn2	16*i*	0.18286(3)	0.18286(3)	0.18286(3)	1	0.0123(3)
Sn3	24*k*	0.31161(4)	0.11758(4)	0	1	0.0136(3)
			$Rb_8Hg_4Sn_{42}$			
Rb1	2*a*	0	0	0	1	0.0222(7)
Rb2	6*d*	0.25	0.5	0	1	0.0730(9)
Hg/Sn1	6*c*	0.5	0.25	0	0.667/0.333	0.0215(3)
Sn2	16*i*	0.18309(3)	0.18309(3)	0.18309(3)	1	0.0148(2)
Sn3	24*k*	0.31132(4)	0.11777(4)	0	1	0.0154(2)
			$Cs_8Hg_4Sn_{42}$			
Cs1	2*a*	0	0	0	1	0.0173(4)
Cs2	6*d*	0.25	0.5	0	1	0.0463(4)
Hg/Sn1	6*c*	0.5	0.25	0	0.667/0.333	0.0227(3)
Sn2	16*i*	0.18335(3)	0.18335(3)	0.18335(3)	1	0.0147(2)
Sn3	24*k*	0.31108(5)	0.11811(5)	0	1	0.0155(2)

As shown in Table 5.8, the Sn-Sn bond lengths range from 2.8201(5) Å to 2.8514(7) Å, 2.8240(5) Å to 2.8695(7) Å, and 2.8198(5) Å to 2.8850(9) Å for M = K, Rb and Cs, respectively. The longest distance in all cases is found for the Sn3-Sn3 contact (site 24*k*). Similar Sn-Sn distances have also been observed in $Cs_8Zn_4Sn_{42}$ (2.810(4)-2.880(4) Å).[9] The shortest bond length is observed for Hg/Sn1-Sn3 with 2.7922(3), 2.8072(6) and 2.8139(4) Å for A = K, Rb and Cs, respectively. Due to the larger atomic size of Hg, a distance increase with respect to homoatomic Sn-Sn contacts is expected. In fact, these distances are found here to be even shorter than the sum of covalent radii of Sn and Hg (1.40 Å + 1.50 Å = 2.90 Å). However, shorter Hg-Sn contacts with respect to normal Sn-Sn contacts are also observed in other intermetallic systems such as

BaHgSn[16] (*d*(Hg-Sn) = 2.8068 Å and 2.8072(3) Å) and in the molecule [MeSi{$SiMe_2N$(*p*-Tol)}$_3$Sn]$_2$M with M = Zn, Cd and Hg.[17] In the latter case, the M-Sn bond lengths are crystallographically determined as 2.5782(4) Å, 2.6758(1) Å, 2.6495(2) Å for Zn, Cd and Hg, respectively and the very slight decrease from Cd to Hg is attributed to the relativistic contraction of the 6*s* valence shell.

Table 5.8 Interatomic distances for $A_8Hg_4Sn_{42}$ (A = K, Rb, Cs).

$K_8Hg_4Sn_{42}$		$Rb_8Hg_4Sn_{42}$		$Cs_8Hg_4Sn_{42}$	
Atomic pairs	*d* / Å	Atomic pairs	*d* / Å	Atomic pairs	*d* / Å
Hg/Sn1 -Sn3	2.7922(3) 4×	Hg/Sn1-Sn3	2.8072(6) 4×	Hg/Sn1-Sn3	2.8139(4) 4×
Sn2 -Sn2	2.8201(5)	Sn2-Sn2	2.8240(5)	Sn2-Sn2	2.8198(5)
-Sn3	2.8249(6) 3×	-Sn3	2.8373(5) 3×	-Sn3	2.8430(7) 3×
Sn3 -Sn3	2.8514(7)	Sn3-Sn3	2.8695(7)	Sn3-Sn3	2.8850(9)
K1 -Sn2	3.8404(4) 8×	Rb1-Sn2	3.8637(4) 8×	Cs1-Sn2	3.8785(4) 8×
-Sn3	4.0385(5) 12×	-Sn3	4.0554(6) 12×	-Sn3	4.0638(6) 12×
K2 -Sn3	4.0546(4) 8×	Rb2-Sn3	4.0769(5) 8×	Cs2-Sn3	4.0898(5) 8×
-Hg/Sn1	4.2870(1) 4×	-Hg/Sn1	4.3076(1) 4×	-Hg/Sn1	4.3179(1) 4×
-Sn2	4.5130(4) 8×	-Sn2	4.5331(4) 8×	-Sn2	4.5423(4) 8×
-Sn3	4.6968(2) 4×	-Sn3	4.7166(2) 4×	-Sn3	4.7233(2) 4×

More generally, it is expected that the Sn-Sn distances in the framework will increase with the increasing size of the guest metal atoms. All bond lengths but one follow this trend; the Sn2-Sn2 length slightly decreases from 2.8240(5) Å in $Rb_8Hg_4Sn_{42}$ to 2.8198(5) Å in $Cs_8Hg_4Sn_{42}$. In all cases, the alkali-metal atoms in the cages are quite distant from the framework atoms and the interaction distances increase with increasing atomic size of the alkali metal. Furthermore, the atomic displacement parameters for the guest alkali metals show isotropic behavior for A1 in the smaller cavity, and anisotropic characteristics for A2 with U_{11} roughly half the value of U_{22} = U_{33} (Table 5.9). The U_{22}(A2):U_{22}(A1) ratio is more than 5 for the A = K phase, close to 4 for A = Rb and more than 3 for A = Cs. Anisotropy is also observed for the Hg/Sn1 site, as the U_{22} parameter that points to the center of the hexagon is significantly larger than U_{11} and U_{33}. One possible explanation is the slightly different electrostatic interaction between Hg or Sn with the alkali-metal atom in the center of the cavity. Since no split model could be applied for this site, the ellipsoids are elongated in the direction of the guest position.

Table 5.9 Anisotropic ADPs for $A_8Hg_4Sn_{42}$ (A = K, Rb, Cs) (in Å^2).

Atom	U_{11}	U_{22}	U_{33}	U_{12}	U_{13}	U_{23}
			$K_8Hg_4Sn_{42}$			
K1	0.027(2)	U_{11}	U_{11}	0	0	0
K2	0.063(5)	0.145(6)	U_{22}	0	0	0
Hg/Sn1	0.0158(3)	0.0285(5)	U_{11}	0	0	0
Sn2	0.0123(3)	U_{11}	U_{11}	–0.0009(1)	U_{12}	U_{12}
Sn3	0.0158(4)	0.0120(3)	0.0131(3)	0.0011(2)	0	0
			$Rb_8Hg_4Sn_{42}$			
Rb1	0.0222(7)	U_{11}	U_{11}	0	0	0
Rb2	0.040(1)	0.089(1)	U_{22}	0	0	0
Hg/Sn1	0.0198(4)	0.0298(5)	U_{11}	0	0	0
Sn2	0.0148(2)	U_{11}	U_{11}	–0.0009(1)	U_{12}	U_{12}
Sn3	0.0170(3)	0.0143(3)	0.0150(3)	0.0006(2)	0	0
			$Cs_8Hg_4Sn_{42}$			
Cs1	0.0173(4)	U_{11}	U_{11}	0	0	0
Cs2	0.0281(8)	0.0554(6)	U_{22}	0	0	0
Hg/Sn1	0.0198(3)	0.0285(5)	U_{11}	0	0	0
Sn2	0.0147(2)	U_{11}	U_{11}	–0.0009(1)	U_{12}	U_{12}
Sn3	0.0168(3)	0.0152(3)	0.0146(3)	0.0007(2)	0	0

The structural refinements of the single-crystal and powder data were also performed by setting the occupation factors of the 6*c* Wyckoff sites as free variables. The results are given in Table 5.10 along with the EDX elemental analysis of the crystals. The single-crystal XRD analysis led to SOF(Hg)/SOF(Sn) values of 0.66/0.34(1), 0.607/0.393(9) and 0.61/0.39(1) for A = K, Rb and Cs, respectively and the compositions $K_8Hg_{3.94}Sn_{42.06(6)}$, $Rb_8Hg_{3.64}Sn_{42.36(5)}$ and $Cs_8Hg_{3.67}Sn_{42.33(6)}$. These values resemble well the results of the corresponding Rietveld analyses. Thus within the standard deviation (3σ range), the A : Hg : Sn ratio is the same and by taking into account the strong correlation effects between ADPs and SOFs in the least-squares refienement, even larger deviations must be assumed. Several X-ray data refinements of different crystals obtained from other reaction stoichiometries like A : Hg : Sn = 8 : 6 : 40 and 8 : 3 : 43 resulted always in the same composition of the main product with deviations on the SOFs less than 0.03(3). Therefore, the composition of all three clathrates can be established as $A_8Hg_4Sn_{42}$.

Table 5.10 Composition of the ternary clathrates $A_8Hg_xSn_{46-x}$ determined by single-crystal and powder X-ray diffraction as well as EDX analysis.

	Single-crystal analysis (x)	Rietveld analysis (x)	EDX analysis (A : Hg : Sn)
$K_8Hg_xSn_{46-x}$	3.94(6)	—	15(2) : 5(2) : 80(5)
$Rb_8Hg_xSn_{46-x}$	3.64(6)	3.5(4)	14(2) : 7(2) : 79(6)
$Cs_8Hg_xSn_{46-x}$	3.67(6)	3.5(4)	12(2) : 7(1) : 81(5)

5.4 Thermal analysis

The DTA diagram of $Rb_8Hg_4Sn_{42}$ is depicted in Figure 5.4. In agreement with the case of $Rb_xCs_{8-x}Sn_{44}$ ($0 \le x \le 8$) (Figure 3.16), the peritectic transformation shows large hysteresis, namely 821 K and 720 K for the melting and the resolidification, respectively. At about 960 K a weak thermal effect is observed. Finally, in the temperature region 455 - 480 K a weak reversible transition is observed, that confirms the existence of a Hg_xSn_{10-x} phase[18] ($x \approx 1$) but no other residues such as *β*-Sn. The cation's size seems to have significant effect on the thermal stability of the clathrates. The melting points of the Hg-substituted clathrates were compared to those of the binary $A_8Sn_{44}\square_2$ (A = K, Rb, Cs) (Table 5.11). For both series, the onsets increase with increasing atomic number of the alkali metals. It is also noteworthy that the Hg-substituted clathrates appear to be significantly more stable than the corresponding defect clathrates.

Table 5.11 Onsets of the melting for the $A_8Sn_{44}\square_2$ and $A_8Hg_4Sn_{42}$ clathrate compounds.

Compound	*T* / K
$K_8Sn_{44}\square_2$	668
$K_8Hg_4Sn_{42}$	719
$Rb_8Sn_{44}\square_2$	784
$Rb_8Hg_4Sn_{42}$	821
$Cs_8Sn_{44}\square_2$	850
$Cs_8Hg_4Sn_{42}$	900

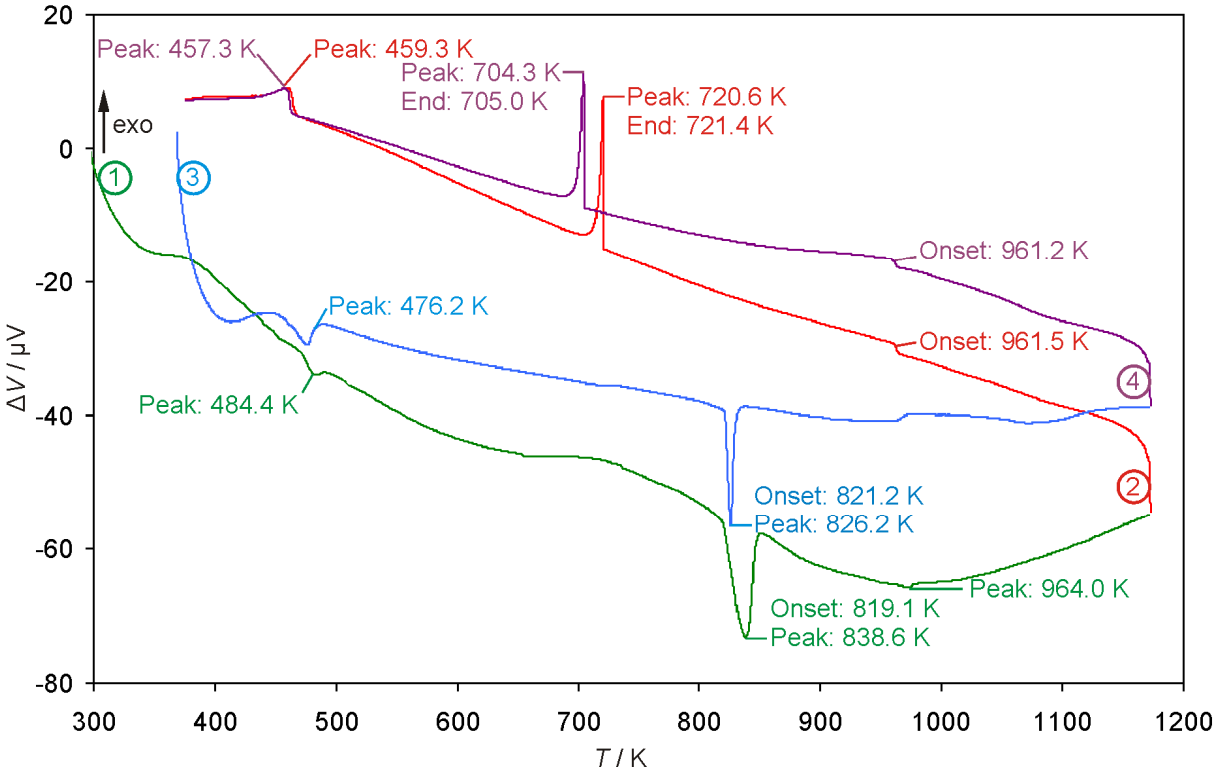

Figure 5.4 DTA diagram for $Rb_8Hg_4Sn_{42}$ in the temperature range 298 - 1173 K with 5 K min^{-1} heating/cooling rate. The numbers ①,②,③ and ④ denote the heating-cooling sequence.

5.5 Raman spectroscopy

The Raman spectrum of $Rb_8Hg_4Sn_{42}$ is depicted in Figure 5.5. The rattling vibrations of the guest atoms occur at 30 cm^{-1} and 39 cm^{-1}. The higher-frequency framework vibrations are found at 50 - 180 cm^{-1}. The most striking difference between the spectra of Rb_8Sn_{44} and $Rb_8Hg_4Sn_{42}$ is the absence of a band around 70 cm^{-1} in the latter. As already mentioned in Chapter 3.6, this band originates from the three-bonded Sn atoms that neighbour on the vacancies. $Rb_8Hg_4Sn_{42}$ has no such vacancies, but Hg-Sn bonds instead, that probably cause the weak peak at 106 cm^{-1}.

The Raman shifts of the Rb atoms in $Rb_8Hg_4Sn_{42}$ are found slightly lower than in Rb_8Sn_{44} (34 cm^{-1} and 40 cm^{-1}). As the chemical environment of Rb in $Rb@(Sn/Hg)_{24}$ is more symmetric than in $Rb@Sn_{22}\square_2$, the strong coupling among the alkali metal and the negatively charged Sn atoms next to the vacancies increases the *k* factor and ultimately the vibrational frequency of the alkali metal in the defect clathrate. This result accords with other reports on guest-free type-I clathrates like $Cs_8Ga_8Sn_{38}$ and $Cs_8Zn_4Sn_{42}$, which show larger ADPs for the Cs atoms in the tkad and lower lattice thermal conductivity than in Cs_8Sn_{44}.[19]

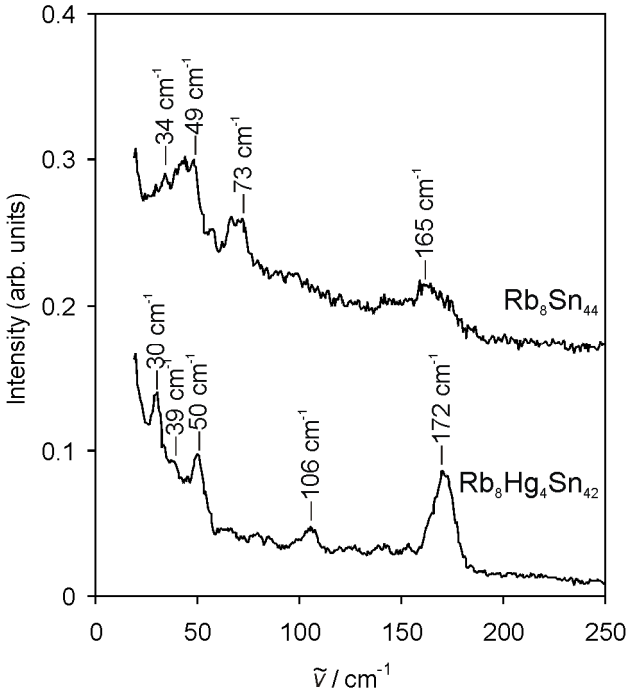

Figure 5.5 Raman spectra of $Rb_8Hg_4Sn_{42}$ and Rb_8Sn_{44} at ambient conditions.

5.6 Magnetic properties

A SQUID measurement was carried out for $Cs_8Hg_4Sn_{42}$ (Figure 5.6). The microcrystalline sample (34.4 mg) was first zero-field cooled to 2 K and checked for superconductivity in a field of 0.01 Tesla. The temperature-independent susceptibility of approximately $\chi = -7\ 10^{-8}$ m^3 mol^{-1} was obtained in the temperature range 100 - 400 K in a field of 2 Tesla (the origin of the spike signals in the temperature range 100 - 250 K is not understood). Such diamagnetic behavior is expected for an electron-precise Zintl phase and has also been observed for A_8Sn_{44} (A = Rb, Cs) in Chapter 4.3. The increase of the magnetic susceptibility at temperatures below 100 K is ascribed to the Curie paramagnetism of $HgSn_9$, which was detected by powder X-Ray diffractometry as secondary phase. Most probably, this admixture also causes the superconducting-magnetic transition at about 4 K (T_c = 3.7 K for β-Sn and T_c = 4.1 K for Hg), when the magnetization was measured in very low field (0.01 Tesla). By subtracting the paramagnetic contributions of the impurity and the diamagnetic core increments of the Hg-substituted clathrate, a weak residual diamagnetism of $\chi(Cs_8Hg_4Sn_{42}) \approx -6\ 10^{-8}$ m^3 mol^{-1} is found.

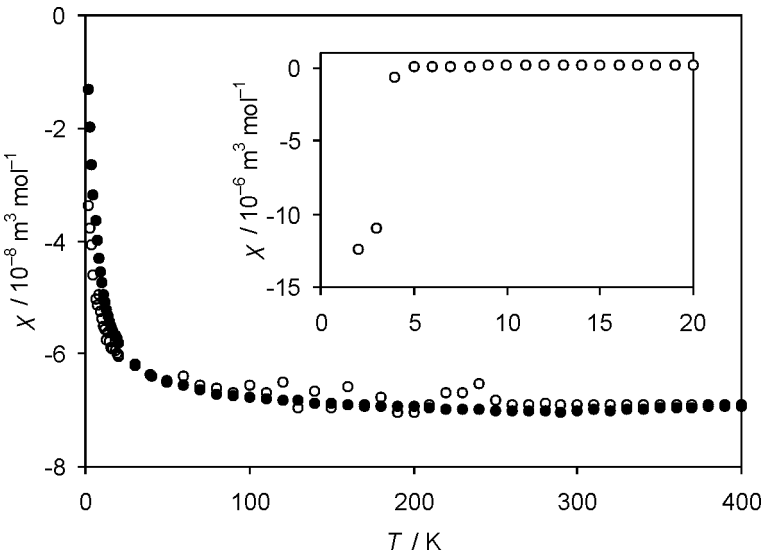

Figure 5.6 Magnetic susceptibility for $Cs_8Hg_4Sn_{42}$ in a field of 2 Tesla. The inset shows the magnetic susceptibility in a field of 0.01 Tesla. Closed circles denote heating steps and open circles cooling steps.

5.7 Discussion

In these first examples of Hg-substituted clathrates, Hg follows the trends of its lighter analogues, namely of M = Zn, Cd in $Cs_8M_4Sn_{42}$.[9,20] Despite the rather unusual tetrahedral coordination, Hg atoms form stable bonds with the Sn atoms, as indicated by the higher thermal stability of $A_8Hg_4Sn_{42}$ compared to $A_8Sn_{44}\square_2$. The encapsulation of large alkali metals, in order to avoid their strong rattling in the cavities, also enhances the overall stability (Figure 5.7). This rationalizes the fact that no type-I Sn clathrates with small guest atoms such as Na, Cu and Ag have been synthesized so far. Moreover, $A_8Hg_4Sn_{42}$ constitute the heaviest members of the rapidly increasing family of semiconducting clathrates doped with group 11 - 13 elements. Therefore, they appear particularly interesting for minimizing the lattice thermal conductivity.

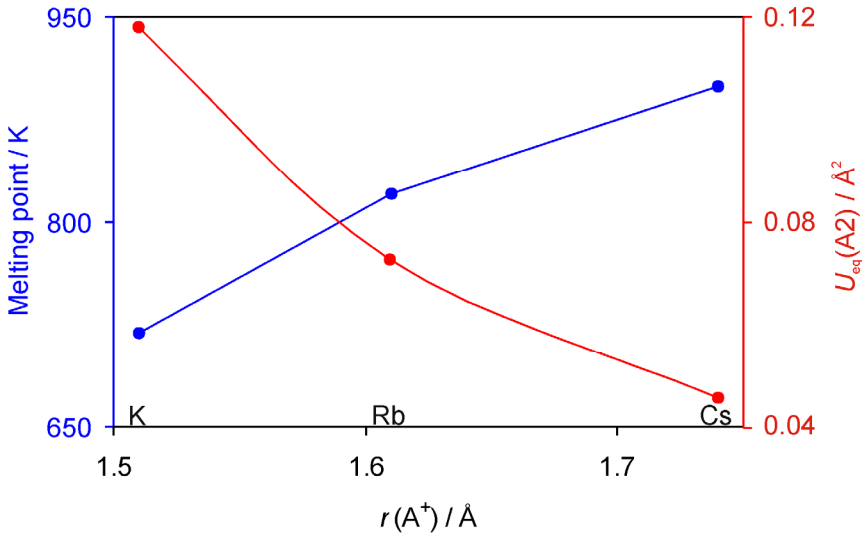

Figure 5.7 Melting point of $A_8Hg_4Sn_{42}$ (A = K, Rb, Cs) and equivalent thermal displacement for the alkali metals in the tkad as a function of the ionic radius (A^+).

Regarding now the electron counting, a neutral framework of 46 Sn atoms per unit cell with exclusively covalently four-bonded Sn atoms requires 46 × 4 = 184 valence electrons. In $A_8Hg_4Sn_{42}$, 42 Sn atoms provide 168 electrons and four Hg atoms 4 × 2 = 8 electrons. Applying the Zintl-Klemm concept, further eight electrons are contributed to the framework bonding by the eight alkali metal atoms, resulting in overall 184 valence electrons. Therefore, the new clathrates are considered as electron-precise Zintl phases. The absence of phase width and the experimentally found diamagnetism for $Cs_8Hg_4Sn_{42}$ are in agreement with this concept.

5.8 References

[1] G. S. Nolas, J. L. Cohn, G. A. Slack, S. B. Schujman *Appl. Phys. Lett.* **1998**, *73*, 178.

[2] N. P. Blake, L. Mollnitz, G. Kresse, H. Metiu *J. Chem. Phys.* **1999**, *111*, 3133.

[3] M. Christensen, N. Lock, J. Overgaard, B. B. Iversen *J. Am. Chem. Soc.* **2006**, *128*, 15657.

[4] M. A. Avila, D. Huo, T. Sakata, K. Suekuni, T. Takabatake *J. Phys. Condens. Matter.* **2006**, *18*, 1585.

[5] J. L. Cohn, G. S. Nolas, V. Fessatidis, T. H. Metcalf, G. A. Slack *Phys. Rev. Lett.* **1999**, *82*, 779.

[6] S. Paschen, M. Baenitz, V. H. Tran, A. Rabis, F. Steglich, W. Carrillo-Cabrera, Yu. Grin, A. M. Strydom, P. de V. du Plessis *J. Phys. Chem. Solids* **2002**, *63*, 1183.

[7] W. Jung, J. Lörincz, R. Ramlau, H. Borrmann, Y. Prots, F. Haarmann, W. Schnelle, U. Burkhardt, M. Baitinger, Yu. Grin *Angew. Chem. Int. Ed.* **2007**, *46*, 6725.

[8] T. Kawaguchi, K. Tanigaki, M. Yasukawa *Appl. Phys. Lett.* **2000**, *77*, 3438.

[9] G. Nolas, T. Weakley, J. L. Cohn *Chem. Mater.* **1999**, *11*, 2470.

[10] S. Johnsen, A. Bentien, G. Madsen, B. Iversen, M. Nygren *Chem. Mater.* **2006**, *18*, 4633.

[11] B. Kuhl, A. Czybulka, H. Shuster *Z. Anorg. Allg. Chem.* **1995**, *621*, 1.

[12] W. Westerhaus, U. Schuster *Z. Naturforsch.* **1977**, *32b*, 1365.

[13] W. Jung, J. Lörincz, R. Ramlau, H. Borrmann, Y. Prots, F. Haarmann, W. Schnelle, U. Burkhardt, M. Baitinger, Yu. Grin *Angew. Chem.* **2007**, *46*, 1.

[14] G. C. Che, M. Ellner, K. Schubert *J. Mater. Sci.* **1991**, *26*, 2417.

[15] J. T. Zhao, J. Corbett *Inorg. Chem.* **1994**, *33*, 5721.

[16] F. Merlo, M. Pani, M. L. Fornasini *J. Alloys Compds.* **1993**, *196*, 145.

[17] M. Lutz, B. Findeis, M. Haukka, R. Graff, T. A. Pakkanen, L. H. Gade *Chem. Eur. J.* **2002**, *8*, 3269.

[18] T. B. Massalski, H. Okamoto, P. R. Subramanian, L. Kacprzak *Binary Alloy Phase Diagrams* 5th ed. ASM-International, Materials-Park, **2004**.

[19] G. S. Nolas, B. C. Chakoumakos, B. Mahieu, G. J. Long, T. J. R. Weakley *Chem. Mater.* **2000**, *12*, 1947.

[20] A. P. Wilkinson, C. Lind, R. A. Young, S. D. Shastri, P.L. Lee, G. S. Nolas *Chem. Mater.* **2002**, *14*, 1300.

6. Mercury substituted type-I clathrates $A_8Hg_3Ge_{43}$ (A = K, Rb)

6.1 Introduction

The synthesis of semiconducting clathrates may follow different routes, depending mostly on the properties of the tetrel atoms.[1,2] Sn-based clathrates are usually obtained by fusion of the elements at temperatures below 950 K. Due to the much higher melting points of the elements, the preparation of Si and Ge clathrates requires reaction temperatures around 1300 K as well as application of external pressure.[3] Alternatively, thermal decomposition of A_4Tt_4 phases (Tt = Si, Ge) under dynamic vacuum in order to remove the excess of A can be implemented for the synthesis of type-I A_8Tt_{46} and type-II $A_{24-x}Tt_{136}$ clathrates (A = Na, K, Rb, Cs).[4,5] Recently, high yields of $A_{8-x}Si_{46}$ (A = Na, K) were achieved by the oxidation of A_4Si_4 with gaseous HCl or H_2O below 700 K,[6] whereas the type-IX Ba_6Ge_{25} produced the type-I $Ba_8Cu_{6-x}Ge_{40+x}$ in rather high purity when reacted with stoichiometric amounts of Cu and Ge.[7] In this context, the synthesis of Hg-substituted Ge clathrates using the neat solid A_4Ge_9 (A = K, Rb) as precursor is studied here.

6.2 Synthesis

Initially, the binary phases A_4Ge_9 (A = K, Rb)[8] were obtained by heating the elements to 873 K for two days in corundum crucibles. A small excess of alkali metal, namely A : Ge = 4.5 : 9 was used. Two different routes were then investigated for the synthesis of the clathrates. In the first method, equimolar amounts of A_4Ge_9 and Hg were loaded in Nb ampoules. These were weld-sealed, enclosed in quartz tubes, heated to 873 K for 24 hours, annealed at 673 K for 72 hours and subsequently cooled down to room temperature in a rate of 4 K min^{-1}. The products consisted of moderately crystalline powder of $A_8Hg_xGe_{46-x}$ and a secondary phase whose X-ray diffraction pattern remains unindexed. This admixture proved to be air sensitive and reacted exothermally with deionized H_2O. The presence of K^+ ions in the solution was verified by elemental analysis.[9] Some Hg drops were also observed and were removed under dynamic vacuum (12 hours at 373 K and 2 10^{-2} mbar) leading finally to pure phases of $A_8Hg_xGe_{46-x}$.

It seemed though crucial to use A_4Ge_9 in deficiency, because *α*-Ge -which was formed as byproduct otherwise- was not possible to remove. The preparation of

$K_8Hg_xGe_{46-x}$ was also attempted using the same reaction mixture at 570 K under ambient pressure in a corundum crucible enclosed in a steel autoclave. The product consisted mostly of $K_8Hg_xGe_{46-x}$ and unreacted K_4Ge_9. For the purification of the clathrate, the sample was transferred in a Schlenk tube under Ar atmosphere and was washed with 5 × 10 mL dimethylformamide (dmf). The clathrate was insoluble in dmf in contrast to K_4Ge_9 and the other admixtures that colored the solution deep red.

In the second method, a mixture of A_4Ge_9 : WO_3 : HgO was loaded in molar ratio 5:6:3 in a Nb ampoule and treated thermally exactly as in the first method. This reaction initially aimed for the synthesis of double salts of the type $A_{10}[Ge_9]_2WO_4$.[10] The reaction products consisted of gray, good quality single crystals of $A_8Hg_xGe_{46-x}$ as well as significant amounts of A_2WO_4 and *α*-Ge, according to the XRPD analysis. HgO decomposes already at 700 K allowing Hg to react with Ge, in its "activated" A_4Ge_9 form. The presence of WO_3 or eventually A_2WO_4 presumably favours the crystal growth of the clathrate, as recently found for K_4Ge_9 as well.[11] Noteworthy, attempts to synthesize the title compounds by fusion of the pure elements were rather unsuccessful. The substantial vapor pressure of Hg at high temperatures triggered the swelling of the ampoule till it cleaved, leading to the escape of Hg and alkali metals. Only the reaction of A and Ge (or $A_8Ge_{44}\square_2$[12]) with excess of Hg at 973 K for 15 days did result in $A_8Hg_xGe_{46-x}$ but in yields below 10%, as indicated by the quantitative analysis of the corresponding powder diffractograms.

6.3 Crystal structure determination

6.3.1 Powder X-ray diffraction

As already mentioned, the synthesis of the clathrates using the first method led also to the formation of an air sensitive admixture whereas in the second method to the formation of A_2WO_4 and *α*-Ge. The theoretical pattern of the clathrate in Figures 6.1 and 6.2 is based on the single-crystal XRD analysis (Chapter 6.3.2) and fits well to the experimental powder diagrams. Rietveld analyses were only performed for the powdered samples obtained by the A_4Ge_9 : Hg synthesis route after the aforementioned purification procedure. The composition of the compounds was refined as $K_8Hg_{3.37(3)}Ge_{42.63(3)}$ (Figure 6.3, Table 6.1) and $Rb_8Hg_{3.43(3)}Ge_{42.57(3)}$ (Figure 6.4, Table 6.2).

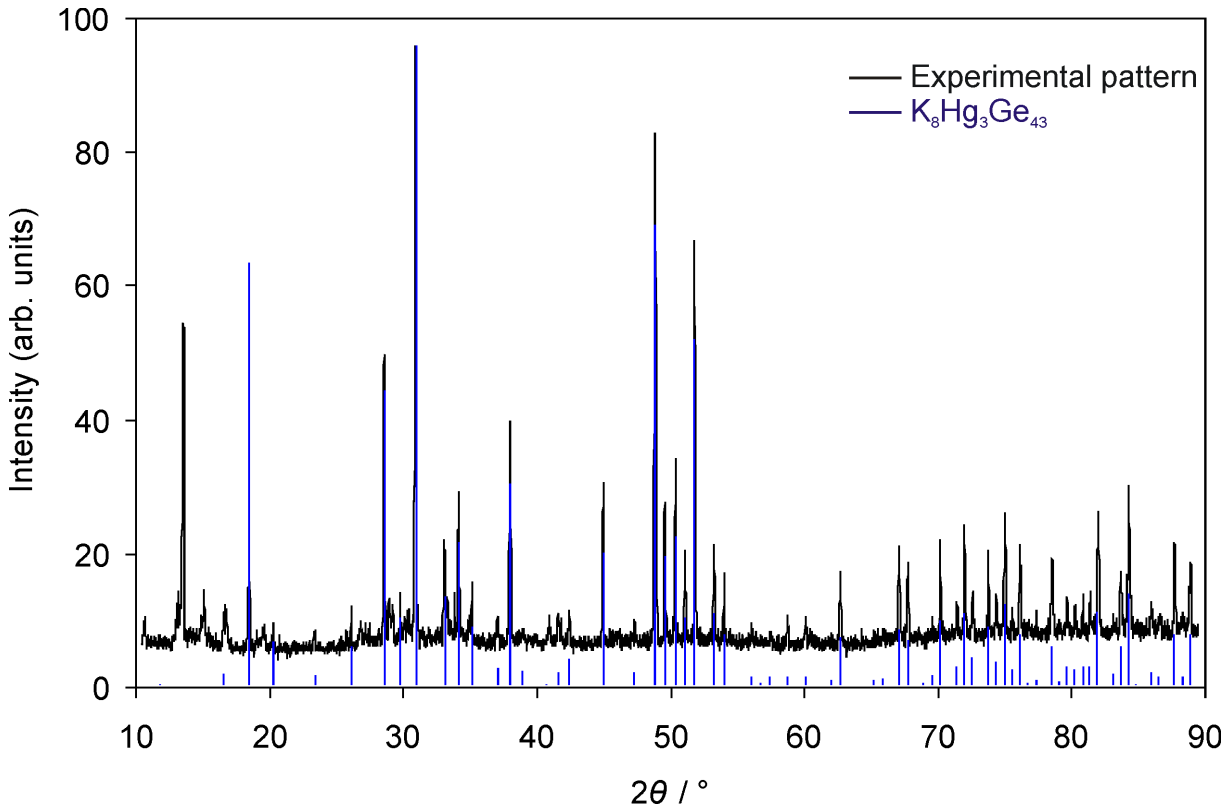

Figure 6.1 Powder diffraction pattern obtained from the reaction of K_4Ge_9 with Hg and recorded in Debye-Scherrer mode. Some unindexed reflections are observed at low angles.

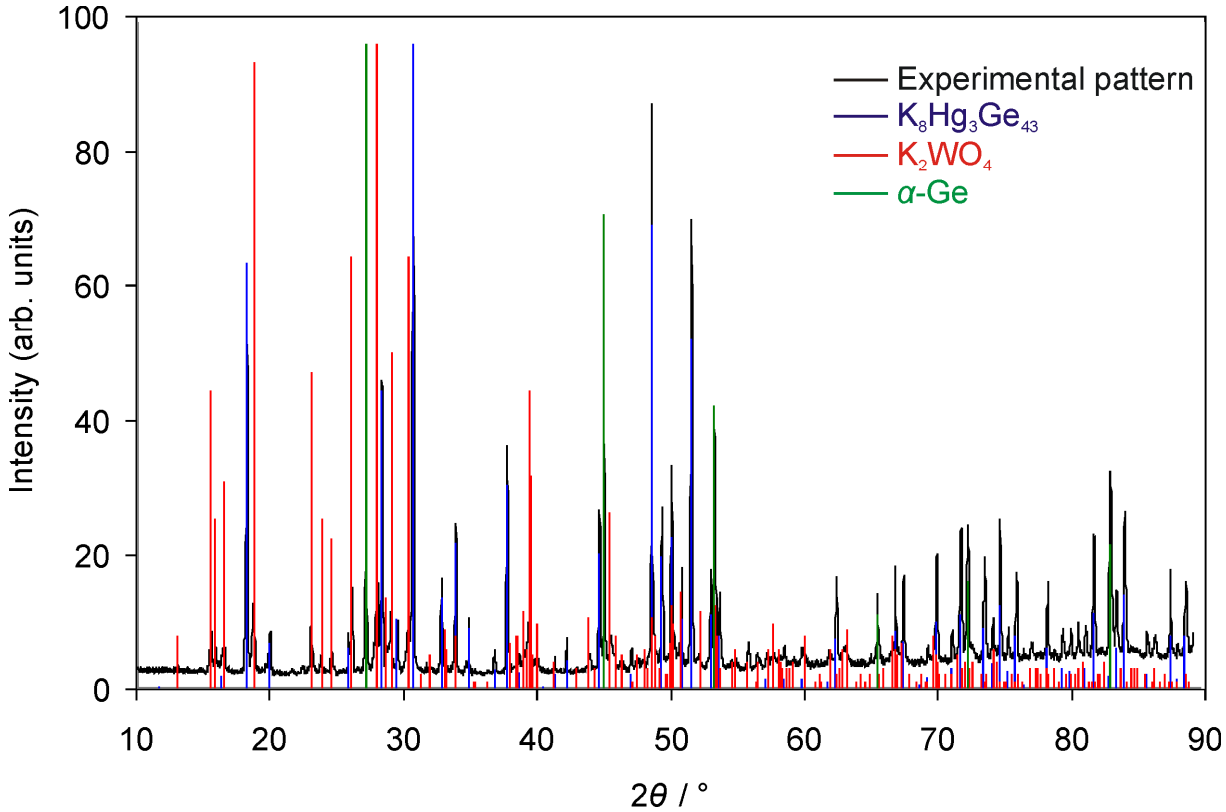

Figure 6.2 Powder diffraction pattern from the reaction of K_4Ge_9 with WO_3 and HgO recorded in Debye-Scherrer mode.

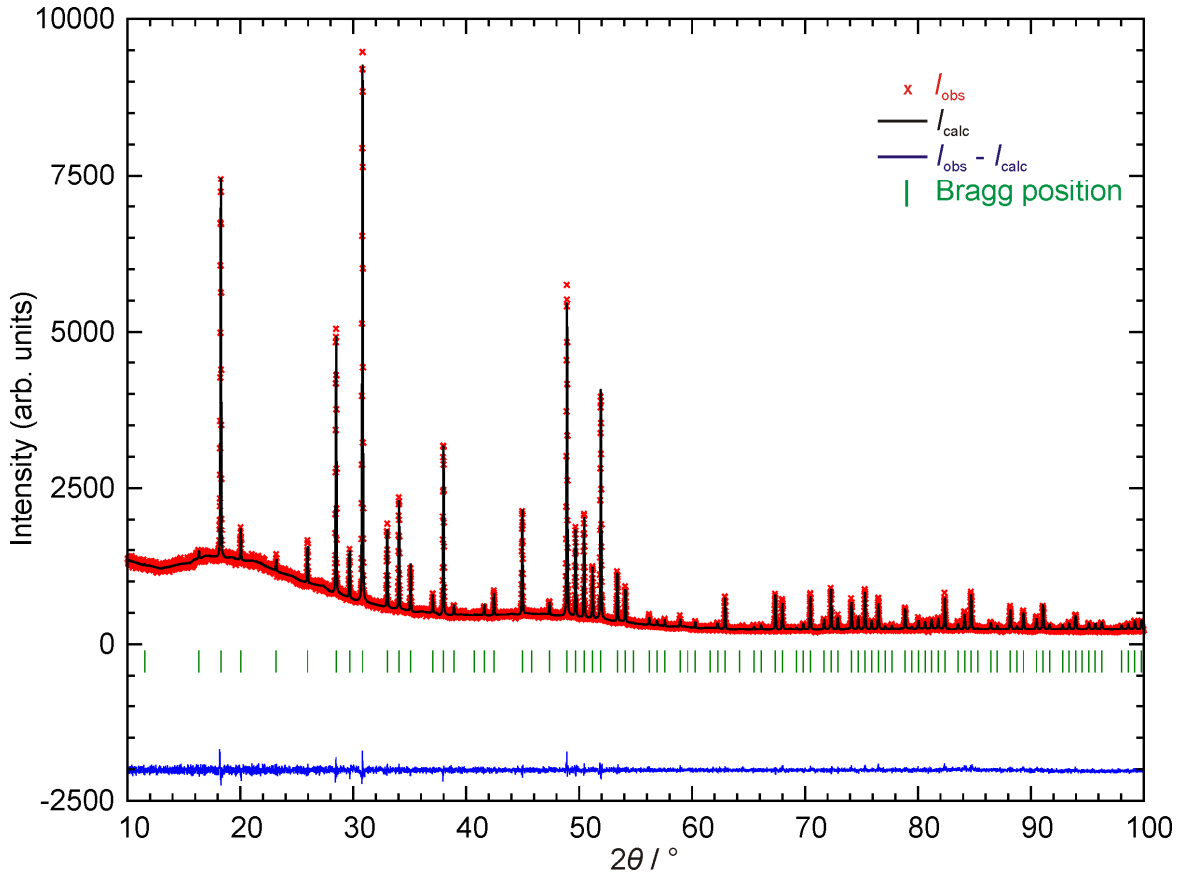

Figure 6.3 Rietveld refinement of powder diffraction data for $K_8Hg_{3.37(3)}Ge_{42.63(3)}$ (space group $Pm\bar{3}n$, a = 10.8469(1) Å) obtained from the reaction of K_4Ge_9 with Hg in transmission mode. General refinement parameters: R_{Bragg} = 0.035, R_{wp} = 0.178, χ^2 = 1.20.

Table 6.1 Atomic coordinates and isotropic displacement parameters for $K_8Hg_{3.37}Ge_{42.63}$.

Atom	Site	*x*	*y*	*z*	SOF	U_{iso} / Å^2
K1	2*a*	0	0	0	1	0.0118
K2	6*d*	0.25	0.5	0	1	0.0514
Hg/Ge1	6*c*	0.5	0.25	0	0.562/0.438(5)	0.0054
Ge2	16*i*	0.1833(1)	0.1833(1)	0.1833(1)	1	0.0042
Ge3	24*k*	0.3045(1)	0.1166(1)	0	1	0.0049

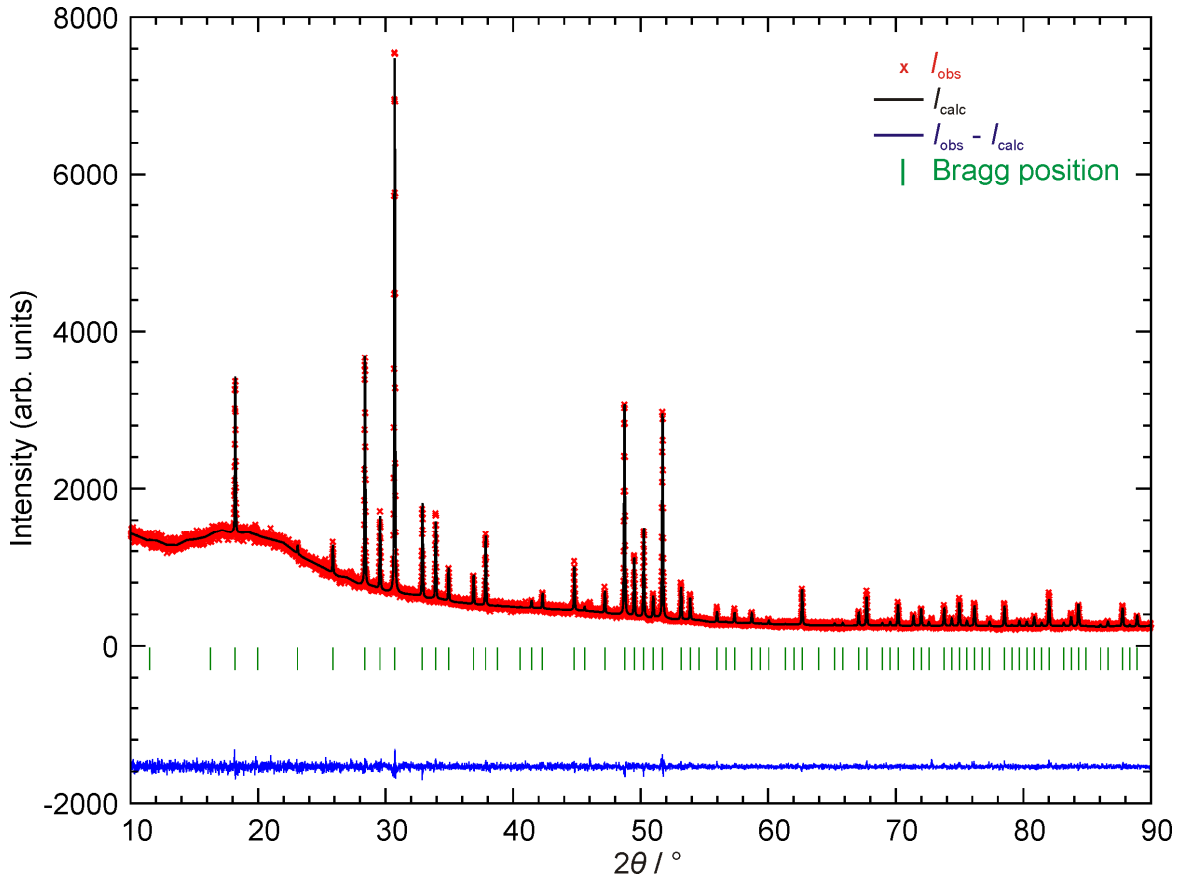

Figure 6.4 Rietveld refinement of powder diffraction data for $Rb_8Hg_{3.43(3)}Sn_{42.57(3)}$ (space group $Pm\bar{3}n$, a = 10.8869(1) Å) obtained from the reaction of Rb_4Ge_9 with Hg in transmission mode. General refinement parameters: R_{Bragg} = 0.0355, R_{wp} = 0.216, χ^2 = 1.12.

Table 6.2 Atomic coordinates and isotropic displacement parameters for $Rb_8Hg_{3.43}Sn_{42.57}$.

Atom	Site	*x*	*y*	*z*	SOF	U_{iso} / Å^2
Rb1	2*a*	0	0	0	1	0.0065
Rb2	6*d*	0.25	0.5	0	1	0.0257
Hg/Ge1	6*c*	0.5	0.25	0	0.572/0.428(5)	0.0025
Ge2	16*i*	0.1832(1)	0.1832(1)	0.1832(1)	1	0.00167
Ge3	24*k*	0.3046(2)	0.1174(2)	0	1	0.00303

6.3.2 Single-crystal X-ray diffraction

Good quality single crystals were obtained via the synthetic route of A_4Ge_9 : WO_3 : HgO and were mounted on the Oxford Xcalibur3 diffractometer equipped with a CCD detector. Full data collections at room temperature included four series of 138 frames with 30 sec exposure time and a crystal-detector distance of 50 mm. The integrated data were corrected numerically for absorption (Table 6.3). $A_8Hg_xGe_{46-x}$ adopt the clathrate-I structure (Figure 6.5, Table 6.4) with primitive cubic lattice. The crystallographic sites of the four-bonded framework atoms are 6*c*, 16*i* and 24*k*, whereas those of the guest atoms are 2*a* and 6*d*. All sites are fully occupied; however the 6*c* site is mixed-occupied by Hg and Ge. According to the single-crystal analysis, x equals to 3.19(5) for $K_8Hg_xGe_{46-x}$ and to 3.03(7) for $Rb_8Hg_xGe_{46-x}$.

Table 6.3 Crystal and structure refinement parameters for $K_8Hg_{3.19}Ge_{42.81}$ and $Rb_8Hg_{3.03}Ge_{42.97}$.

Chemical formula	$K_8Hg_{3.19(5)}Ge_{42.81(5)}$	$Rb_8Hg_{3.03(7)}Ge_{42.97(7)}$
Space group (No.)	$Pm\bar{3}n$ (223)	$Pm\bar{3}n$ (223)
Formula weight	4060.26	4410.74
Temperature, T / K	293	293
Diffractometer	Oxford Xcalibur3	Oxford Xcalibur3
Radiation, λ / Å	Mo-Kα, 0.71073	Mo-Kα, 0.71073
Z	1	1
A / Å	10.849(1)	10.875(1)
V / Å^3	1276.9(3)	1286.1(3)
$\rho_{calc.}$ / g cm^{-3}	5.280	5.695
Absorption coeff., μ / mm^{-1}	34.94	41.18
F(000)	1777	1913
θ range for data collection / °	4.20 - 27.82	4.19 - 27.75
Index ranges	$0 \le h \le 8$, $0 \le k \le 10$, $1 \le l \le 14$	$0 \le h \le 8$, $0 \le k \le 10$, $1 \le l \le 14$
Reflections collected	10100	10214
Independent reflections	288 (R_{int} = 0.109)	298 (R_{int} = 0.095)
Parameters	17	17
Goodness-of-fit on F^2	1.093	1.125
Weighting parameters	a = 0.039, b = 0	a = 0.039, b = 0
Final R indices (I > 2σ(I))	R_1 = 0.028, wR_2 = 0.074	R_1 = 0.031, wR_2 = 0.078
R indices (all data)	R_1 = 0.037, wR_2 = 0.079	R_1 = 0.045, wR_2 = 0.089
Largest diff. peak and hole / e Å^{-3}	1.45 in 1.39 Å from Ge3 –1.27 in1.03 Å from K1	1.89 in 2.29 Å from Ge3 –2.57 in 2.46 Å from Rb1

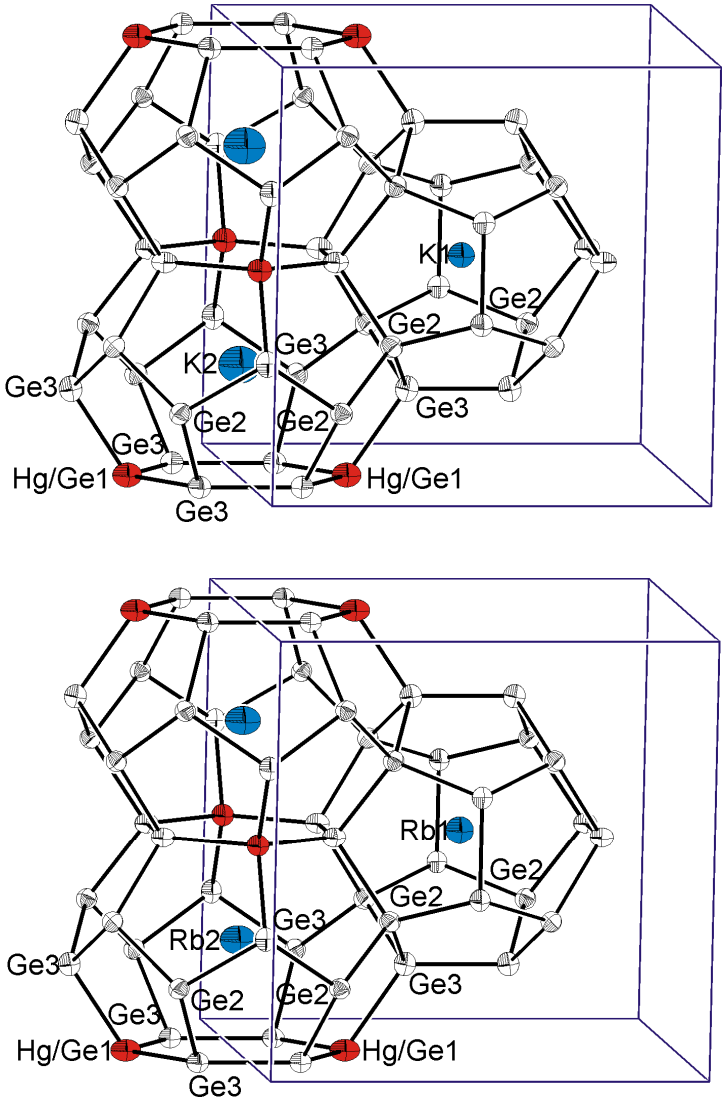

Figure 6.5 Partial view of the clathrate-I structure for $A_8Hg_xGe_{46-x}$. Two types of framework cages in the unit cell are centered by the guest metal (A1@Ge_{20} and A2@$(Ge/Hg)_{24}$). All thermal ellipsoids are presented at 90% probability level.

As expected, the Hg/Ge-Ge bonds are slightly longer than the Ge-Ge bonds (Table 6.5). Moreover, $Rb_8Hg_{3.03}Ge_{42.97}$ shows a slight increase of all interatomic distances compared to $K_8Hg_{3.19}Ge_{42.81}$, due to the different radii of the alkali metals (*d*(Hg/Ge-Ge) = 2.5634(8) Å and average *d*(Ge-Ge) = 2.503(1) Å for $K_8Hg_{3.19}Ge_{42.81}$, whereas *d*(Hg/Ge-Ge) = 2.564(2) Å and average *d*(Ge-Ge) = 2.511(2) Å for $Rb_8Hg_{3.03}Ge_{42.97}$). The increase however is smaller than one would expect based on the ionic radii ($r(K^+)$ = 1.38 Å and $r(Rb^+)$ = 1.52 Å) and it actually points out the rigidity of the Ge/Hg framework. The Ge-Ge bond lengths in $K_8Hg_3Ge_{43}$ and $Rb_8Hg_3Ge_{43}$ are slightly larger than those in *α*-Ge (*d* = 2.445 Å) and K_8Ge_{44} (average *d* = 2.471 Å).[12] Lastly, the Hg-Ge bond lengths are similar to the values of 2.54 - 2.61 Å and 2.55 Å found for the clusters [K([2.2.2]-crypt)]$_2$[$HgGe_9$](en)$_2$[13] and [K([2.2]-crypt)]$_2$[$HgGe_9$](dmf), respectively.[14]

Table 6.4 Atomic coordinates and equivalent isotropic displacement parameters for $K_8Hg_{3.19}Ge_{42.81}$ and $Rb_8Hg_{3.03}Ge_{42.97}$.

Atom	Site	*x*	*y*	*z*	SOF	U_{eq} / Å^2
			$K_8Hg_{3.19}Ge_{42.81}$			
K1	2*a*	0	0	0	1	0.017(2)
K2	6*d*	0.25	0.5	0	1	0.038(2)
Hg/Ge1	6*c*	0.5	0.25	0	0.532/0.468(9)	0.0161(5)
Ge2	16*i*	0.18350(7)	0.18350(7)	0.18350(7)	1	0.0114(4)
Ge3	24*k*	0.3047(1)	0.1169(1)	0	1	0.0133(4)
			$Rb_8Hg_{3.03}Ge_{42.97}$			
Rb1	2*a*	0	0	0	1	0.018(1)
Rb2	6*d*	0.25	0.5	0	1	0.0265(8)
Hg/Ge1	6*c*	0.5	0.25	0	0.51/0.49(1)	0.0149(6)
Ge2	16*i*	0.18362(9)	0.18362(9)	0.18362(9)	1	0.0101(5)
Ge3	24*k*	0.3049(1)	0.1175(1)	0	1	0.0115(5)

Table 6.5 Interatomic distances for $K_8Hg_{3.19}Ge_{42.81}$ and $Rb_8Hg_{3.03}Ge_{42.97}$.

$K_8Hg_{3.19}Ge_{42.81}$		$Rb_8Hg_{3.03}Ge_{42.97}$	
Atomic pairs	*d* / Å	Atomic pairs	*d* / Å
Hg/Ge1 -Ge3	2.5634(8) 4×	Hg/Ge1-Ge3	2.564(1) 4×
Ge2 -Ge2	2.499(1)	Ge2-Ge2	2.501(1)
-Ge3	2.493(1) 3×	-Ge3	2.499(1) 3×
Ge3 -Ge3	2.537(2)	Ge3-Ge3	2.555(2)
K1 -Ge2	3.4481(8) 8×	Rb1-Ge2	3.458(1) 8×
-Ge3	3.541(1) 12×	-Ge3	3.554(2) 12×
K2 -Ge3	3.668(1) 8×	Rb2-Ge3	3.677(1) 8×
-Hg/Ge1	3.8357(3) 4×	-Hg/Ge1	3.8449(3) 4×
-Ge2	4.0341(8) 8×	-Ge2	4.043(1) 8×
-Ge3	4.1980(5) 4×	-Ge3	4.2025(5) 4×

Both compounds exhibit anisotropy in the thermal displacement for the A2 atoms in the large and asymmetric framework cavities (Table 6.6). Note that the corresponding ADP values for $A_8Hg_4Sn_{42}$ (A = K, Rb) (Table 5.9) are more than double, due to the oversized Sn tkad cages. Finally, anisotropy is also observed in the displacement parameters of the Hg/Ge1 site, in the same manner as for $A_8Hg_4Sn_{42}$ (A = K, Rb, Cs) in Chapter 5.3.2.

Table 6.6 Anisotropic displacement parameters for $K_8Hg_{3.19}Ge_{42.81}$ and $Rb_8Hg_{3.03}Ge_{42.97}$ (in Å^2).

Atom	U_{11}	U_{22}	U_{33}	U_{12}	U_{23}	U_{13}
			$K_8Hg_{3.19}Ge_{42.81}$			
K1	0.017(2)	U_{11}	U_{11}	0	0	0
K2	0.032(4)	0.042(3)	U_{22}	0	0	0
Hg/Ge1	0.0139(6)	0.0205(9)	U_{11}	0	0	0
Ge2	0.0114(4)	U_{11}	U_{11}	–0.0007(3)	U_{12}	U_{12}
Ge3	0.0159(7)	0.0125(6)	0.0115(6)	0.0007(5)	0	0
			$Rb_8Hg_{3.03}Ge_{42.97}$			
Rb1	0.018(1)	U_{11}	U_{11}	0	0	0
Rb2	0.019(2)	0.030(1)	U_{22}	0	0	0
Hg/Ge1	0.0113(7)	0.022(1)	U_{11}	0	0	0
Ge2	0.0101(5)	U_{11}	U_{11}	–0.0003(4)	U_{12}	U_{12}
Ge3	0.0133(8)	0.0115(8)	0.0096(8)	0.0003(6)	0	0

As already discussed in Chapter 5.3, the large correlation between the SOFs and the thermal displacement vectors of the mixed occupied sites reduces to some extent the accuracy of crystallographically determined composition. By comparing the results from single-crystal XRD, powder XRD and EDX analysis, the composition of the clathrates can be finally regarded as $A_8Hg_3Ge_{43}$ (Table 6.7).

Table 6.7 Composition of the ternary clathrates $A_8Hg_xGe_{46-x}$ determined by single-crystal and powder X-ray diffraction as well as EDX analysis.

	Single-crystal analysis (x)	Rietveld analysis (x)	EDX analysis (A : Hg : Ge)
$K_8Hg_xGe_{46-x}$	3.19(5)	3.37(3)	18(2) : 10(5) : 72(12)
$Rb_8Hg_xGe_{46-x}$	3.03(7)	3.43(3)	19(2) : 8(5) : 73(14)

6.4 Magnetic properties

A SQUID measurement was carried out for $K_8Hg_3Ge_{43}$ and $Rb_8Hg_3Ge_{43}$. The microcrystalline samples were first zero-field cooled to 2 K and checked for superconductivity in a field of 0.01 Tesla. In all cases, a superconducting magnetic transition at about 4 K (T_c = 4.1 K for Hg) was observed, which entails that traces of elemental Hg remain in the sample even after heating under dynamic vacuum. Furthermore, the magnetization of $K_8Hg_3Ge_{43}$ shows a stepwise change at 170 - 200 K. Nevertheless, this effect is not accompanied by any structural change, as verified by single-crystal XRD analysis at 150 K. In stronger magnetic fields both compounds show

weak and slightly temperature-dependent paramagnetism. The behavior resembles to some extent the expected Pauli paramagnetism.

6.5 Discussion

The use of the Zintl phases A_4Ge_9 (A = Na, K, Rb) as precursors for both solution and solid-state synthesis has been studied in the recent years. The reactivity of the $[Ge_9]^{4-}$ cluster varies immensely upon the reaction conditions: a) the guest-free type-II $\square_{24}Ge_{136}$ clathrate ($\square$ denotes here vacant cationic position) was synthesized by heating Na_4Ge_9 to 570 K in a 1:1 mixture of $AlCl_3$ and n-dodecyltrimethyl-ammoniumchloride (DTAC),[15] and b) the reaction of $[Ge_9]^{4-}$ clusters with Hg in ethylenediamine (en) or dimethylformamide (dmf) solutions led to the isolation of the polymer $^1_\infty[HgGe_9]^{2-}$.[13,14] The present study establishes the reaction of A_4Ge_9 phases with Hg to produce type-I clathrates $A_8Hg_3Ge_{43}$ in high yields (Figure 6.6).

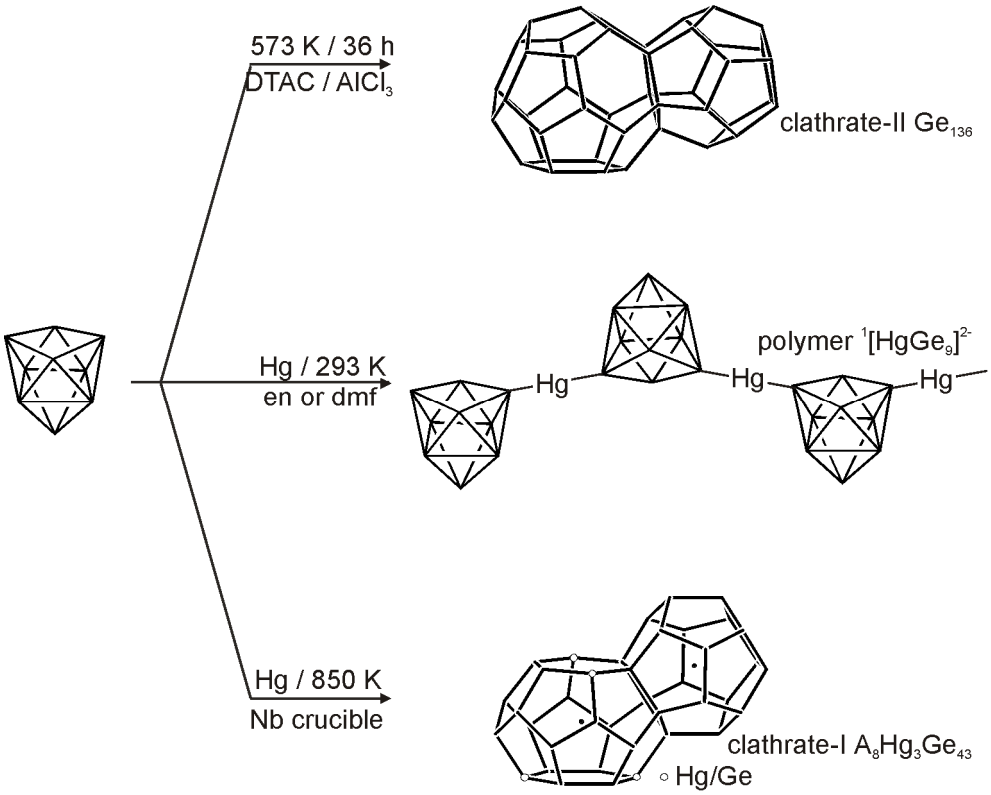

Figure 6.6 Reaction of the $[Ge_9]^{4-}$ cluster towards formation of the guest-free type-II clathrate Ge_{136} or the polymer $^1_\infty[HgGe_9]^{2-}$ or the clathrate-I $A_8Hg_3Ge_{43}$ (A = K, Rb).

According to the 8 – N rule, the conduction band of $A_8Hg_3Ge_{43}$ is occupied by two electrons, in agreement with the paramagnetic behavior found here. The class of known

ternary Ge clathrates shows in principle atom mixing on all three framework sites as it is observed for the triel-rich compounds $Ae_8Ga_{16}Ge_{30}$ (Ae = Sr, Ba).[16,17] Mixed positions on only two sites are discussed for $A_8Tr_8Ge_{38}$ (A = K, Rb, Cs and Tr = Al, Ga, In)[18,19] and $Ba_8M_8Ge_{38}$ (M = Zn, Cd),[20] whereas in compounds with smaller amounts of dopants such as $Ba_8M_6Ge_{40}$ (M = Cu, Ag, Au),[21] $K_8Zn_4Ge_{42}$[22] and the here presented $A_8Hg_3Ge_{43}$ (A = K, Rb) only one crystallographic site is statistically occupied by two atom types. Beside the title compounds all ternary phases fulfill the 8 – N rule, while $A_8Hg_3Ge_{43}$ is electron rich and follows the trend of the binary phases $A_{8-x}Si_{46}$ (A = Na, K, Ba) and $Ba_8Ge_{43}\square_3$.

6.6 References

[1] S. Bobev, S. C. Sevov *J. Sol. State Chem.* **2000**, *153*, 92.

[2] K. A. Kovnir, A. V. Shevelkov *Russ. Chem. Rev.* **2004**, *73*, 923.

[3] P. Rogl *International Conference on Thermoelectrics* **2005**, 443.

[4] E. Reny, P. Gravereau, C. Cros, M. Pouchard *J. Mater. Chem*. **1998**, *8*, 2839.

[5] H.-G. von Schnering, M. Somer, M. Kaupp, W. Carillo-Cabrera, M. Baitinger, A. Schmeding, Yu. Grin *Angew. Chem.* **1998**, *110*, 2507.

[6] B. Böhme, A. Guloy, Z. Tang, W. Schnelle, U. Burkhardt, M. Baitinger, Yu. Grin *J. Am. Chem. Soc.* **2007**, *129*, 5348.

[7] S. Johnsen, A. Bentien, G. Madsen, B. Iversen, M. Nygren *Chem. Mater.* **2006**, *18,* 4633.

[8] H.-G. von Schnering, M. Baitinger, U. Bolle, W. Carrillo-Cabrera, J. Curda, Yu. Grin, F. Heinemann, J. Llanos, K. Peters, A. Schmeding, M. Somer *Z. Anorg. Allg. Chem.* **1997**, *623*, 1037.

[9] G. Jander, E. Blasius *Einführung in das Anorganisch-chemische Praktikum* 15. Auflage, S. Hirzel Verlag Stuttgart, **2005**.

[10] S. Ponou *Ph.D. Thesis*, T.U. München, **2006**.

[11] S. Ponou, T. F. Fässler *Z. Anorg. Allg. Chem.* **2007**, *633*, 393.

[12] G. K. Ramachandran, P. F. McMillan, J. Dong, O. F. Sankey *J. Solid State Chem.* **2000**, *154*, 626.

[13] A. Nienhaus, R. Hauptmann, T. F. Fässler *Angew. Chem. Int. Ed.* **2002**, *41*, 3213.

[14] M. B. Boeddinghaus, S. D. Hoffmann, T. F. Fässler *Z. Anorg. Allg. Chem.* **2007**, *633*, 2338.

[15] A. Guloy, R. Ramlau, Z. Tang, W. Schnelle, M. Baitinger, Yu. Grin *Nature* **2006**, *443*, 320.

[16] G. S. Nolas, J. L. Cohn, G. A. Slack, S. B. Schujman *Appl. Phys. Lett.* **1998**, *73*, 178.

[17] M. Christensen, N. Lock, J. Overgaard, B. B. Iversen *J. Am. Chem. Soc.* **2006**, *128*, 15657.

[18] R. Kröner, K. Peters, H.-G. von Schnering, R. Nesper *Z. Kristallogr.-New Cryst. Struct.* **1998**, *213*, 675.

[19] H.-G. von Schnering, R. Kröner, H. Menke, K. Peters, R. Nesper *Z. Kristallogr.-New Cryst. Struct.* **1998**, *213*, 677.

[20] B. Kuhl, A. Czybulka, H.-U. Schuster *Z. Anorg. Allg. Chem.* **1995**, *621*, 1.

[21] G. Cordier, P. Woll *J. Less-Common. Met.* **1991**, *169*, 291.

[22] Q. Xie *Ph.D. Thesis*, ETH No. 15626, **2004**.

7. Summary

The present study deals with the synthesis, characterization and physical properties of Sn and Ge clathrates. All compounds adopt the type-I clathrate structure where the tetrel elements form large polyhedra in which the alkali metals reside. The encapsulation of the latter in the cavities is an irreversible procedure as without them the covalent framework collapses. The compounds are divided in two categories: a) binary A_8Sn_{44} (A = Rb, Cs) or pseudobinary $Rb_xCs_{8-x}Sn_{44}$ (x = 1.3, 1.4, 2.1) and b) ternary $A_8Hg_4Sn_{42}$ (A = K, Rb, Cs) and ternary $A_8Hg_3Ge_{43}$ (A = K, Rb).

7.1 Order-disorder phase transition in $Rb_xCs_{8-x}Sn_{44}$ ($0 \le x \le 8$)

The X-ray diffraction studies and thermal analysis have established a temperature-induced order-disorder phase transition in $Rb_xCs_{8-x}Sn_{44}\square_2$ ($0 \le x \le 8$) which occurs at 353 K for Rb_8Sn_{44}, 330 - 360 K for $Rb_{1.4}Cs_{6.6}Sn_{44}$ and 363 K for Cs_8Sn_{44}. The transformation regards the ordering of the framework defects (□) in the crystal lattice and is completely reversible. The *β* modification (space group $Pm\bar{3}n$) and possesses higher symmetry and lower ordering of the defects than the *α* form (space group $Ia\bar{3}d$) (Figure 7.1). As expected, the more disordered modification is favored at elevated temperatures by means of an entropy-driven phase transition.

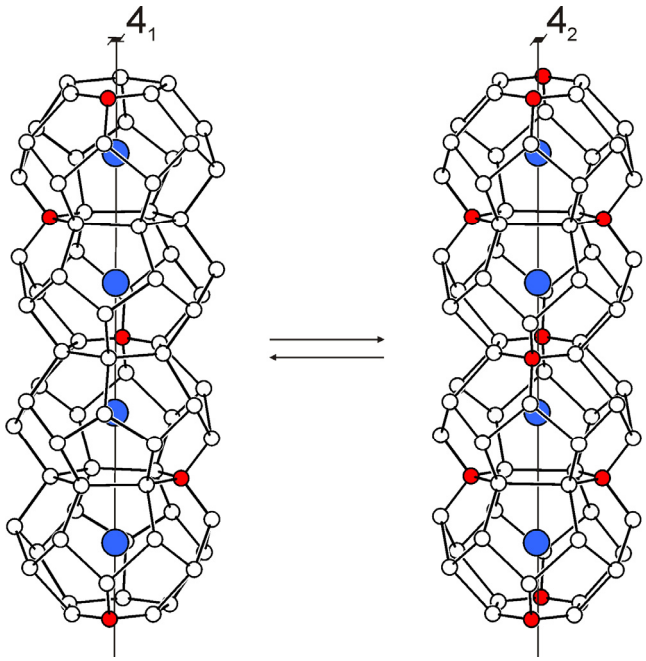

Figure 7.1 Order-disorder phase transition in A_8Sn_{44}. The underoccupied Sn sites (red spheres) are distributed along a 4_1 helical axis in *α*-A_8Sn_{44} (left) and along a 4_2 helical axis in *β*-A_8Sn_{44} (right). The alkali-metal atoms reside in the center of the cavities.

Beyond the crystallographic description, the chemical environment of the Sn atoms has been investigated by ^{119}Sn-Mössbauer and Raman spectroscopy. The results show explicitly the presence of negatively-charged, three-bonded Sn atoms, as a result of introducing vacancies in the framework. Furthermore, no significant difference is observed in the spectra for α-Rb_8Sn_{44} and β-Rb_8Sn_{44}, implying that the phase transition takes place without altering the local environment of the Sn atoms, but by varying the concentration of vacancies in different domains of the crystal. The substitution effects in the pseudobinary compounds $Rb_xCs_{8-x}Sn_{44}$ ($0 \le x \le 8$) have also been investigated. Both types of framework cavities show clear trend towards encapsulation of the larger alkali metal, namely Cs rather than Rb. A certain homogeneity range close to the composition $Rb_2Cs_6Sn_{44}$ is observed, although the cations are crystallographically not fully ordered even in the long-annealed samples.

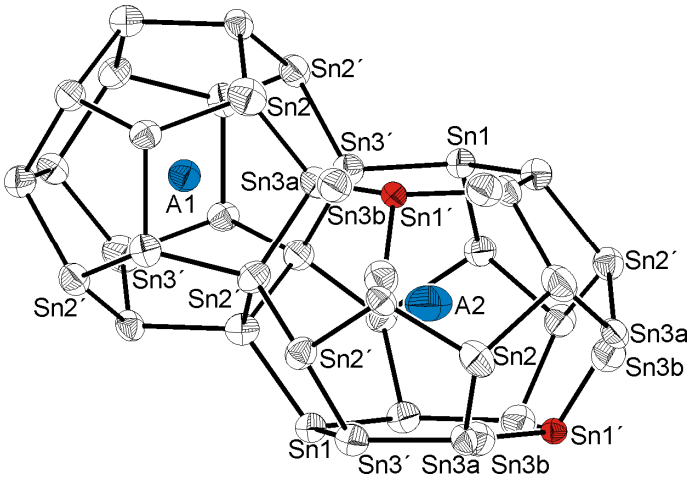

Figure 7.2 Partial view of the $Rb_{1.42}Cs_{6.58}Sn_{44}$ crystal structure. Displacement ellipsoids are drawn at 90% probability level. A1: Rb (46%), Cs (54%) and A2: Rb (8%), Cs (92%).

According to the electrical resistivity and magnetic susceptibilty measurements, the clathrates $Rb_xCs_{8-x}Sn_{44}\square_2$ ($0 \le x \le 8$) are diamagnetic semiconductors. Over the phase-transition temperature, the electrical resistivity decreases by a factor of about 4. The hysteresis observed between heating and cooling segments is indicative of a first-order phase transition (Figure 7.3). The transformation has also significant effect on the charge-carrier properties of the compounds. Thermoelectric measurements performed on a pressed sample of Rb_8Sn_{44} established that the more disordered modification exhibits larger Seebeck coefficient (in absolute value) and lower electrical resistivity (Figure 7.4).

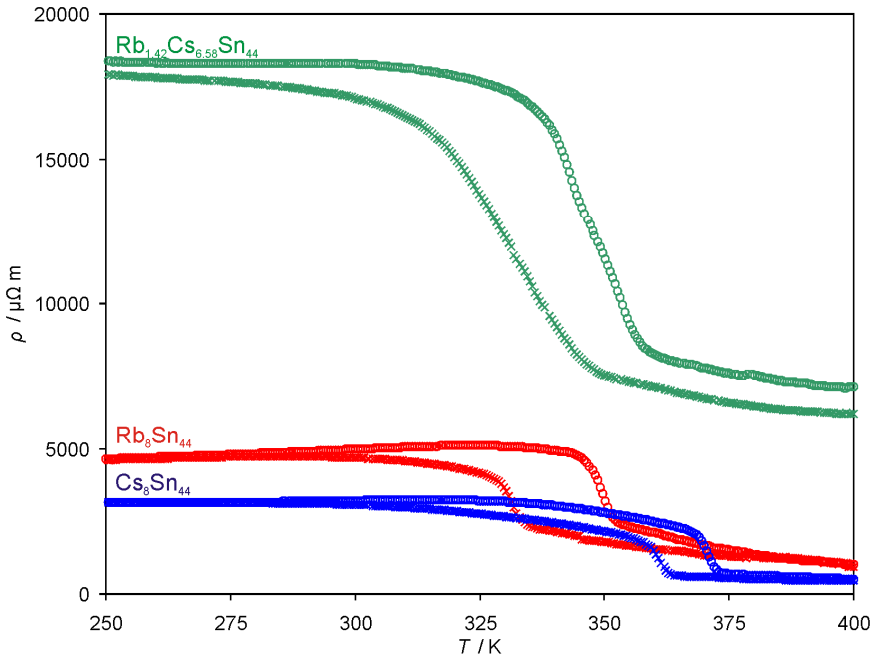

Figure 7.3 Electrical resistivity for single crystals of Rb_8Sn_{44}, $Rb_{1.42}Cs_{6.58}Sn_{44}$ and Cs_8Sn_{44} in the temperature range 250 - 400 K. Open circles and (×) denote the heating and cooling sequences, respectively.

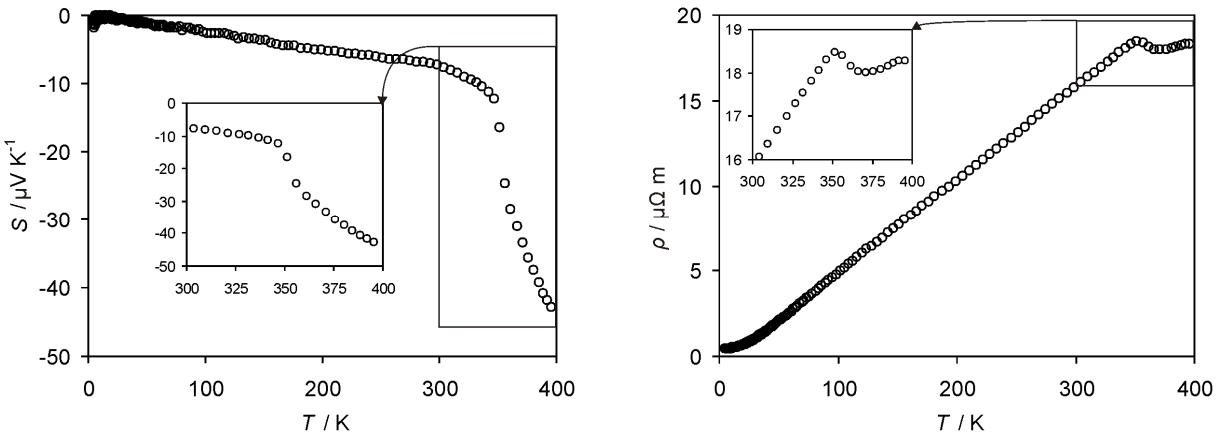

Figure 7.4 Seebeck coefficient (left) and electrical resistivity (right) for a pressed pellet of Rb_8Sn_{44}. The insets zoom in the phase-transition temperature. Values below 3.8 K have been removed due to a small superconducting Sn impurity.

Other physical properties such as thermal conductivity (Figure 7.5) and magnetic susceptibility seem virtually unaffected by the structural transformation. The rattling of the guest atoms as well as the framework vibrations have been investigated by Raman spectroscopy, ADPs from the synchrotron diffraction data and multi-temperature PDOS obtained from neutron time-of-flight scattering. The results show no abrupt change in the vibrational modes over the transition temperature. Nevertheless, the overall thermoelectric efficiency of Rb_8Sn_{44} is significantly affected by the phase transition. This fact points out how minor structural changes may influence the charge-carriers properties of a material.

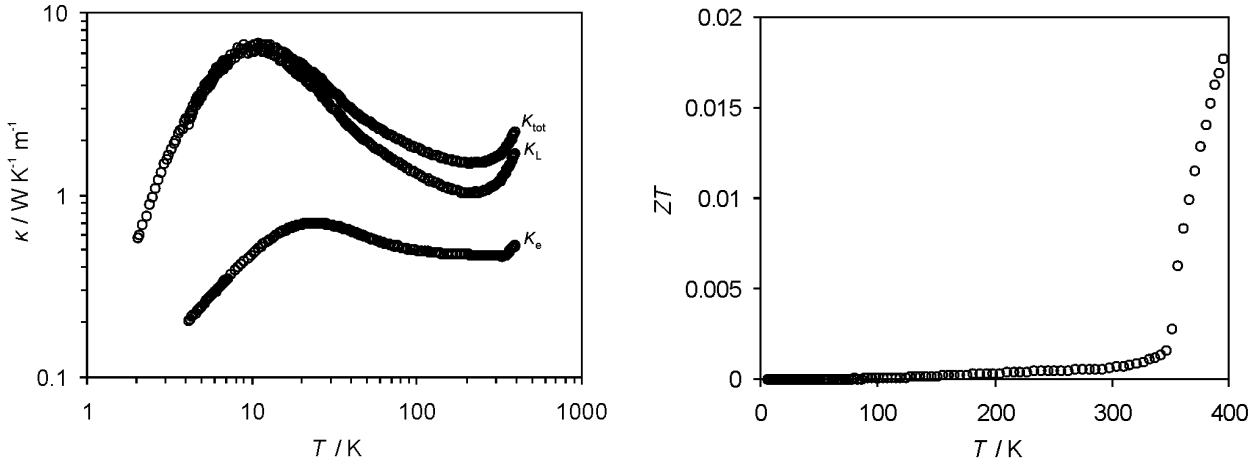

Figure 7.5 Thermal conductivity in logarithmic scale (left) and thermoelectric FOM (right) for a pressed pellet of Rb_8Sn_{44}. Values below 3.8 K have been removed due to a small superconducting Sn impurity.

7.2 Mercury substituted clathrates $A_8Hg_4Sn_{42}$ and $A_8Hg_3Ge_{43}$ (A = K, Rb, Cs)

The compounds $A_8Hg_4Sn_{42}$ are the first reported cases of Hg-substituted clathrates. Despite the rather unusual tetrahedral coordination, Hg forms stable bonds with the Sn atoms, as indicated by the higher thermal stability of $A_8Hg_4Sn_{42}$ compared to A_8Sn_{44}. The encapsulation of large alkali metals, in order to avoid their strong rattling in the cavities also enhances the thermal stability (Figures 7.6). This rationalizes the fact that no type-I Sn clathrates with small guest atoms such as Na, Cu and Ag have been synthesized. The compounds constitute also the heaviest members of the rapidly growing family of semiconducting clathrates doped with group 11 - 13 elements. Therefore, they appear interesting for minimizing the lattice thermal conductivity.

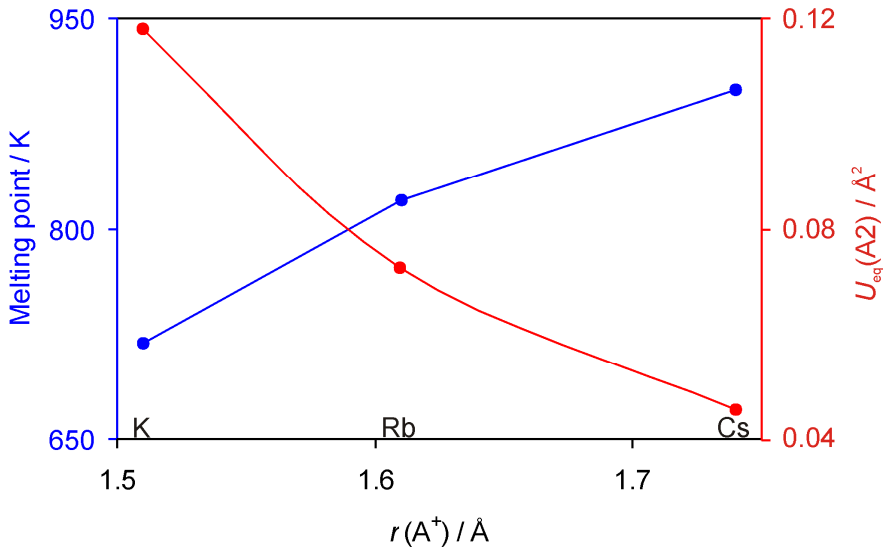

Figure 7.6 Melting point of $A_8Hg_4Sn_{42}$ (A = K, Rb, Cs) and equivalent thermal displacement for the alkali metals in the tkad as a function of the ionic radius (A^+).

In contrast to A_8Sn_{44} and $A_8Hg_4Sn_{42}$ where the synthesis was achieved by fusing the elements at elevated temperatures, the preparation of the $A_8Hg_3Ge_{43}$ (A = K, Rb) clathrates succeeded only with the use of the Zintl phases A_4Ge_9 as precursors. The current study points out the reactivity of the $[Ge_9]^{4-}$ clusters in different media (Figure 7.7) and also suggests a reproducible method for the synthesis of clathrates in high yields and temperatures that do not exceed 870 K. However, these new clathrates do not follow the normal electron-counting rules for Zintl phases as also indicated by their weak paramagnetic behavior. The composition is refined by single-crystal and powder X-ray diffraction and indicates lower content of Hg, compared to $A_8Hg_4Sn_{42}$ (A = K, Rb, Cs).

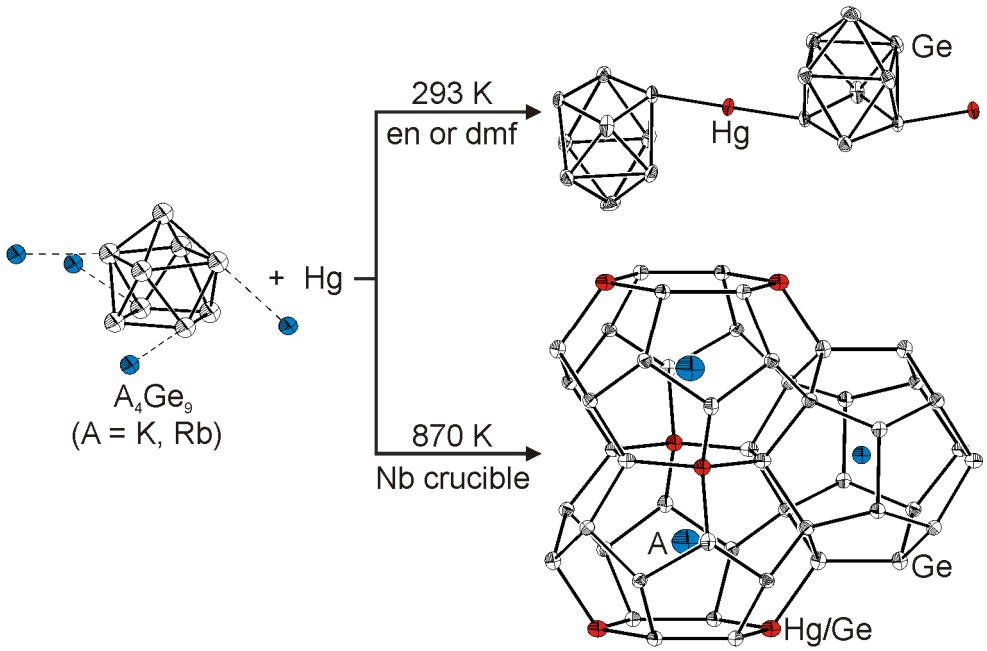

Figure 7.7 Reaction of $[Ge_9]^{4-}$ with Hg towards formation of the polymer $^1_\infty[HgGe_9]^{2-}$ or the clathrate-I $A_8Hg_3Ge_{43}$ (A = K, Rb).

Appendix A. Phase diagrams of binary systems

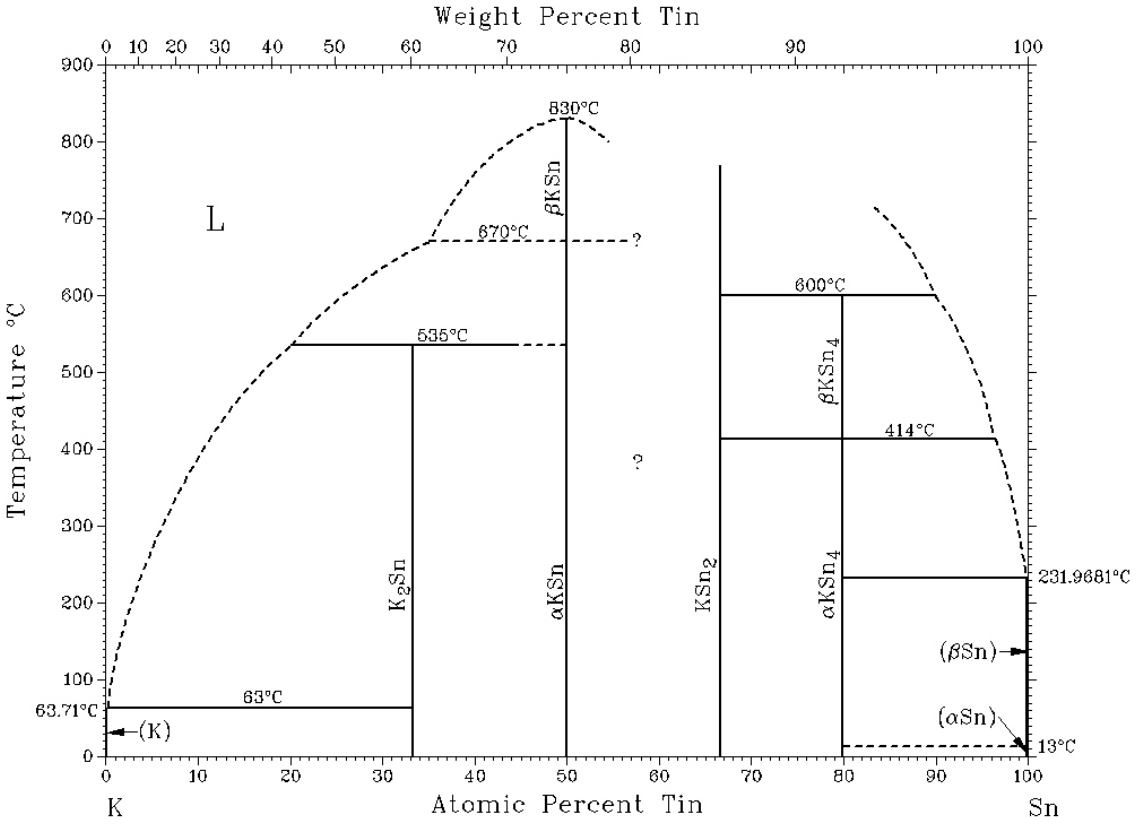

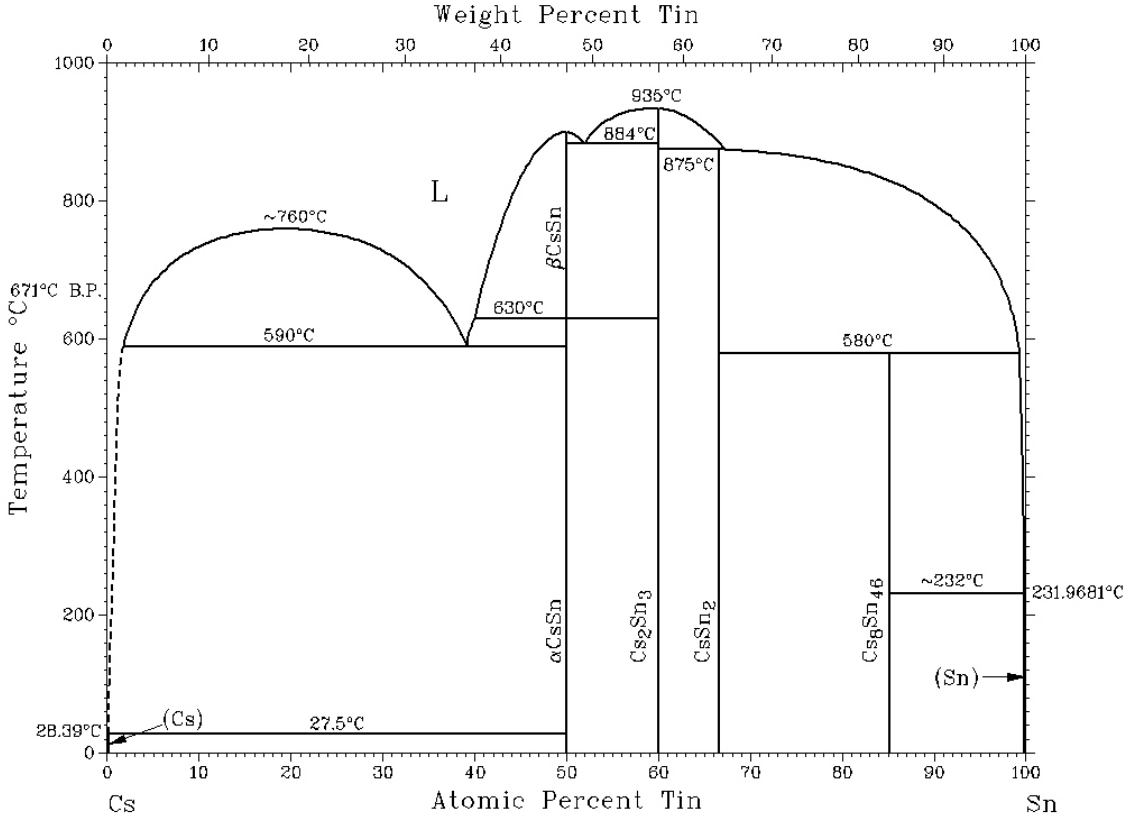

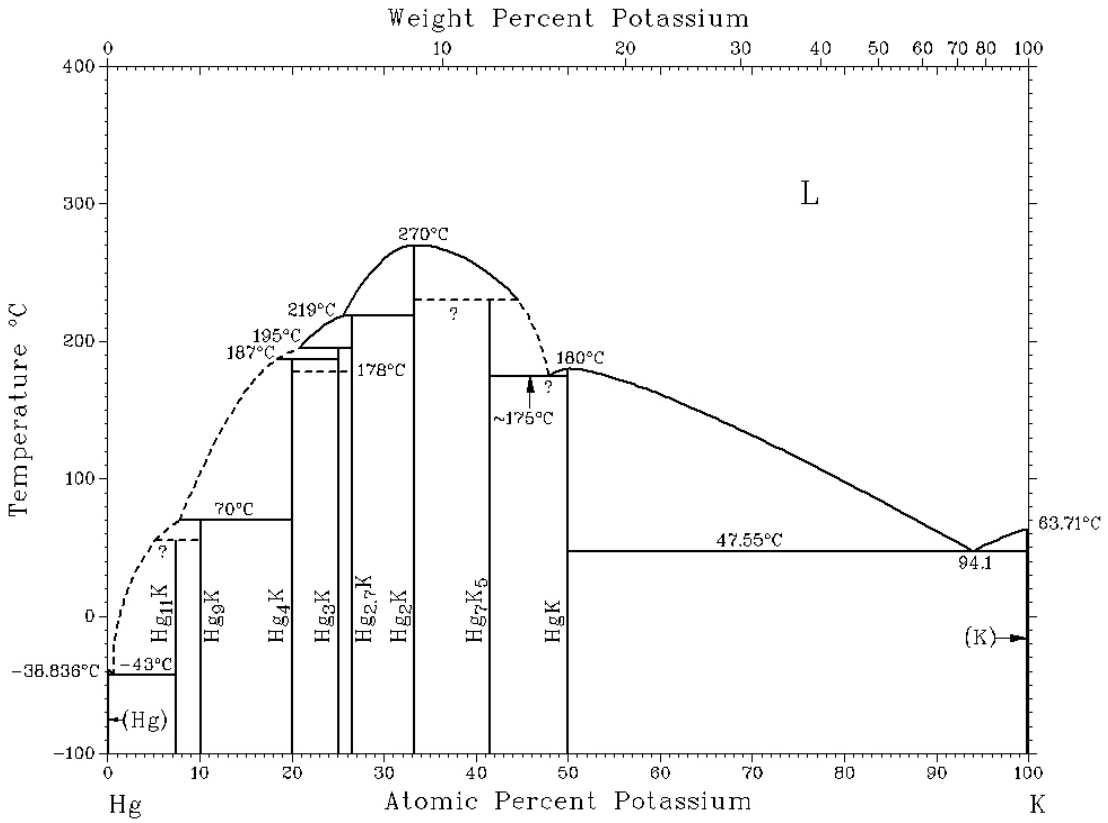
Weight Percent Potassium
Temperature °C
Atomic Percent Potassium
Hg
K
L
270°C
219°C
195°C
187°C
178°C
180°C
~175°C
70°C
47.55°C
94.1
63.71°C
-43°C
-38.836°C
(Hg)
(K)
Hg11K
Hg9K
Hg4K
Hg3K
Hg2.7K
Hg2K
Hg7K6
HgK

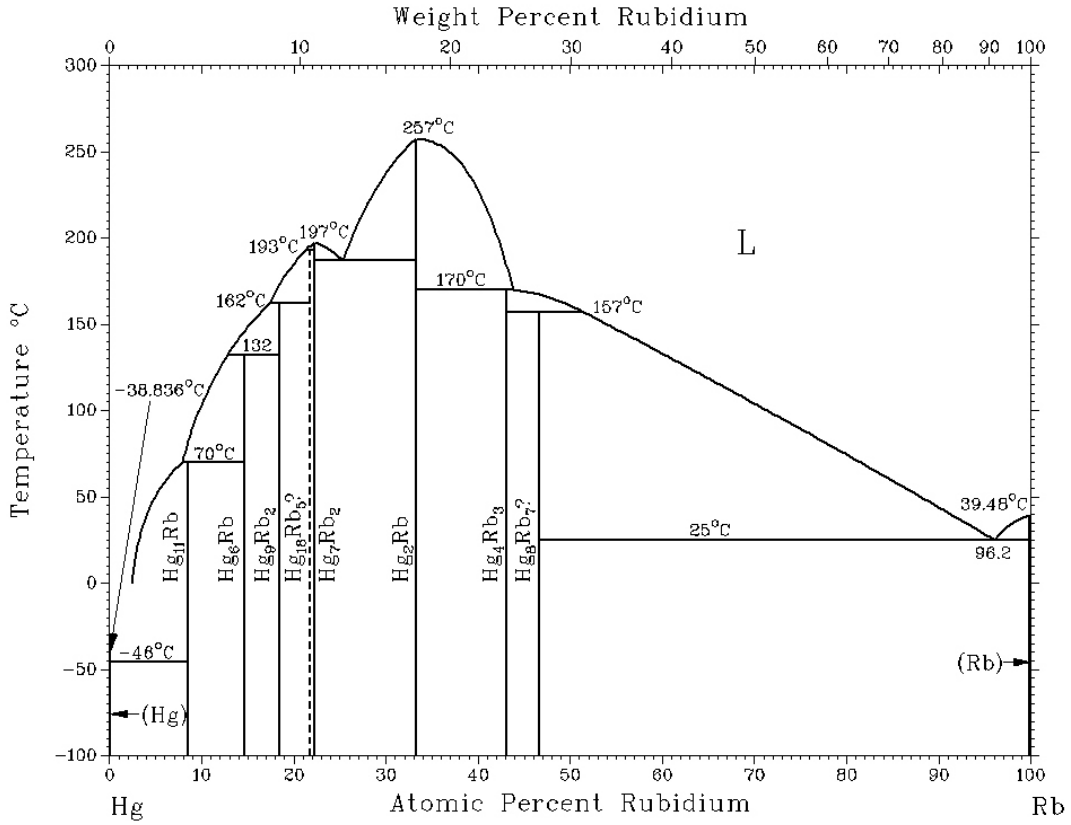
Weight Percent Rubidium
Temperature °C
Atomic Percent Rubidium
Hg
Rb
L
257°C
193°C
197°C
170°C
162°C
157°C
132
-38.836°C
70°C
39.48°C
25°C
96.2
-46°C
(Hg)
(Rb)
Hg11Rb
Hg6Rb
Hg9Rb2
Hg18Rb5?
Hg7Rb2
Hg2Rb
Hg4Rb3
Hg8Rb7?

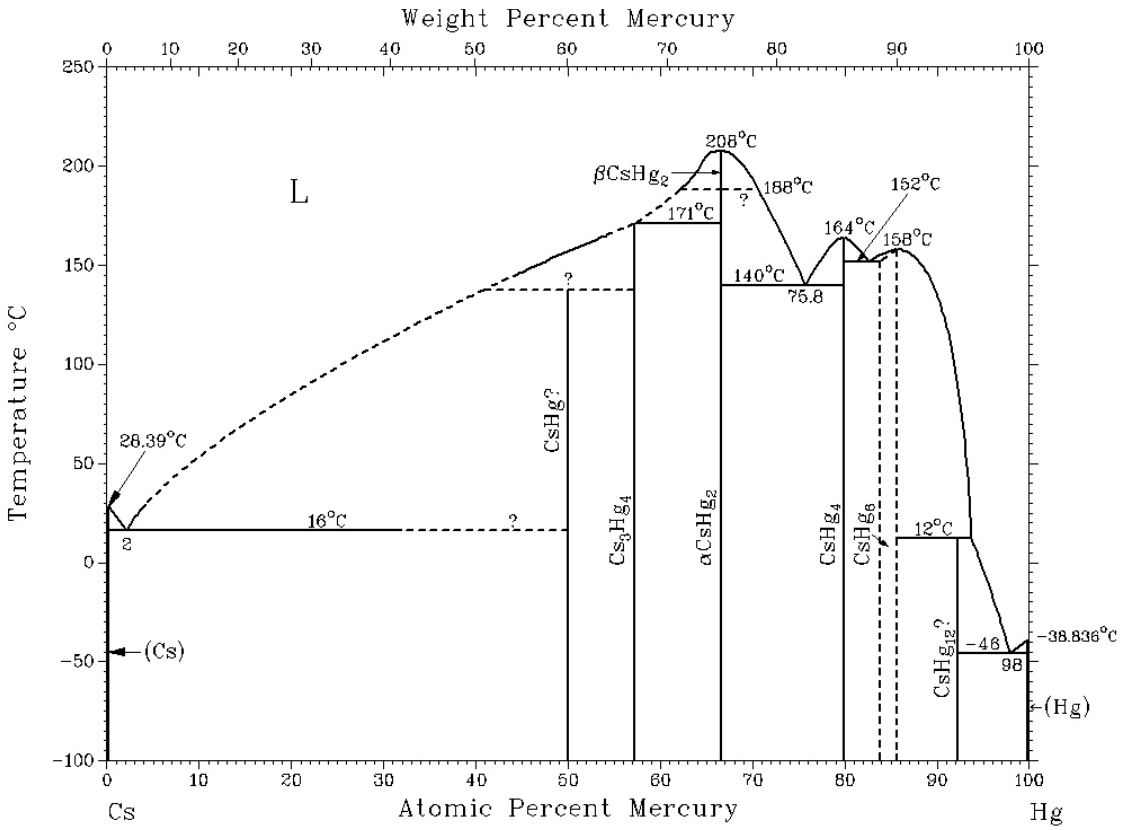
Weight Percent Mercury
Temperature °C
Atomic Percent Mercury
Cs
Hg
L
208°C
βCsHg2
188°C
171°C
164°C
152°C
158°C
140°C
75.8
28.39°C
16°C
CsHg?
Cs3Hg4
αCsHg2
CsHg4
CsHg6
12°C
CsHg12?
-46
98
-38.836°C
(Cs)
(Hg)

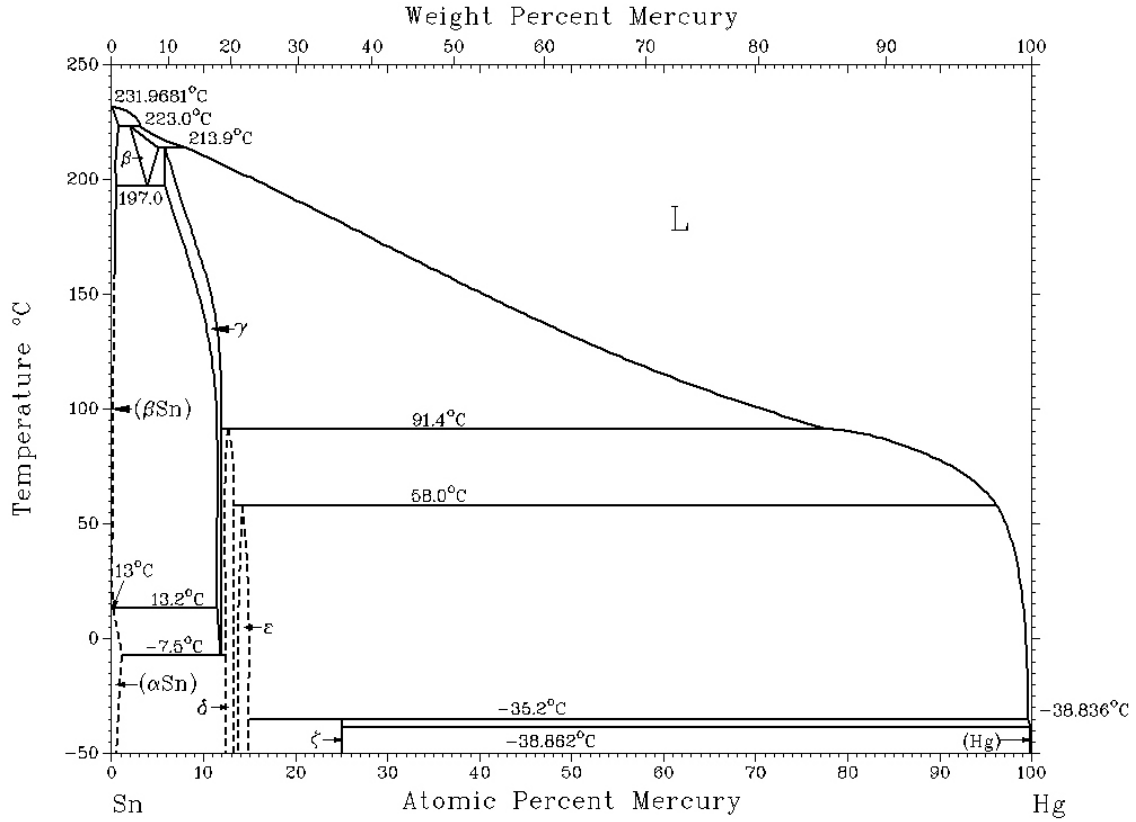
Weight Percent Mercury
Temperature °C
Atomic Percent Mercury
Sn
Hg
L
231.9681°C
223.0°C
213.9°C
β
197.0
γ
(βSn)
91.4°C
58.0°C
13°C
13.2°C
-7.5°C
(αSn)
δ
ε
-35.2°C
ζ
-38.862°C
(Hg)
-38.836°C

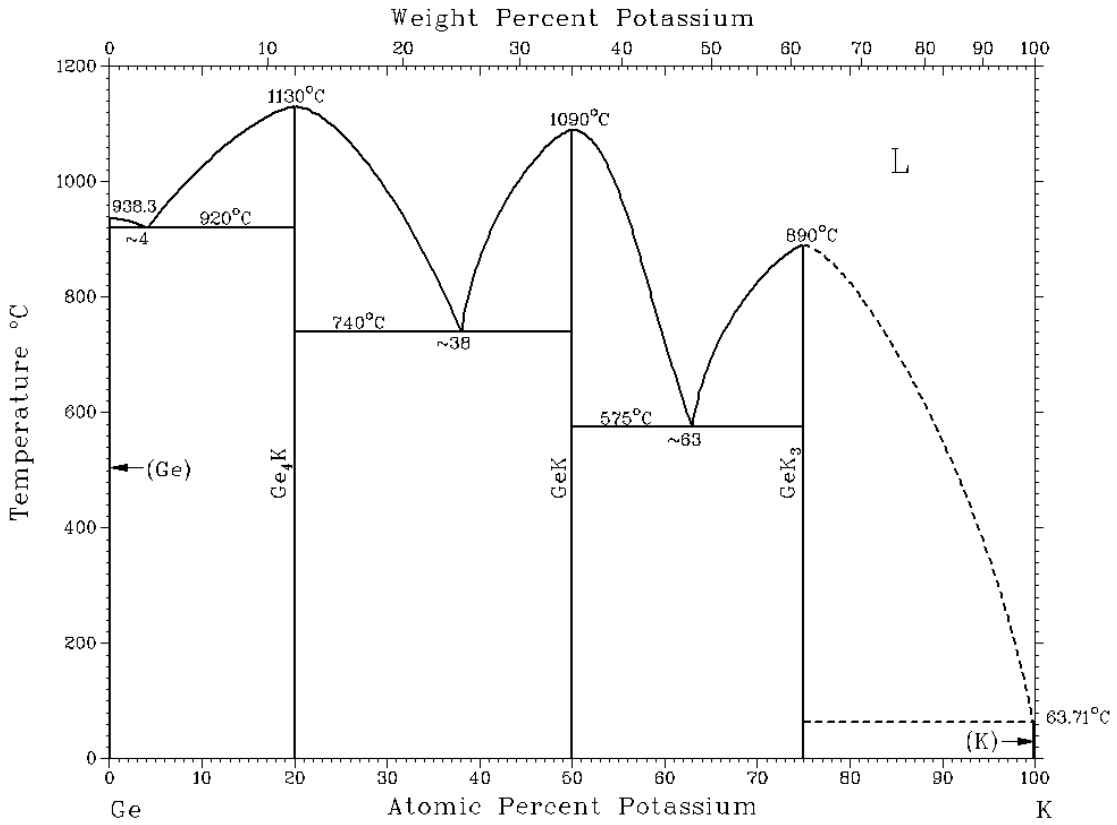
Weight Percent Potassium
Temperature °C
Atomic Percent Potassium
Ge
K
L
1130°C
1090°C
938.3
920°C
~4
890°C
740°C
~38
575°C
~63
(Ge)
Ge4K
GeK
GeK3
63.71°C
(K)

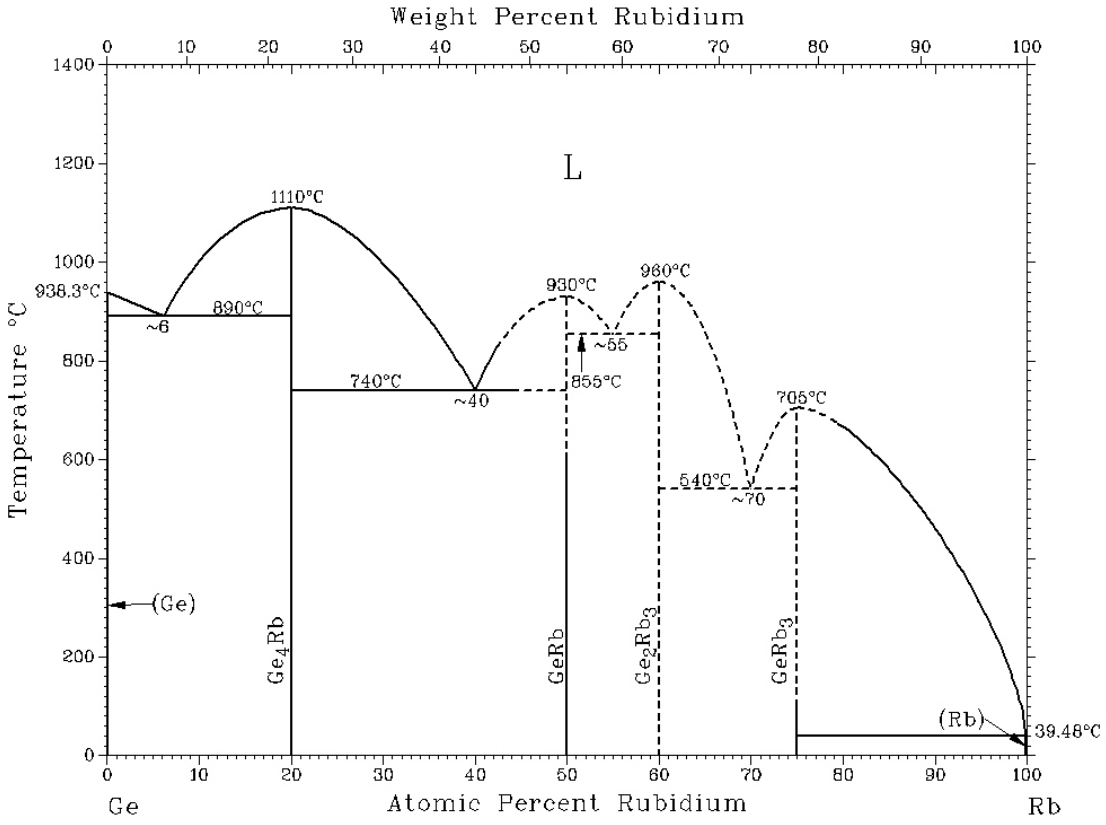
Weight Percent Rubidium
Temperature °C
Atomic Percent Rubidium
Ge
Rb
L
1110°C
938.3°C
890°C
~6
930°C
960°C
~55
855°C
740°C
~40
705°C
540°C
~70
(Ge)
Ge4Rb
GeRb
Ge2Rb3
GeRb3
(Rb)
39.48°C

Appendix B. Synchrotron data refinements for A_8Sn_{44} (A = Rb, Cs)

Table B.1 Synchrotron data refinements for Rb_8Sn_{44} in the temperature range 90 - 300 K. Atomic coordinates for space group $Ia\bar{3}d$: Rb1 = (0, 0, 0, U_{iso}), Rb2 = (0.125, 0.25, 0, U_{11}, U_{22}), Sn1 = (0.375, 0, 0.25), Sn1´ = (0.125, 0, 0.25, SOF), Sn2 = (x, x, x), Sn2´ = (x, y, z), Sn3a = (x, y, z, SOF), Sn3b = (x, y, z, 1 – SOF), Sn3´ = (x, y, z).

T / K	90	105	120	135	150	165	180
a / Å	24.0522 (2)	24.0563 (2)	24.0604 (2)	24.0646 (2)	24.0683 (2)	24.0726(2)	24.0768(2)
U_{iso}(Rb1) / Å^2	0.0061 (8)	0.0061 (9)	0.0086 (9)	0.0085 (9)	0.0096 (9)	0.011(1)	0.011(1)
U_{11}(Rb2) / Å^2	0.0009 (12)	0.0015 (13)	0.0042 (14)	0.0041 (14)	0.0062 (14)	0.008(1)	0.008(1)
U_{22}(Rb2) / Å^2	0.020 (1)	0.023 (1)	0.026 (1)	0.029 (1)	0.032 (1)	0.035(1)	0.038(1)
U_{iso}(host) / Å^2	0.0039 (3)	0.0042 (4)	0.0052 (4)	0.0055 (4)	0.0064 (4)	0.0067(4)	0.0071(4)
SOF(Sn1´)	0.3167 (7)	0.3164 (7)	0.3137 (7)	0.3124 (7)	0.3111 (7)	0.3082(7)	0.3100(7)
x(Sn2)	0.0908 (1)	0.0908 (1)	0.0908 (1)	0.0907 (1)	0.0908 (1)	0.0907(1)	0.0908(1)
x(Sn2´)	0.0895 (1)	0.0896 (1)	0.0895 (1)	0.0896 (1)	0.0896 (1)	0.0896(1)	0.0896(1)
y(Sn2´)	0.4054 (1)	0.4053 (1)	0.4053 (1)	0.4054 (1)	0.4053 (1)	0.4053(1)	0.4054(1)
z(Sn2´)	0.0904 (1)	0.0903 (1)	0.0903 (1)	0.0904 (1)	0.0903 (1)	0.0904(1)	0.0903(1)
x(Sn3a)	0.00323 (3)	0.00296 (1)	0.00297 (1)	0.00318 (1)	0.00319 (1)	0.00308(1)	0.00321(3)
y(Sn3a)	0.15193 (1)	0.15187 (1)	0.15192 (1)	0.15201 (1)	0.1521 (1)	0.15189(1)	0.15198(1)
z(Sn3a)	0.05766 (1)	0.05777 (1)	0.05773 (1)	0.05788 (1)	0.05767 (1)	0.05788(1)	0.05782(1)
SOF(Sn3a)	0.3167 (7)	0.3164 (7)	0.3137 (7)	0.3124 (7)	0.3111 (7)	0.3082(7)	0.3100(7)
x(Sn3b)	0.0012 (2)	0.0014 (2)	0.0014 (2)	0.0012 (2)	0.0013 (2)	0.0014(2)	0.0012(2)
y(Sn3b)	0.1740 (1)	0.1740 (1)	0.1741 (1)	0.1740 (1)	0.1741 (1)	0.1740(1)	0.1740(1)
z(Sn3b)	0.0671 (1)	0.0671 (1)	0.0671 (1)	0.0671 (1)	0.0671 (1)	0.0671(1)	0.0670(1)
SOF(Sn3b)	0.6833 (7)	0.6836 (7)	0.6863 (7)	0.6876 (7)	0.6889 (7)	0.6918(7)	0.6900(7)
x(Sn3´)	0.4995 (1)	0.4995 (1)	0.4996 (1)	0.4995 (1)	0.4995 (1)	0.4996(1)	0.4995(1)
y(Sn3´)	0.1540 (1)	0.1541 (1)	0.1541 (1)	0.1540 (1)	0.1540 (1)	0.1540(1)	0.1540(1)
z(Sn3´)	0.0560 (1)	0.0560 (1)	0.0560 (1)	0.0560 (1)	0.0560 (1)	0.0560(1)	0.0560(1)
U	0.034 (1)	0.028 (1)	0.027 (1)	0.027 (1)	0.029 (1)	0.028(1)	0.031(1)
V	0.0001 (3)	0.0012 (3)	0.0015 (3)	0.0015 (3)	0.0009 (3)	0.0012(3)	0.0008(3)
W	0.00124 (2)	0.00120 (2)	0.00118 (2)	0.00117 (2)	0.00121 (2)	0.00118(2)	0.00119(2)
X	0.023 (3)	0.038 (3)	0.039 (3)	0.040 (2)	0.034 (3)	0.041(2)	0.039(2)
Y	0.0005 (1)	–0.0001 (1)	–0.0003 (1)	–0.0003 (1)	0.0000 (1)	–0.0004(1)	–0.0003(1)
R_p	6.06	6.31	6.31	6.24	6.09	6.17	6.13
R_{wp}	6.42	6.84	6.80	6.75	6.65	6.63	6.62
R_{exp}	2.37	2.42	2.45	2.44	2.46	2.47	2.48
χ^2	7.32	7.99	7.69	7.64	7.32	7.21	7.11
R_F	1.68	1.67	1.63	1.62	1.66	1.55	1.68
R_I	1.87	1.82	1.78	1.81	1.74	1.72	1.77

Table B.1 (continued)

T / K	195	210	225	240	255	270	285	300
a / Å	24.0809(3)	24.0853(3)	24.0895(3)	24.0938(3)	24.0980(3)	24.1017(3)	24.1046(3)	24.1082(3)
U_{iso}(Rb1) / Å^2	0.012(1)	0.013(1)	0.015(1)	0.016(1)	0.017(1)	0.017(1)	0.018(1)	0.019(1)
U_{11}(Rb2) / Å^2	0.009(1)	0.010(1)	0.011(1)	0.013(1)	0.014(2)	0.014(2)	0.016(2)	0.018(2)
U_{22}(Rb2) / Å^2	0.039(1)	0.043(1)	0.046(1)	0.048(1)	0.051(1)	0.054(1)	0.056(1)	0.058(1)
U_{iso}(host) / Å^2	0.0077(4)	0.0085(4)	0.0095(4)	0.0103(4)	0.0110(4)	0.0115(4)	0.0119(4)	0.0125(4)
SOF(Sn1´)	0.3134(7)	0.3071(7)	0.3057(7)	0.2998(7)	0.3125(7)	0.3027(7)	0.3056(7)	0.3047(7)
x(Sn2)	0.0907(1)	0.0908(1)	0.0907(1)	0.0908(1)	0.0907(1)	0.0908(1)	0.0907(1)	0.0907(1)
x(Sn2´)	0.0896(1)	0.0896(1)	0.0896(1)	0.0896(1)	0.0897(1)	0.0896(1)	0.0896(1)	0.0896(1)
y(Sn2´)	0.4053(1)	0.4054(1)	0.4053(1)	0.4053(1)	0.4054(1)	0.4054(1)	0.4053(1)	0.4054(1)
z(Sn2´)	0.0904(1)	0.0904(1)	0.0903(1)	0.0904(1)	0.0904(1)	0.0904(1)	0.0904(1)	0.0905(1)
x(Sn3a)	0.00319(1)	0.00321(1)	0.00312(1)	0.4996(1)	0.4996(1)	0.4996(1)	0.4996(1)	0.4996(1)
y(Sn3a)	0.15167(1)	0.15191(1)	0.15206(1)	0.1540(1)	0.1540(1)	0.1539(1)	0.1539(1)	0.1540(1)
z(Sn3a)	0.05783(1)	0.05782(1)	0.05760(1)	0.0560(1)	0.0560(1)	0.0560(1)	0.0560(1)	0.0559(1)
SOF(Sn3a)	0.3134(7)	0.3071(7)	0.3057(7)	0.2998(7)	0.3125(7)	0.3027(7)	0.3056(7)	0.3047(7)
x(Sn3b)	0.0013(2)	0.0012(2)	0.0013(2)	0.0013(2)	0.0013(2)	0.0013(3)	0.0011(2)	0.0012(3)
y(Sn3b)	0.1739(1)	0.1740(1)	0.1740(1)	0.1740(1)	0.1739(1)	0.1740(1)	0.1740(1)	0.1739(1)
z(Sn3b)	0.0669(1)	0.0670(1)	0.0670(1)	0.0670(1)	0.0670(1)	0.0670(1)	0.0670(1)	0.0670(1)
SOF(Sn3b)	0.6866(7)	0.6929(7)	0.6943(7)	0.7002(7)	0.6875(7)	0.6973(7)	0.6944(7)	0.6953(7)
x(Sn3´)	0.4996(1)	0.4996(1)	0.4996(1)	0.00310(1)	0.00319(1)	0.00308(1)	0.00352(1)	0.00331(1)
y(Sn3´)	0.1540(1)	0.1540(1)	0.1539(1)	0.15194(1)	0.15177(1)	0.15206(1)	0.15185(1)	0.15178(1)
z(Sn3´)	0.0560(1)	0.0560(1)	0.0561(1)	0.05794(1)	0.05794(1)	0.05788(1)	0.05792(1)	0.05792(1)
U	0.030(1)	0.032(1)	0.031(1)	0.031(1)	0.031(1)	0.031(1)	0.033(1)	0.035(1)
V	0.0008(3)	0.0005(3)	0.0006(3)	0.0005(3)	0.0007(3)	0.0008(3)	0.0001(3)	–0.0001(3)
W	0.00119(2)	0.00120(2)	0.00120(2)	0.00120(2)	0.00119(2)	0.00117(2)	0.00123(2)	0.00122(2)
X	0.042(2)	0.038(2)	0.039(2)	0.036(2)	0.041(2)	0.042(2)	0.040(2)	0.041(2)
Y	–0.0004(1)	–0.0003(1)	–0.0003(1)	–0.0001(1)	–0.0004(1)	–0.0004(1)	–0.0002(1)	–0.0003(1)
R_p	6.21	6.16	6.12	6.25	6.25	6.17	6.12	6.11
R_{wp}	6.66	6.57	6.57	6.61	6.55	6.48	6.40	6.38
R_{exp}	2.49	2.49	2.50	2.51	2.53	2.56	2.58	2.59
χ^2	7.13	6.96	6.88	6.95	6.70	6.41	6.16	6.08
R_F	1.69	1.61	1.66	1.83	1.72	1.60	1.67	1.75
R_I	1.83	1.77	1.76	1.87	1.85	1.69	1.75	1.81

Table B.2 Synchrotron data refinements for Rb_8Sn_{44} in the temperature range 300 - 475 K. Atomic coordinates for space group $Ia\bar{3}d$: Rb1 = (0, 0, 0, U_{iso}), Rb2 = (0.125, 0.25, 0, U_{11}, U_{22}), Sn1 = (0.375, 0, 0.25), Sn1´ = (0.125, 0, 0.25, SOF), Sn2 = (x, x, x), Sn2´ = (x, y, z), Sn3a = (x, y, z, SOF), Sn3b = (x, y, z, 1 – SOF), Sn3´ = (x, y, z). Atomic coordinates for space group $Pm\bar{3}n$: Rb1 = (0, 0, 0, U_{iso}), Rb2 = (0.25, 0.5, 0, U_{11}, U_{22}), Sn1 = (0.25, 0, 0.5, SOF), Sn2 = (x, x, x), Sn3a = (0, y, z, SOF), Sn3b = (0, y, z, 1 – SOF). The structure refinement and weight percentage of *β*-Sn as secondary phase is also listed.

T / K	300	335	370	405	440	475
Space group	$Ia\bar{3}d$	$Ia\bar{3}d$	$Pm\bar{3}n$	$Pm\bar{3}n$	$Pm\bar{3}n$	$Pm\bar{3}n$
a / Å	24.1031 (4)	24.1156 (4)	12.0645 (1)	12.0715 (2)	12.0793 (1)	12.0856 (1)
U_{iso}(Rb1) / Å^2	0.020 (1)	0.024 (1)	0.024 (1)	0.023 (1)	0.031 (2)	0.031 (3)
U_{11}(Rb2) / Å^2	0.019 (2)	0.022 (2)	0.024 (2)	0.027 (2)	0.025 (3)	0.014 (5)
U_{22}(Rb2) / Å^2	0.055 (2)	0.060 (2)	0.070 (2)	0.082 (2)	0.093 (3)	0.099 (5)
U_{iso}(host) / Å^2	0.014 (1)	0.017 (1)	0.020 (1)	0.024 (1)	0.026 (1)	0.031 (1)
SOF(Sn1)			0.684 (1)	0.685 (1)	0.686 (1)	0.688 (1)
SOF(Sn1´)	0.347 (1)	0.349 (1)				
x(Sn2)	0.0907 (1)	0.0906 (1)	0.1827 (1)	0.1826 (1)	0.1827 (1)	0.1831 (1)
x(Sn2´)	0.0896 (1)	0.0897 (1)				
y(Sn2´)	0.4053 (1)	0.4053 (1)				
z(Sn2´)	0.0904 (1)	0.0904 (1)				
x(Sn3a)	0.0027 (6)	0.0023 (6)	0	0	0	0
y(Sn3a)	0.1516 (4)	0.1517 (4)	0.3071 (1)	0.3071 (1)	0.3068 (2)	0.3062 (3)
z(Sn3a)	0.0582 (4)	0.0579 (4)	0.1133 (1)	0.1135 (2)	0.1138 (2)	0.1145 (3)
SOF(Sn3a)	0.347 (1)	0.349 (1)	0.685 (1)	0.685 (1)	0.686 (1)	0.688 (1)
x(Sn3b)	0.0016 (4)	0.0020 (4)	0	0	0	0
y(Sn3b)	0.1739 (1)	0.1739 (1)	0.3475 (2)	0.3477 (3)	0.3477 (5)	0.3486 (7)
z(Sn3b)	0.0668 (1)	0.0668 (1)	0.1350 (3)	0.1340 (3)	0.1330 (5)	0.1303 (7)
SOF(Sn3b)	0.653 (1)	0.651 (1)	0.315 (1)	0.315 (1)	0.314 (1)	0.312 (1)
x(Sn3´)	0.4996 (2)	0.4999 (2)				
y(Sn3´)	0.1539 (1)	0.1540 (1)				
z(Sn3´)	0.0562 (1)	0.0562 (1)				
U	0.049 (5)	0.057 (5)	0.053 (3)	0.028 (3)	0.012 (4)	0.009 (5)
V	–0.0023 (9)	–0.0037 (9)	–0.0044 (7)	–0.0007 (7)	0.0018 (8)	–0.0003 (9)
W	0.00145 (4)	0.00154 (4)	0.00162 (3)	0.00128 (3)	0.00112 (4)	0.00116 (4)
X	0.055 (7)	0.042 (8)	0.048 (2)	0.036 (3)	0.019 (4)	0.053 (8)
a(Sn) / Å	5.8299 (5)	5.8336 (5)	5.8379 (4)	5.8430 (1)	5.8469 (1)	5.8508 (1)
b(Sn) / Å	3.1810 (3)	3.1853 (3)	3.1899 (2)	3.1945 (1)	3.1991 (1)	3.2038 (1)
U_{iso}(Sn) / Å^2	0.009 (3)	0.009 (3)	0.016 (3)	0.029 (1)	0.034 (1)	0.039 (1)
R_p	6.5	6.6	5.9	7.5	8.9	9.6
R_{wp}	6.2	6.2	5.2	6.6	7.8	7.9
R_{exp}	3.7	3.8	4.0	4.1	4.2	4.2
χ^2	2.8	2.7	1.7	2.6	3.5	3.6
R_F (Rb_8Sn_{44})	1.8	2.0	1.7	2.5	3.3	6.0
R_I (Rb_8Sn_{44})	1.8	1.9	1.5	2.2	2.8	5.2
R_F (Sn)	1.5	1.8	1.9	2.4	2.4	2.0
R_I (Sn)	2.7	3.2	1.9	2.6	1.9	1.9
Weight frac. (Rb_8Sn_{44}) (%)	97.5 (6)	97.4 (6)	97.9 (5)	91.8 (5)	75.5 (5)	49.3 (5)
Weight frac. (Sn) (%)	2.6 (1)	2.6 (1)	2.1 (1)	8.2 (1)	24.5 (2)	50.7 (4)

Table B.3 Synchrotron data refinements for Cs_8Sn_{44} in the temperature range 300 - 510 K. Atomic coordinates for space group $Ia\bar{3}d$: Cs1 = (0, 0, 0, U_{iso}), Cs2 = (0.125, 0.25, 0, U_{11}, U_{22}), Sn1 = (0.375, 0, 0.25), Sn1´ = (0.125, 0, 0.25, SOF), Sn2 = (x, x, x), Sn2´ = (x, y, z), Sn3a = (x, y, z, SOF), Sn3b = (x, y, z, 1 – SOF), Sn3´ = (x, y, z). Atomic coordinates for space group $Pm\bar{3}n$: Cs1 = (0, 0, 0, U_{iso}), Cs2 = (0.25, 0.5, 0, U_{11}, U_{22}), Sn1´ = (0.25, 0, 0.5, SOF), Sn2 = (x, x, x), Sn3a = (0, y, z, SOF), Sn3b = (0, y, z, 1 – SOF). The structure refinement and weight percentage of *β*-Sn as secondary phase is also listed.

T / K	300	335	370	405	440	475	510
Space group	$Ia\bar{3}d$	$Ia\bar{3}d$	$Pm\bar{3}n$	$Pm\bar{3}n$	$Pm\bar{3}n$	$Pm\bar{3}n$	$Pm\bar{3}n$
a / Å	24.2125 (2)	24.2234 (2)	12.1176 (1)	12.1233 (1)	12.1301 (1)	12.1381 (1)	12.1464 (1)
U_{iso}(Cs1) / Å^2	0.0137 (6)	0.0156 (7)	0.0169 (6)	0.0190 (7)	0.0202 (7)	0.0217 (9)	0.025 (1)
U_{11}(Cs2) / Å^2	0.015 (1)	0.018 (1)	0.020 (1)	0.020 (1)	0.023 (1)	0.024 (2)	0.028 (3)
U_{22}(Cs2) / Å^2	0.041 (1)	0.046 (1)	0.0496 (9)	0.0546 (9)	0.060 (1)	0.066 (1)	0.076 (2)
U_{iso}(host) / Å^2	0.0135 (3)	0.0155 (3)	0.0195 (3)	0.0206 (3)	0.0225 (3)	0.0242 (4)	0.0292 (5)
SOF(Sn1)			0.6941 (2)	0.6957 (2)	0.7020 (2)	0.7047 (3)	0.7188 (5)
SOF(Sn1´)	0.3361 (4)	0.3386 (4)					
x(Sn2)	0.0907 (1)	0.0907 (1)	0.1830 (1)	0.1831 (1)	0.1831 (1)	0.1831 (1)	0.1827 (1)
x(Sn2´)	0.0897 (1)	0.0897 (1)					
y(Sn2´)	0.4049 (1)	0.4048 (1)					
z(Sn2´)	0.0906 (1)	0.0905 (1)					
x(Sn3a)	0.0025 (5)	0.0025 (5)	0	0	0	0	0
y(Sn3a)	0.1525 (3)	0.1524 (3)	0.3074 (1)	0.3073 (1)	0.3074 (1)	0.3073 (1)	0.3071 (2)
z(Sn3a)	0.0578 (4)	0.0580 (4)	0.1140 (1)	0.1138 (1)	0.1140 (1)	0.1143 (2)	0.1142 (3)
SOF(Sn3a)	0.3361 (4)	0.3386 (4)	0.6941 (2)	0.6957 (2)	0.7020 (2)	0.7047 (3)	0.7188 (5)
x(Sn3b)	0.0020 (3)	0.0018 (3)	0	0	0	0	0
y(Sn3b)	0.1725 (1)	0.1725 (1)	0.3447 (2)	0.3443 (2)	0.3444 (3)	0.3447 (4)	0.3438 (6)
z(Sn3b)	0.0671 (1)	0.0669 (1)	0.1353 (3)	0.1357 (3)	0.1355 (3)	0.1348 (4)	0.1363 (7)
SOF(Sn3b)	0.6639 (4)	0.6614 (4)	0.3059 (2)	0.3043 (2)	0.2980 (2)	0.2953 (3)	0.2812 (5)
x(Sn3´)	0.4995 (1)	0.4995 (2)					
y(Sn3´)	0.1535 (1)	0.1536 (1)					
z(Sn3´)	0.0564 (1)	0.0565 (1)					
U	0.021 (2)	0.020 (2)	0.016 (2)	0.017 (2)	0.017 (2)	0.013 (2)	0.009 (2)
V	0.0000 (5)	0.0004 (5)	–0.0009 (4)	–0.0012 (4)	–0.0011 (4)	–0.0010 (4)	–0.0003 (6)
W	0.00110 (2)	0.00108 (3)	0.00114 (2)	0.00116 (2)	0.00112 (2)	0.00107 (2)	0.00084 (3)
X	0.032 (2)	0.031 (2)	0.035 (2)	0.041 (2)	0.042 (2)	0.042 (4)	–0.022 (3)
a(Sn) (Å)	5.8311 (7)	5.8353 (7)	5.8402 (7)	5.8446 (7)	5.8480 (3)	5.8515 (1)	
b(Sn) (Å)	3.1805 (5)	3.1846 (5)	3.1891 (5)	3.1937 (4)	3.2002 (2)	3.2048 (1)	
U_{iso}(Sn) / Å^2	0.026 (9)	0.03 (1)	0.06 (2)	0.06 (1)	0.036 (5)	0.038 (1)	
R_p	7.1	7.4	7.1	7.2	7.6	9.0	13.5
R_{wp}	7.4	7.4	6.7	6.8	7.0	8.6	14.1
R_{exp}	2.9	3.3	3.4	3.5	3.5	3.7	4.7
χ^2	6.6	5.1	3.8	3.7	4.0	5.5	9.2
R_F (Cs_8Sn_{44})	2.8	3.1	3.3	3.6	4.0	4.8	9.0
R_I (Cs_8Sn_{44})	2.5	2.6	2.1	2.2	2.4	3.0	5.7
R_F (Sn)	2.7	2.8	3.6	4.3	5.5	5.0	
R_I (Sn)	4.3	4.1	4.3	3.6	6.0	4.5	
Weight frac. (Cs_8Sn_{44}) (%)	99.3 (4)	99.3 (4)	99.2 (4)	99.2 (4)	98.4 (4)	91.2 (5)	
Weight frac. (Sn) (%)	0.7 (1)	0.7 (1)	0.8 (1)	0.8 (1)	1.6 (1)	8.9 (1)	

Appendix C. Single-crystal data refinement for β-$Rb_{1.46}Cs_{6.54}Sn_{44}$

Table C.1 Crystallographic data and refinement parameters for β-$Rb_{1.46}Cs_{6.54}Sn_{44}$.

Chemical formula	$Rb_{1.46(5)}Cs_{6.54(5)}Sn_{44}$
Space group (No.)	$Pm\bar{3}n$ (223)
Formula weight	6216.38
Temperature, T / K	373
Diffractometer	APEX II
Radiation, λ / Å	Mo-Kα, 0.71073
Z	1
a / Å	12.0878(2)
V / Å^3	1766.21(5)
$\rho_{calc.}$ / g cm^{-3}	5.844
Absor. coeff., μ / mm^{-1}	19.55
F(000)	2614
θ range for data collection / °	2.38 - 30.50
Index ranges	$-5 \le h \le 14$, $-14 \le k \le 13$, $-17 \le l \le 15$
Reflections collected	4605
Indep. reflections	508 (R_{int} = 0.031)
Parameters	24
Goodness-of-fit on F^2	1.127
Weighting parameters	a = 0.0125, b = 2.623
Final R indices (I > 2σ(I))	R_1 = 0.019, wR_2 = 0.035
R indices (all data)	R_1 = 0.032, wR_2 = 0.037
Largest diff. peak and hole / e Å^{-3}	0.64 in 1.40 Å from Sn3a –0.57 in 2.18 Å from Sn2

Table C.2 Atomic coordinates and equivalent isotropic displacement parameters for *β*-$Rb_{1.46}Cs_{6.54}Sn_{44}$.

Atom	Site	*x*	*y*	*z*	SOF	U_{eq} / Å^2
Rb/Cs1	2*a*	0	0	0	0.46/0.54(1)	0.0235(4)
Rb/Cs2	6*d*	0.25	0.5	0	0.09/0.91(1)	0.0478(3)
Sn1	6*c*	0.25	0	0.5	0.667	0.0175(2)
Sn2	16*i*	0.18299(2)	0.18299(2)	0.18299(2)	1	0.0252(1)
Sn3a	24*k*	0	0.30551(7)	0.1137(1)	0.667	0.0221(2)
Sn3b	24*k*	0	0.3443(1)	0.1338(2)	0.333	0.0260(4)

Table C.3 Anisotropic displacement parameters for *β*-$Rb_{1.46}Cs_{6.54}Sn_{44}$ (in Å^2).

Atom	U_{11}	U_{22}	U_{33}	U_{12}	U_{13}	U_{23}
Rb/Cs1	0.0235(4)	0.0235(4)	0.0235(4)	0	0	0
Rb/Cs2	0.0281(5)	0.0576(4)	0.0576(4)	0	0	0
Sn1	0.0188(5)	0.0169(3)	0.0169(3)	0	0	0
Sn2	0.0252(1)	0.0252(1)	0.0252(1)	–0.0038(1)	–0.0038(1)	–0.0038(1)
Sn3a	0.0223(3)	0.0190(5)	0.0251(4)	0	0	–0.0029(3)
Sn3b	0.0240(7)	0.028(1)	0.0256(9)	0	0	0.0063(7)

Appendix D. List of publications

1. A. Kaltzoglou, S. D. Hoffmann, T. F. Fässler *Eur. J. Inorg. Chem.* **2007**, 4162. *Order-Disorder Phase Transition in Type-I Clathrate $Cs_8Sn_{44}\square_2$*
2. A. Kaltzoglou, S. Ponou, T. F. Fässler *Eur. J. Inorg. Chem.* **2008**, 538. *Synthesis and Crystal Structure of the Mercury Substituted Type-I Clathrates $A_8Hg_4Sn_{42}$ (A = K, Rb, Cs)*
3. A. Kaltzoglou, T. F. Fässler, M. Christensen, S. Johnsen, B. B. Iversen, I. Presniakov, A. Sobolev, A. Shevelkov *J. Mater. Chem.* **2008**, *18*, 5630. *Effects of the Order-Disorder Phase Transition on the Physical Properties of $A_8Sn_{44}\square_2$ (A = Rb, Cs)*
4. H. Shimizu, T. Imai, T. Kume, S. Sasaki, A. Kaltzoglou, T. F. Fässler *Chem. Phys. Lett.* **2008**, *464*, 54. *Raman Spectroscopy Study of Type-I Clathrates $A_8Sn_{44}\square_2$ (A= Rb, Cs)*
5. A. Kaltzoglou, S. Ponou, T. F. Fässler *Eur. J. Inorg. Chem.* **2008**, 4507. *A_4Ge_9 (A = K, Rb) as Precursors for Hg-Substituted Clathrate-I Synthesis: Crystal Structure of $A_8Hg_3Ge_{43}$*
6. A. Kaltzoglou, T. F. Fässler, T. Kume, H. Shimizu, C. Gold, E.-W. Scheidt, W. Scherer *submitted. Substitution Effects in Type-I Clathrates $Rb_xCs_{8-x}Sn_{44}\square_2$ (1.3 ≤ x ≤ 2.1)*